ALMA MATER STUDIORUM · UNIVERSITÀ DI BOLOGNA

Scuola di Scienze
Corso di Laurea Magistrale in Fisica del Sistema Terra

THE Q-VECTOR THEORY:
A TOOL FOR THE IDENTIFICATION OF INTENSE CYCLONES

Relatore:
Prof. Silvana Di Sabatino

Correlatori:
Dott. Barbara Turato
Dott. Mario Marcello Miglietta
Dott. Silvio Davolio

Candidato:
Lucia Drago Pitura

Abstract

La tesi si è concentrata sull'analisi del ciclone extra-tropicale che ha colpito la parte centro-occidentale del Mar Mediterraneo il 29 ottobre 2018, denominato Vaia. L'evento ciclonico ha interessato principalmente le regioni del Nord Italia: Liguria, Emilia-Romagna, Trentino Alto Adige, Friuli Venezia Giulia e Veneto, causando gravi e diffusi danni, come la devastazione della costa ligure e lo sradicamento degli alberi su vaste superfici forestali in alcune foreste dolomitiche.

Per studiare la tempesta Vaia, è stato utilizzato l'approccio della teoria del Q-vector, uno strumento teorico in grado di combinare la variazione del vento geostrofico con la variazione termica orizzontale, fornendo informazioni sulla frontogenesi, al fine di capire se il Q-vector possa rappresentare un utile strumento previsionale per i cicloni baroclini.

Il Q-vector è un concetto matematico utilizzato nei centri operativi principalmente all'estero, ma raramente viene utilizzato negli studi accademici. Poiché la tempesta Vaia è registrata come un evento estremo per i danni che ha causato, soprattutto a causa dell'estrema velocità del vento, si è voluto analizzare la risposta del Q-vector poiché nel Mar Mediterraneo è stato usato raramente. La particolarità di questo ciclone è la presenza di un gradiente di temperatura molto elevato, che suggerisce un ruolo chiave della frontogenesi durante intensi eventi meteorologici osservati nel Nord Italia. Quindi, si è voluto capire quanto fossero eccezionali i valori della frontogenesi osservati nel ciclone Vaia rispetto alla climatologia dei cicloni mediterranei.

Come prima analisi, è stato effettuato un confronto tra i valori del Q-vector assunti dai cicloni di diversa natura con quelli assunti da Vaia. In secondo luogo, sono stati analizzati i meccanismi che hanno portato all'intensificazione del ciclone Vaia attraverso *sensitivity tests* e, infine, è stata effettuata un'analisi climatologica, utilizzando i valori del Q-vector per l'identificazione e la selezione dei cicloni che hanno interessato l'area centro -occidentale del Mediterraneo per comprendere la frequenza di eventi caratterizzati da valori di frontogenesi comparabili a quelli di Vaia. Con l'ultima analisi si è cercato di identificare una possibile tendenza dell'intensità del Q-vector.

Abstract

The thesis focused on the analysis of the extra-tropical cyclone that affected the central-western part of the Mediterranean Sea on 29 October 2018, called Vaia. The cyclonic event mainly affected the regions of Northern Italy: Liguria, Emilia-Romagna, Trentino Alto Adige, Friuli Venezia Giulia and Veneto, causing serious and widespread damage, such as the devastation of the Ligurian coast and the uprooting of trees on vast forest surfaces in some of the Dolomite forests.

To study the Vaia storm, the Q-vector theory approach was used, a theoretical tool capable of combining the variation of the geostrophic wind with the horizontal thermal variation, providing information on the frontogenesis, in order to understand whether the Q-vector could represent a useful predictive tool for baroclinic cyclones. The Q-vector is a mathematical concept used in the operational centers mainly abroad but is rarely used in academic studies. Since the storm Vaia is recorded as an extreme event for its damage, especially due to the extreme wind speed, we wanted to understand the response of the Q-vector since in the Mediterranean Sea it was rarely used. The peculiarity of this cyclone is the presence of very high temperature gradient, suggesting a key role of frontogenesis in the severe weather episodes observed in Northern Italy. Hence, we wanted to understand how exceptional were the values of frontogenesis observed in the cyclone Vaia in comparison with the climatology of Mediterranean cyclones.

As a first analysis, a comparison was made among the Q-vector values assumed by cyclones of different nature with those assumed by Vaia. Second, the mechanisms that led to the intensification of the cyclone Vaia were analyzed through a sensitivity test and last, but not least, a climatological analysis was carried out, using the Q-vector values for the identification and selection of cyclones that affected the central-western Mediterranean area in order to understand the frequency of events characterized by frontogenesis values comparable with that of Vaia. With the last analysis we tried to identify a possible trend of the Q-vector intensity.

Contents

Chapter 1

General description of cyclogenesis in the Mediterranean Sea and explosive cyclogenesis

1.1 Introduction

Before describing the mechanisms that regulate cyclogenesis in the Mediterranean, it is necessary to briefly recall some key concepts of the general circulation of the atmosphere.

The difference in insolation between the equator and the poles determines, together with the terrestrial rotation, the formation of three large convective air cells for each hemisphere. In the northern hemisphere they are: the Hadley cell, whose average position is from equatorial latitudes up to $30°N$, the Ferrel cell, whose average position is between latitudes $30°N$ to $60°N$, and finally the Polar cell, which extends from $60°N$ to polar latitudes. As a consequence of these circulations, high and low pressures are created at the ground as shown in Figures 1.1 and 1.2.

The dividing line on the ground between the subtropical and polar air is called the Polar Front. The Polar Front is not a rigid and immobile barrier, as it moves due to the presence of westerlies and suffers sudden path deviations, induced by the alternation of oceans and continents or mountain ranges. These undulations are called Rossby waves (Figura 1.3) and are therefore produced by alternating thrusts of tropical air towards northern latitudes (ridge) and polar air towards southern latitudes (trough or depression).

The high-level depressions that move in the mid-latitudes trigger the formation at the ground of cyclonic structures (Figure 1.4) called extratropical cyclones.

Looking at Figure 1.4, the horizontal divergence of air in the upper troposphere, at the south-western branches of the polar jet current, generates a decrease of surface pressure and an increase of vorticity resulting in the rise of air. The air masses that converge horizontally towards the depression at the ground to replace those rising, acquire an anti-clockwise rotation around the low pressure center in the northern hemisphere, due to the gradient wind, that is the balance between the force of Coriolis,

5

the centrifugal force and the horizontal pressure gradient force. This cyclonic rotation favors warm air advection towards the areas occupied by cold air (warm front) and cold air advection towards the regions occupied by warmer air (cold front). This is how extra-tropical cyclones, typical mobile depressions associated with frontal structures, generate. These swirling structures together with other, from small to large scale features, guarantee the transport of heat from the Equator to the Poles.
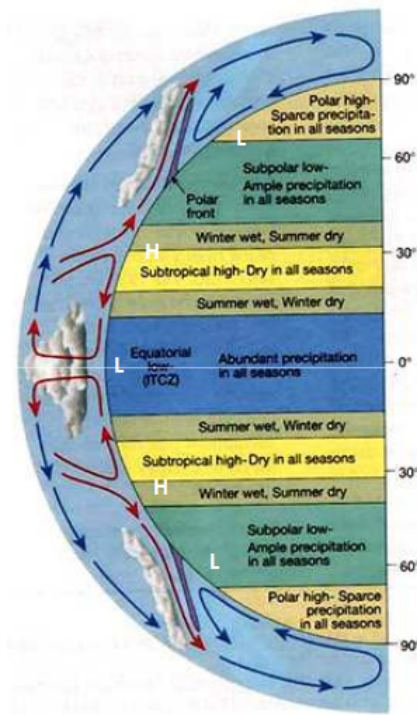
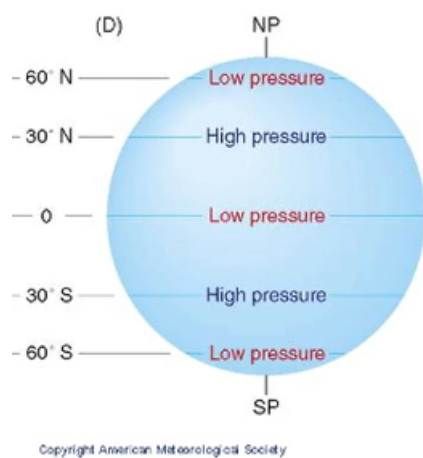

Figure 1.1: General circulation in the atmosphere.

Figure 1.2: Average position of the high and low pressures created by the general circulation of the atmosphere.
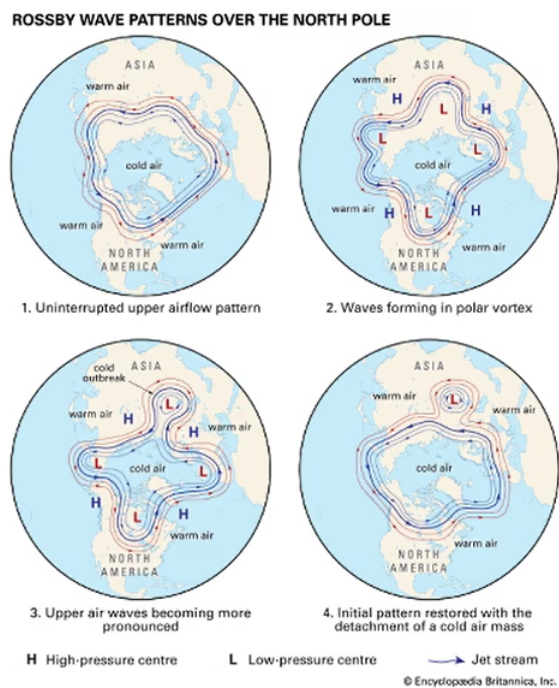

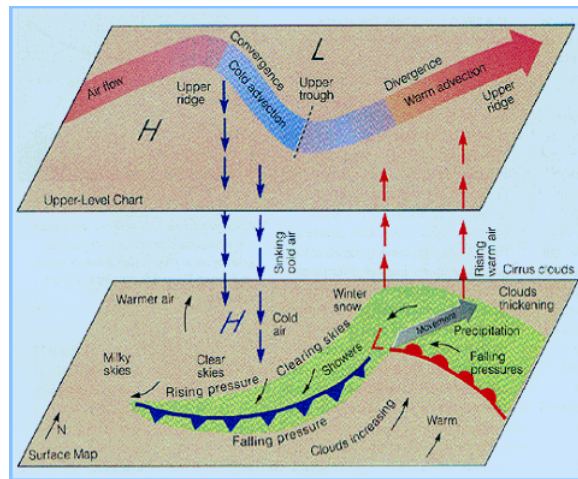Figure 1.3: Rossby Wave formation (polar stereographic projection).

Figure 1.4: Ground formation of a low pressure depression structure.

1.2 Climatology of the Mediterranean Sea

The Mediterranean region is a vast area that extends for over 4.000 km from west to east and 1.500 km from south to north and is characterized by various climatic *patterns*, synoptic weather conditions and hydrological properties, such as type of surface, land use and plant cover. The Mediterranean basin is a region with frequent cyclone development, influenced by the transit of depressions in the upper troposphere generated on the Atlantic Ocean or in Northwest Europe. The study and forecast of the dynamic evolution of the depressions is complex given that the Mediterranean is surrounded by mountain ranges and is warmer than the ocean.

So, in summary, the unique meteorological characteristics of the Mediterranean are also strongly influenced by the fact that:

- it is an almost closed sea; it represents an important source of energy and humidity for the development of cyclones

- it is characterized by a complex orography, conducive to the development of secondary cyclogenesis, that is, low pressure areas generated downwind of the mountain chains when they are hit perpendicularly by intense flows.

The main characteristics of the Mediterranean climate are humid winters and warm and very dry summers. The singular seasonal characteristics of the Mediterranean are directly linked in winter to the extension to the south of an area of depressions and westerly winds that blow from the Atlantic to Europe, in the summer season to the formation of a large depression centered on Southwest Asia. During the year, the permanent subtropical anticyclone on the Atlantic, south of the depression area, and generally known as the "Azores anticyclone", considerably changes its position and shape. On average during winter it is found in the southern part of its annual excursion and in summer in the northern part. In winter it extends like a long and narrow belt from Egypt to North America while a narrow band of high pressure on western Europe demarcates a relatively low pressure in the Mediterranean region. In this season, the cold air from the north-west frequently and intensely enters the Mediterranean where it meets hot and humid air, and therefore conditions for the development of intense depressions and rainfall are created. Many cyclones observed in the region either develop on the sea itself or are reinforced once they reach the basin.

A detailed climatology of the cyclones for the area would be relevant for a more complete understanding of the dynamics of the atmosphere in the subtropical margins and of the relationship between cyclones and air-sea fluxes, as well as, as far as possible, of the projections in future storms and their implications for local weather conditions.

Petterssen (1956) was the first to study the frequency of cyclones in the Mediterranean as part of a climatology that covers the entire Northern hemisphere. As evidenced by the study of *Trigo et al.* over a period of 18 years [23] the presence of a number of cyclogenetic areas has been highlighted, apparently determined mainly by the topography of the region, in which the events of cyclogenesis tend to concentrate.

Figures 1.5 and 1.6 show the concentration of events where the peaks are located, mainly in the areas listed below; moreover, areas with a lower concentration of events can also be observed.

The western Mediterranean basin seems to be dominated by three main regions of cyclogenesis.

1. LIGURIAN GULF: cyclones are formed mainly in the lee of the Alps [4]; it constitutes one of the main regions of cyclogenesis of the entire study domain and one of the most persistent throughout the year (the surface depression is created on the Ligurian Sea when the Central-Western Alps are affected by strong mistral currents).

2. SAHARA DESERT: Saharan cyclones (or Sharav depressions) seem to be the dominant feature in the Mediterranean spring. In North Africa there are three areas favorable to the development of cyclogenesis. The area where it is most frequent is the one located on the north-western part, visible throughout the year and which peaks between May and June. Cyclogenesis downwind (orographic cyclogenesis, also called Lee cyclogenesis) of the Atlas chain is considered as the primary mechanism of formation of these Saharan pressure low [9], along with an influence of desert sand that amplifies the radiative heating profiles [22], the maximum observed on the North African Atlantic coast seems to be mainly induced by the sea-land contrast during the warmer season.

3. IBERIAN PENINSULA: the relatively warm surface and the sea-land thermal contrast favor the formation of shallow thermal minima on the Iberian peninsula from late spring until summer. A three-nuclei structure - above the eastern, western and central coasts - becomes particularly pronounced between June and August.

Cyclogenesis in the eastern part of the domain appears to be distributed among four main regions.

1. AEGEAN SEA: one of the main sources of winter and spring cyclones.

2. BLACK SEA: the maximum cyclogenetic frequency occurs on the Eastern Black Sea throughout the year, becoming particularly pronounced in the months of July and August (an average of one cyclogenesis for week).

3. CYPRUS: from the maps in Figures 1.5 and 1.6, the cyclogenetic activity is highest in the period between July and October.

4. MIDDLE EAST: the maximum cyclogenetic frequency is observed on Syria and Iraq.

The areas located in the Eastern Mediterranean in the analysis carried out in this study will not be taken into consideration.
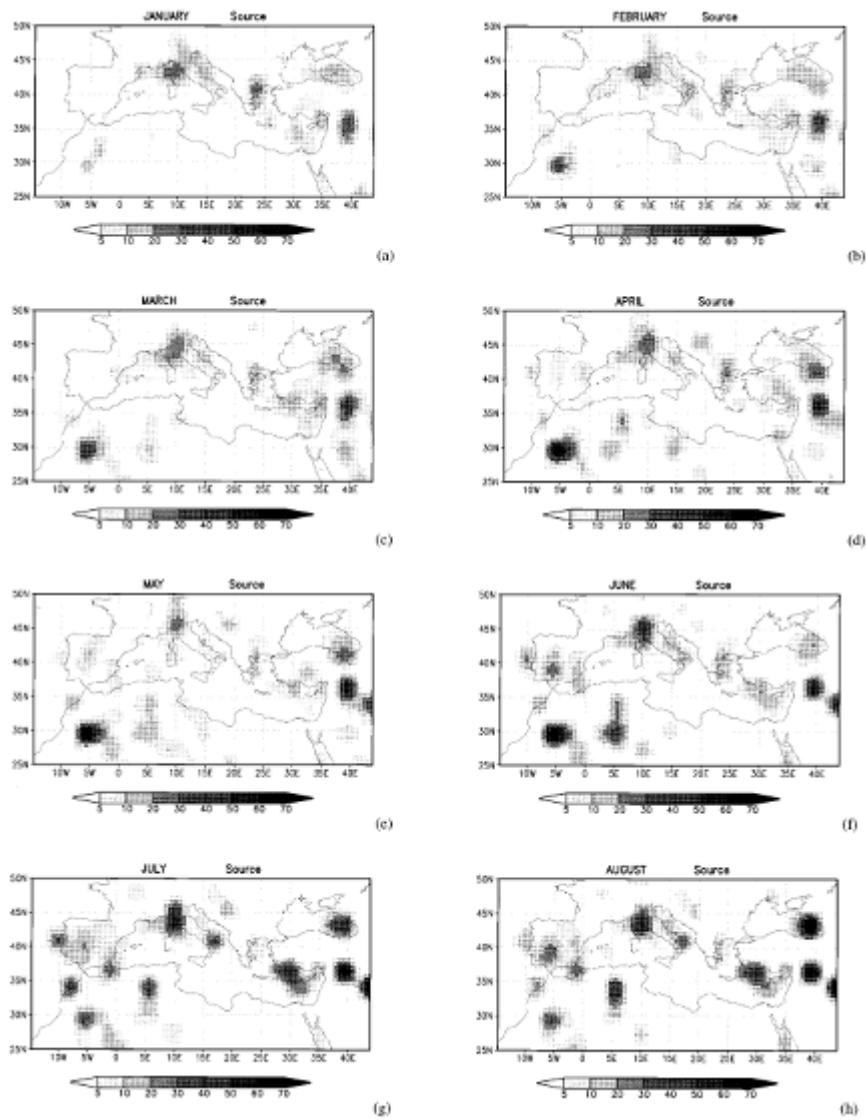
Figure 1.5: Number of cyclogenesis events detected per cell 2.25X2.25 degrees, for each month from January to August, for periods of 18 years [23].
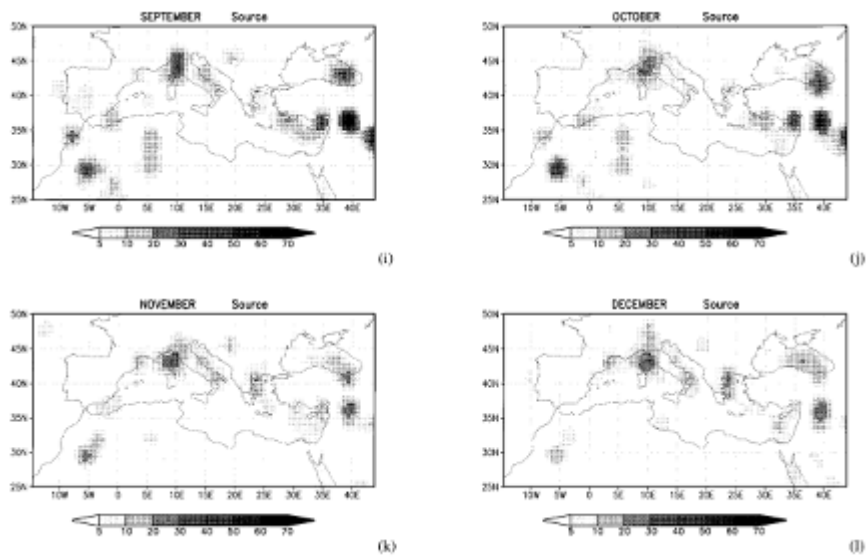
Figure 1.6: Number of cyclogenesis events detected per cell $2.25X2.25$ degrees, for each month from September to December, for the entire 18-year period [23].

1.3 Explosive cyclogenesis

The extra-tropical cyclone named Vaia, the main event analysed in the present thesis, is a Mediterranean depression that was characterized by an explosive dynamics.

The work carried out by Uccellini [25] defines explosive cyclogenesis as a cyclone which is subject to a deepening of at least 24 hPa in 24 hours.

There are some notable differences between "ordinary" cyclones, the majority of all cyclones, and these less frequent events. One of the most significant differences is that cyclones with explosive dynamics not only deepen faster, but also for a longer time than "ordinary" cyclones. The prevailing opinion is that these storms are the manifestation of physical and dynamic processes that occur to some extent in all cyclones, but which are particularly vigorous in explosive deepening. Many scientists have wondered what ordinary processes make these storms so powerful.

A very important variable is the latent heat released into the atmosphere, which can:

1. add energy to the system

2. focus and intensy the vertical motion through a local reduction of static stability in saturated updraft

3. influences the structure and dynamics of the largest cyclone scale in order to intensify the cyclogenetic effect of normal dynamic processes

As schematically shown in Figure 1.7, the winds in the boundary layer directed towards the Pole, on the eastern side of the cyclone, heat the lower troposphere, located on the warm sector, through advection of warm air and diabatic heating resulting from the release of latent heat in ascending moist air. This heating leads to an increase in the surface temperature gradient and of warm advection, which, where it is more intense, is often associated with more intense vertical upward motions. An intense upward motion leads to a more intense conversion of baroclinic energy and often to a deeper cyclone, whose intense circulation, in turn, causes positive feedback: since water vapor is not a passive scalar[1], its phase change, with an increase in the amount of latent heat released into the atmosphere, tends to concentrate normal baroclinic processes on smaller scales. This process leads to feedback that favors the contraction of the scale and the intensification of these storms up to an explosive dynamics. Hence, storms with explosive dynamics do not develop as a consequence of "special" dynamic processes, but rather as a result of intense interactions between "ordinary" physical and dynamic processes which operate, to a certain extent, in all mid-latitude cyclones.

---

[1]If the scalar in consideration has no influence on the dynamics of fluid motion, it is called passive scalar.
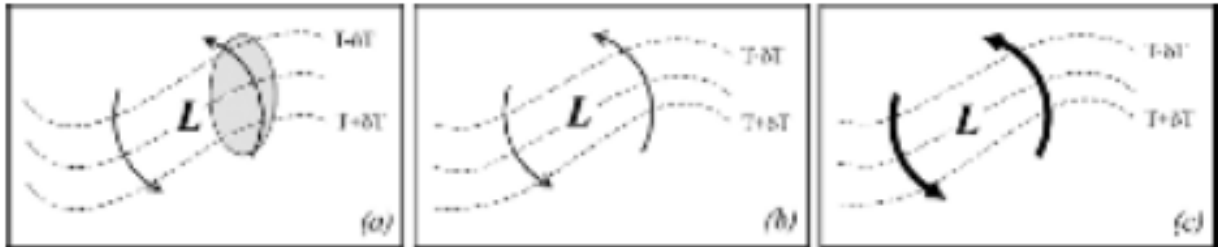
Figure 1.7: Schematic illustration of the influence that sensible and latent heat fluxes in the planetary boundary layer can have on the magnitude of the lower tropospheric temperature advection east of the surface cyclone center [16].
(a) Prior to the influence of the heat fluxes a uniform temperature gradient exists. Dashed lines are isotherms, "L" is the location of the sea-level pressure minimum, arrows represent the flow around the cyclone and the gray shaded area is the location where heat fluxes will warm the boundary layer.
(b) Increased temperature gradient results from the heating in the boundary layer. Intensified lower tropospheric warm air advection intensifies the cyclone.
(c) More intense cyclone leads to more intense lower tropospheric winds (bolder arrows) and increased warm air advection.

Chapter 2

Q-vector theory

The Q-vectors are not directly measurable physical quantities but help to explain the physical processes in the atmosphere and are useful diagnostic tools. Their size is proportional to the horizontal variation rate of the geostrophic wind at a certain level and to the horizontal temperature gradient. Q-vector can be traced at specific atmospheric levels and the divergence field of the Q-vector represents the forcing for vertical motions at synoptic scale. In general, the convergence of the Q-vector represents a forcing, on synoptic scale, for the ascending motions while the divergence of the Q-vector represents a forcing for the descending motions.

2.1   Mathematical treatment of the Q-Vector

To obtain the mathematical expression of the Q-vector, its horizontal components are calculated separately below.
To proceed to the mathematical derivation we start from the equation of horizontal motion in isobaric coordinates

$$\frac{D\vec{V}}{Dt} + f\hat{k} \times \vec{V} = -\nabla\phi \tag{2.1}$$

where

$$\vec{V} = \vec{V_g} + \vec{V_a} \tag{2.2a}$$

$$f = f_0 + \beta y \tag{2.2b}$$

where f_0 it is the parameter of Coriolis that at mid-latitudes holds 10^{-4} rad/s and $\beta = (\frac{df}{dy})_\phi$ e ϕ represents latitude.

Replacing the equation (2.2a) and the (2.2b) in the equation (2.1) (APPENDIX A):

$$\frac{D_g\vec{V_g}}{Dt} = -f_0\hat{k} \times \vec{V_a} - \beta y\hat{k} \times \vec{V_g} \tag{2.3}$$

In addition to this equation, the equation of *thermodynamic energy* is also used (APPENDIX B):

$$\frac{D_g u_g}{Dt} - f_0 v_a - \beta y v_g = 0 \tag{2.4}$$

$$\frac{D_g v_g}{Dt} + f_0 u_a + \beta y u_g = 0 \tag{2.5}$$

$$\frac{D_g T}{Dt} - S_p \omega - \frac{J}{c_p} = 0 \tag{2.6}$$

where $S_p = -T\frac{\partial ln\theta}{\partial p}$ is the parameter of stability, J represents the heating rate per unit of mass due to radiation, conduction and latent heat released (diabatic heating), $\omega = \frac{Dp}{Dt}$ represents the variation of the pressure following the motion (the vertical velocity in an isobaric coordinate system) and finally c_p is the specific heat at constant volume.

The aim is to find the components of the Q-vector, removing the temporal dependency.

The horizontal y-component of the Q-vector follows from $p\frac{\partial}{\partial p}(2.4) - (\frac{R}{f_0})\frac{\partial}{\partial y}(2.6)$ (APPENDIX C):

$$Q_y = -\frac{R}{p}\left[\frac{\partial u_g}{\partial y}\frac{\partial T}{\partial x} + \frac{\partial v_g}{\partial y}\frac{\partial T}{\partial y}\right] \tag{2.7}$$

The horizontal x-component, however, is calculated from $p\frac{\partial}{\partial p}(2.5) + (\frac{R}{f_0})\frac{\partial}{\partial x}(2.6)$:

$$Q_x = -\frac{R}{p}\left[\frac{\partial v_g}{\partial x}\frac{\partial T}{\partial y} + \frac{\partial u_g}{\partial x}\frac{\partial T}{\partial x}\right] \tag{2.8}$$

So, considering the newly derived components we get the **Q-vector**:

$$\begin{aligned}\vec{Q} = (Q_x, Q_y) &= -\frac{R}{p}\left(\frac{\partial v_g}{\partial x}\frac{\partial T}{\partial y} + \frac{\partial u_g}{\partial x}\frac{\partial T}{\partial x}, \frac{\partial u_g}{\partial y}\frac{\partial T}{\partial x} + \frac{\partial v_g}{\partial y}\frac{\partial T}{\partial y}\right) \\ &= -\frac{R}{p}\left(\frac{\partial \vec{V_g}}{\partial x}\cdot\nabla T, \frac{\partial \vec{V_g}}{\partial y}\cdot\nabla T\right)\end{aligned} \tag{2.9}$$

The definition of this variable allows to rewrite the equation called *omega equation* in terms of Q-vector (APPENDIX D):

$$\sigma\nabla^2\omega - f_0^2\frac{\partial^2\omega}{\partial p^2} = -2\nabla\cdot\vec{Q} - f_0\beta\frac{\partial v_g}{\partial p} - \frac{k}{p}\nabla^2 J \tag{2.10}$$

The equation (2.10) shows that vertical motions are forced by the sum of the divergence of the Q-vector, the Laplacian of diabatic warming, and a term related to the effect β which is generally small for synoptic scale motions. In all forms of the *omega equation*, the terms on the right side represent mechanisms that tend to break the geostrophic balance. Vertical motion (ω) is the effective response to this forcing and attempts to restore the balance of the geostrophic and thermal wind [11].

16

A different representation of the traditional quasi-geostrophic *omega equation*, even if it is an excellent diagnostic tool, is appropriate since the traditional formulation is not of immediate interpretation (for example, forcing terms tend to compensate because of opposite sign).

The advantages of the formulation in terms of Q-vector are [11]:

1. The vertical derivative does not come into play in the equation. Therefore, the Q-vector can be evaluated on single pressure surfaces, in layers (e.g. $850 - 700mb$, $700 - 500mb$) and in spatial height sections, as in AWIPS[1]. This allows the visualization of the depth and slope of the divergence/convergence fields of the Q-vector (forcing).

2. In the equation (2.10) (*omega equation* with the Q-vector) there is no partial compensation between two terms as in the traditional form of the quasi-geostrophic *omega equation*.

3. No term are overlooked in equation (2.10). However, the QG system (quasi-geostrophic) neglects temporal changes of ageostrophic wind, friction, diabatic effects and vertical advection of ω, which can sometimes be significant and which are present in this formulation.

4. The Q-vector are closely related to the ageostrophic flow. The amplitude of the Q-vector is approximately proportional to the ageostrophic horizontal wind.

5. Where the Q-vector points perpendicular to the isotherms from cold to warm air (from warm to cold), frontogenesis or intensification of the thermal gradient (frontolysis or dissipation of the thermal gradient) is implicit. Where frontogenesis is indicated, baroclinicity, wind convergence and vertical motions are increasing, with the available potential energy converted into kinetic energy.

---

[1] AWIPS-*Advanced Weather Interactive Processing System* is a meteorological visualization and analysis package, originally developed by the National Weather Service and Raytheon, modified and repackaged by Unidata to support non-operational use in research and education by UCAR member institutions. Further explanations at the following link `https://www.unidata.ucar.edu/software/awips2/`

2.2 Applications of the Q-vector

The direction and size of the Q-vector at a given point on a weather map can be estimated by referring, for example, to a Cartesian coordinate system in which the x-axis is parallel to the local isotherm with cold air on the left.
The Q-vector equation can be written as follows:

$$\vec{Q} = -\frac{R}{p}\frac{\partial T}{\partial y}\left(\frac{\partial v_g}{\partial x}\vec{i} + \frac{\partial u_g}{\partial x}\vec{j}\right) \qquad (2.11)$$

or in vector form:

$$\vec{Q} = -\frac{R}{p}\left|\frac{\partial T}{\partial y}\right|\left(\vec{k} \times \frac{\partial \vec{v_g}}{\partial x}\right) \qquad (2.12)$$

The Q-vector can be obtained by evaluating the variation of $\vec{V_g}$ along the isotherm (with cold air on the left). Identified the vector representing the geostrophic wind variation, rotate it by 90° clockwise multiply by $|\partial T/\partial y|$ and obtain the Q-vector. Two simple cases are reported, which verify a decrease in temperature towards the north, shown in Figures 2.1 and 2.2, where the Q-vector, and therefore the forcing of vertical motion, can be estimated with the help of equation (2.12).
The Figure 2.1 shows an idealized model of cyclones and anticyclones in a slightly disturbed westerly thermal wind. Near the low pressure center, the variation of the geostrophic wind that moves eastward along the isotherm (i.e. with cold air to the left) points north and a rotation of 90° clockwise produces a Q-vector parallel to the thermal wind. In high pressures, for the same reasoning, the Q-vector are opposed to the thermal wind.
In the situation shown in Figure 2.2, the geostrophic flow is convergent and the variation of the geostrophic wind is parallel to the isotherms, and by rotating 90° clockwise the Q-vector turns out to be normal to the isotherms. In both Figures 2.1 and 2.2 in the convergence region of the Q-vector there is vertical ascending motion, therefore stretching of the vorticity in the air column below; cyclonic vorticity will therefore tend to increase (see Figure 2.3)
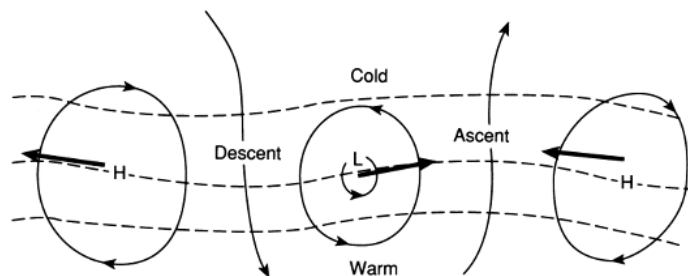

Figure 2.1: Q-vector (bold arrows) for an idealized model of isobars (black lines) and isotherms (dotted black lines) for a family of cyclones and anticyclones [13].
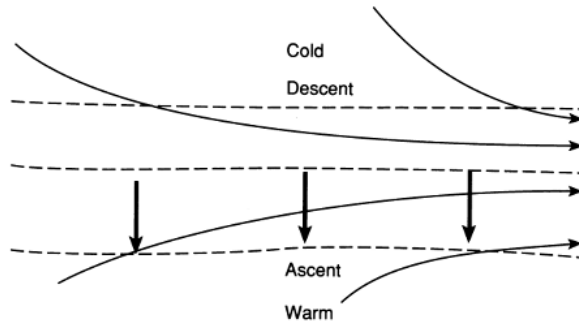
Figure 2.2: Orientation of the Q-vector (bold arrows) for the convergent flow (*jet entrance*). The dotted lines are isotherms [13].
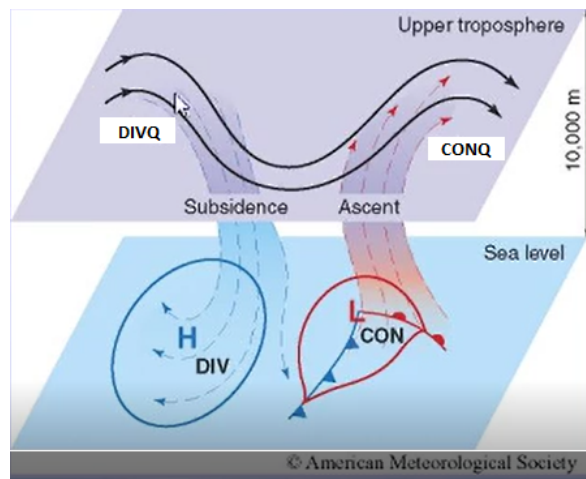

Figure 2.3: At the ground there are two areas, one of high and one of low pressure, and near the tropopause there is the ridge. Near the ascending branch of the ridge (descending branch of the ridge) there is convergence of the Q-vector (divergence of Q-vector) and therefore ascending motions occur (descending motions) with formation at the ground of a minimum of pressure (high pressure).

2.3 Fronts and Frontogenesis

A *front* is a region whose main structural and dynamic characteristic is the contrast of temperature (or density) (Figure 2.4).
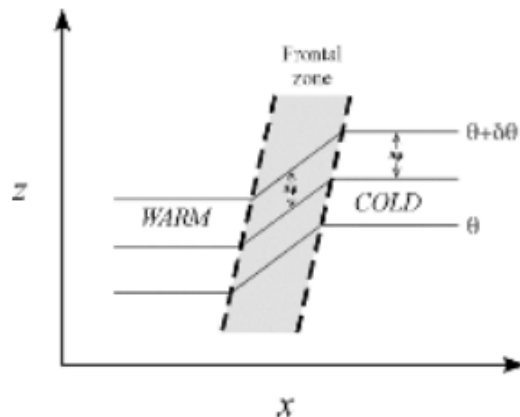

Figure 2.4: Isentropic lines associated with a first-order front [16].

The formation of a front, a process called frontogenesis, usually occurs in association with the development of baroclinic waves. Even if on average baroclinic disturbances carry heat along the average temperature gradient and tend to weaken the temperature difference between the polar and tropical regions, locally the flow associated with baroclinic disturbances can actually increase the temperature gradient.

If, for example, with a horizontal advection process, the temperature gradient (∇T) increases, then also the wind speed necessarily increases. A more intense jet causes a greater vorticity and therefore there is an increase in wind divergence. Remember that from the frictionless vorticity equation, vorticity can change only because of the divergence of the wind ($\frac{d\zeta}{dt} = -f(\nabla \cdot V)$). The presence of divergence in the high tropospheric levels causes a vertical upward movement. Therefore, an increase in the temperature gradient requires the production of vertical circulation in the atmosphere in an approximate balance of the thermal wind.

The influence of a purely geostrophic flow on the temperature gradient was given in terms of the Q-vector whose divergence forces a secondary ageostrophic circulation. The nature of the secondary flow can be deduced from the Q-vector model illustrated in Figure 2.5.
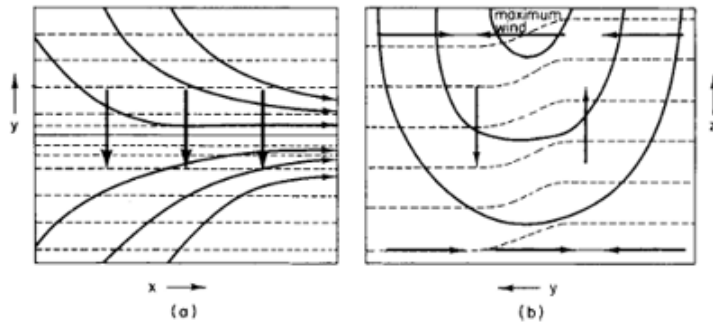
Figure 2.5: (a) Horizontal flow, isothermal lines and Q-vector in a frontogenetic zone. (b) Vertical cross section of confluence. Isotaches (black lines), isotherms (dashed lines), vertical and transverse motions (arrows) [21].

In the Figure 2.5 b), the vertical motion associated with the ageostrophic circulation tends to weaken the front in the mid-troposphere due to the adiabatic temperature variations (adiabatic heating on the cold side of the front and adiabatic cooling on the hot side). For this reason, the fronts are more intense in the lower troposphere and close to the tropopause.

The secondary circulation associated with frontogenesis is necessary to maintain the balance of the thermal wind between the flow along the front and perpendicular to the temperature gradient near the front in the presence of advective processes which tend to destroy this balance.

The thermal wind relationship requires that the fronts (regions of large ∇T) are associated with a strong vertical shear of the geostrophic wind. In the Figure 2.6 an idealized vertical section is shown through a frontal area. Note that the size of ∇T is greater near the surface and that the frontal area is characterized by the stronger vertical shear.
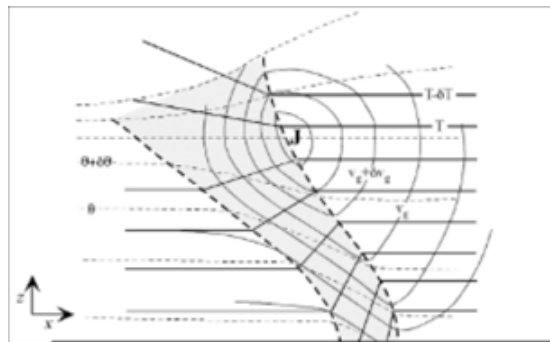
Figure 2.6: Idealized vertical cross-section through a frontal zone. Gray solid lines are isotachs of the geostrophic wind into the page with 'J' indicating the position of the wind maxima. Black solid lines are isotherms and thin dashed lines are isentropes. Gray shaded region with thick dashed border represents the idealized frontal zone [16].

To analyze the dynamics of cross-frontal circulation, it is convenient to use the Boussinesq approximation, in which the density is replaced by a constant reference value ρ_0 except where it appears in the buoyancy force. This approximation simplifies the

equations of motion without affecting the main characteristics of the results. It is also useful to replace the total pressure and density fields with deviations from their standard atmosphere values.

The circulation is created in a cross-frontal direction; therefore, assuming that the direction of motion of the front is along the x axis, the secondary circulation is two-dimensional in the y and z plane.

From a mathematical point of view, the circulation on the y axis is expressed by the equation 5.40 and on the z axis from the equation 5.42 (shown in APPENDIX E):

$$\frac{D}{Dt}\left(\frac{\partial b}{\partial y}\right) = Q_y - \frac{\partial v_a}{\partial y}\frac{\partial b}{\partial y} - \frac{\partial w}{\partial y}\left(N^2 + \frac{\partial b}{\partial z}\right) \tag{2.13}$$

$$\frac{D}{Dt}\left(f\frac{\partial u_g}{\partial z}\right) = Q_y - \frac{\partial v_a}{\partial z}f\left(f - \frac{\partial u_g}{\partial y}\right) + \frac{\partial w}{\partial z}\frac{\partial b}{\partial y} \tag{2.14}$$

where

$$Q_y = -\frac{\partial u_g}{\partial y}\frac{\partial b}{\partial x} - \frac{\partial v_g}{\partial y}\frac{\partial b}{\partial y} \tag{2.15}$$

is the y-component of the Q-vector previously discussed, but expressed in the Boussinesq approximation.

For a situation like the one in Figure 2.7 b), with both $\partial v_g/\partial y$ e $\partial b/\partial y$ negative, the forcing term Q_y is negative in the frontal region.

Since Q_y represents the "quasi-geostrophic forcing", it can be seen from the equation 5.40 that is acts to decrease the cross-frontal temperature gradient $\frac{\partial b}{\partial y}$ and the vertical shear $\frac{\partial u_g}{\partial z}$ (equation 5.42). The above effects tend to destroy the thermal wind balance / geostrophic balance. In order to maintain the geostrophic balance for the u-component of the wind (as hypothesized by the *scaling analysis* in APPENDIX E), for consistency the non-geostrophic component of the motion (i.e. the secondary circulation) must counterbalance the effect of the geostrophic forcing:
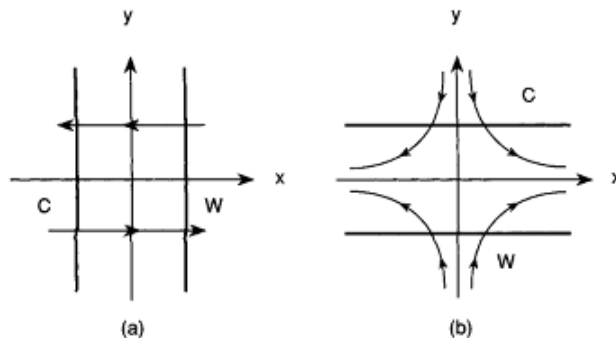
$$\frac{Du_g}{Dt} - fv_a = 0 \tag{2.16}$$

Figure 2.7: Frontogenetic flow configurations: (a) Horizontal shear deformation-gradient rotated and intensified by shear. (b) Horizontal stretching deformation-temperature advected [13].

22
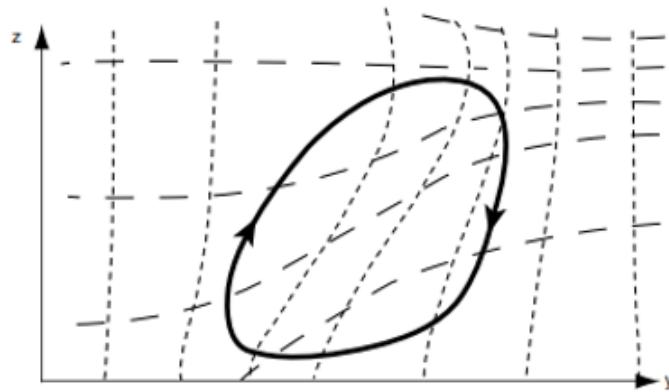
Figure 2.8: Relationship of the ageostrophic circulation (black curve with arrows) in two-dimensional frontogenesis with the potential temperature field (lines with long dashes) and the absolute moment field (short dashes). Cold air is on the right and warm air on the left. Note the inclination of the circulation towards the cold air side and the increase of the absolute moment gradient and the potential temperature in the frontal zone [13].

The term "frontogenetic" refers to any process that acts to increase the temperature gradient.

More specifically (to facilitate physical interpretation), reference is made to any horizontal advective process which acts to increase ∇T as horizontal frontogenesis.

A function of frontogenesis can be defined:

$$F = \frac{d|\nabla_p \theta|}{dt} \tag{2.17}$$

which represents the Lagrangian rate of change of the potential temperature gradient measured at an isobaric surface.

Without loss of physical intuition, we can consider the unidirectional version of the equation (2.17) to understand what are the main contributions that represent frontogenesis. Therefore, consider the processes that can change the temperature gradient in the x-direction using:

$$F_x = \frac{d}{dt}\left(\frac{\partial\theta}{\partial x}\right) \tag{2.18}$$

where

$$\frac{d}{dt} = \frac{\partial}{\partial t} + u\frac{\partial}{\partial x} + v\frac{\partial}{\partial y} + \omega\frac{\partial}{\partial p} \tag{2.19}$$

then:

$$F_x = \frac{d}{dt}\left(\frac{\partial\theta}{\partial x}\right) = \frac{\partial}{\partial x}\left(\frac{d\theta}{dt}\right) - \frac{\partial u}{\partial x}\left(\frac{\partial\theta}{\partial x}\right) - \frac{\partial v}{\partial x}\left(\frac{\partial\theta}{\partial y}\right) - \frac{\partial\omega}{\partial x}\left(\frac{\partial\theta}{\partial p}\right) \tag{2.20}$$

There are four physical processes, represented by the four terms on the right in the equation (2.20), which contribute to an increase of $\left(\frac{\partial\theta}{\partial x}\right)$.

- The first of these processes is the effect of across-front gradients in diabatic heating, represented by $\frac{\partial}{\partial x}\left(\frac{d\theta}{dt}\right)$.
  If there is latent heat release in ascending air on the warm side of potential temperature gradient, then $\frac{\partial}{\partial x}\left(\frac{d\theta}{dt}\right) > 0$. Consequently, such a distribution of latent heat release is frontogenetic. Utilizing the same expression we can consider the effect of differential cloud cover on frontal intensity. If the warm side is cloudy and the cold side clear, then differential insolation during the day renders $\frac{\partial}{\partial x}\left(\frac{d\theta}{dt}\right) < 0$ and daytime heating is frontolytic under such circumstances. Under the same distribution of clouds during the night, the cold side cools more rapidly than the warm side so that $\frac{\partial}{\partial x}\left(\frac{d\theta}{dt}\right) > 0$ and so the cloud cover promotes frontogenesis.

- The second term, on the other hand, can be analysed considering the confluent flow shown in the Figure 2.9 where you notice that $\frac{\partial\theta}{\partial x} > 0$. The winds are distributed such that $\frac{\partial u}{\partial x} < 0$. Overall, then, the effect of the confluent wind

field shown in Figure 2.9 is to promote frontogenesis. One can imagine the wind field acting to push the isentropes closer together in the horizontal, thereby increasing $|\left(\frac{\partial\theta}{\partial x}\right)|$.

- The effect of horizontal shearing on $\frac{\partial\theta}{\partial x}$ is represented by the third term and is illustrated in Figure 2.10. In this instance, the isentropes are aligned at a small angle to both the x and y axes in such a way that $\frac{\partial\theta}{\partial y} < 0$. Given the indicated winds, it is clear that $\frac{\partial v}{\partial x} > 0$ as well, meaning that the entire shearing term is positive. Thus, such shearing will act to increase $\frac{\partial\theta}{\partial x}$ by rotating the isotherms into a more meridional orientation. This increase in $\frac{\partial\theta}{\partial x}$ does not, however, represent a decrease in the absolute distance between successive isentropes (as was the case for both of the prior physical mechanisms).

- The effect of vertical tilting is represented by the fourth term.
  A thermally direct vertical circulation, along with a frontal bundle of isentropes, is illustrated in the vertical cross-section depicted in Figure 2.11. In a statically stable atmosphere, $\frac{\partial\theta}{\partial p}$ must be negative. Recalling that upward vertical motion is consistent with negative omega and vice versa, $\frac{\partial\omega}{\partial x} < 0$ for the situation shown in Figure 2.11. Thus, the entire vertical tilting term is negative, suggesting that a thermally direct vertical circulation acts to decrease $\frac{\partial\theta}{\partial x}$ by rotating the isentropes into a more nearly horizontal orientation. From that perspective, the rising warm air cools by expansion while the sinking cold air warms by compression. Thus, the originally warm air is made colder while the originally cold air is made warmer under the influence of the thermally direct vertical motions.
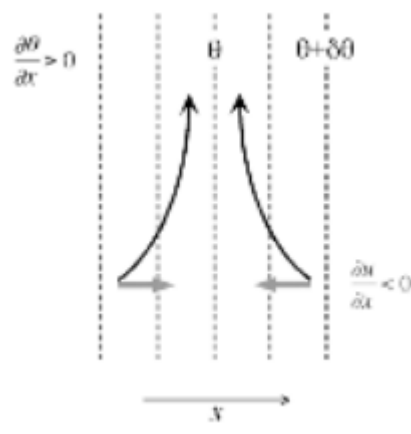
Figure 2.9: Confluent horizontal flow that acts on north-south oriented isentropics. The gray arrows represent the wind in the x direction [16].
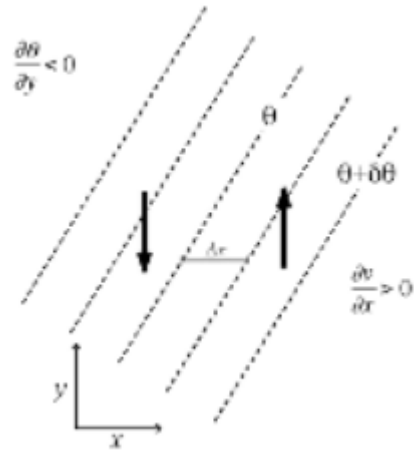
Figure 2.10: Effect of the horizontal shear on $\left(\frac{\partial\theta}{\partial x}\right)$. The black arrows represent the wind in the y direction [16].
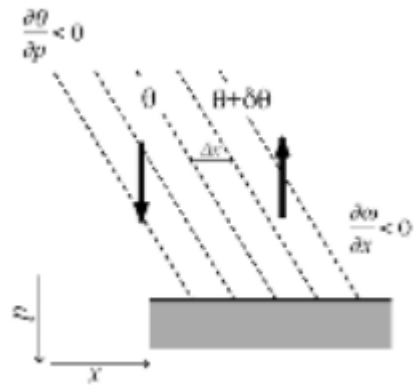

Figure 2.11: Tilt effect on $\left(\frac{\partial\theta}{\partial p}\right)$. The black arrows represent vertical movements upwards and downwards [16].

For many types of frontal development, it is sufficient to consider the 2-D version in which the diabatic and inclination terms are neglected.

The resulting expression is:

$$F = \frac{1}{|\nabla\theta|}\left[-\left(\frac{\partial\theta}{\partial x}\right)\left(\frac{\partial u}{\partial x}\frac{\partial\theta}{\partial x} + \frac{\partial v}{\partial x}\frac{\partial\theta}{\partial y}\right) - \left(\frac{\partial\theta}{\partial x}\right)\left(\frac{\partial u}{\partial y}\frac{\partial\theta}{\partial x} + \frac{\partial v}{\partial y}\frac{\partial\theta}{\partial y}\right)\right] \qquad (2.21)$$

The formulation is also reported using the geostrophic wind instead of the total wind:

$$F = \frac{1}{|\nabla\theta|}\left[-\left(\frac{\partial\theta}{\partial x}\right)\left(\frac{\partial u_g}{\partial x}\frac{\partial\theta}{\partial x} + \frac{\partial v_g}{\partial x}\frac{\partial\theta}{\partial y}\right) - \left(\frac{\partial\theta}{\partial x}\right)\left(\frac{\partial u_g}{\partial y}\frac{\partial\theta}{\partial x} + \frac{\partial v_g}{\partial y}\frac{\partial\theta}{\partial y}\right)\right] \qquad (2.22)$$

Looking at the right side of the equation (2.22), note how the terms in square brackets multiplied by $\frac{\partial\theta}{\partial x}$ represent the horizontal components of the Q-vector multiplied by p/R. The only difference is in the temperature that is used; for the calculation of the Q-vector the temperature is used instead of the potential temperature, used for frontogenesis. Graphing the equation (2.22), in any place where the Q-vector points through the isentropics from cold to warm air will be associated with horizontal frontogenesis and F will be positive. In such places, geostrophic winds are advecting θ to increase $|\nabla\theta|$ and a thermally directed vertical circulation will develop where warm air will rise in a convergent zone of Q-vector in the medium-high tropospheric levels and descent of cold air in an area where the Q-vector is divergent.

The equation (2.22) will be used to calculate the frontogenesis of two cyclones to compare their Q-vector values.

Chapter 3

Comparison of the Q-vector in some cases of cyclogenesis

3.1 Cyclone Vaia, *28-29 October 2018*

Introduction

In this chapter, three cyclones of different characteristics were taken into consideration and compared with the cyclone Vaia, which produced significant damage in North-Eastern Italy at the end of October 2018. In particular, the respective Q-vector and the horizontal gradient of equivalent potential temperature at $850hPa$ were compared. The Q-vector is a diagnostic tool developed in the context of the quasi-geostrophic theory, therefore it is suitable especially for the synoptic scales. Since it may display present a noisy field if represented at high resolution, it was necessary to use a low resolution *dataset* for its computation: it was decided to use the NCEP (*National Center for Environmental Prediction*) reanalysis (available from the (`http://www.esrl.noaa.gov/psd/data/gridded/data.ncep.reanalysis2.pressure.html`)) with a horizontal resolution of 2.5 degrees. This choice, however, necessarily imposes a lower resolution of all the meteorological fields at the ground including the mean sea level pressure, with the consequence that, for example, the minimum pressure value of the low results strongly underestimated. Anyway, the objective of the present analysis, is to identify the order of magnitude of the Q-vector for each event and to make a comparison between the various cases, rather than focusing on the absolute values, which by the way is sensitive to the resolution of the dataset used.

In paragraphs 2.1 and 2.2, for each event, after a brief analysis of the synoptic scenario, the temporal evolution maps of the most significant variables are shown for an analysis of the conditions favorable to frontogenesis. In particular, the Q-vector and its divergence were analyzed: the Q-vector provides information on frontogenesis, while its divergence is associated with the intensity of vertical motions (see chapter 2). In addition, other graphs are drawn reporting:

1. Temporal evolution of the low

2. The Q-vector module

3. The value of the maximum convergence of the Q-vector

identified following the trajectory of the cyclone from its formation to the filling phase.

Synoptic analysis

Between 27 and 29 October, the Western Mediterranean and Northern Italian regions in particular were affected by the passage of an intense low-pressure system (Figure 3.1 a)) which caused sea storm, heavy precipitation, floods, and huge damage due to fierce winds that reached storm intensity ($103 - 117$ km/h according to the classification of the Beaufort scale).

The synoptic scenario in the days preceding the event was characterized by the presence of a high pressure ridge over Eastern Europe and by an Atlantic trough approaching the Western European coasts. On the day of 28 October this trough extended over the Iberian Peninsula, but its eastward progression was hampered by the presence of high pressure over the Balkans. Thus, the trough remained stationary, and deepened over North Africa, forcing intense humid currents from African tropical regions towards the Mediterranean and the formation of a secondary cyclone in the lee of the Atlas chain. The trough subsequently (Figure 3.1 b)) evolved in a " *cutoff*" and the surface low moved rapidly to the north, passing to the West of Sardinia and reaching Liguria in the afternoon of the 29 October. Only on 30 October it reached the North of the Alps. Cyclone dynamics were explosive[1] and the low reached a value of around 976 hPa on 29 October at 15 UTC between Sardinia and Corsica. The consequent formation of an intense pressure gradient (about 8 hPa between Provence and Corsica and up to 32 hPa between the Ligurian Sea and the Balkans) was responsible for the strong winds that caused serious and widespread damage.[18]

---

[1]Baric deepening of 24 hPa or more in 24 hours (see chapter 1).
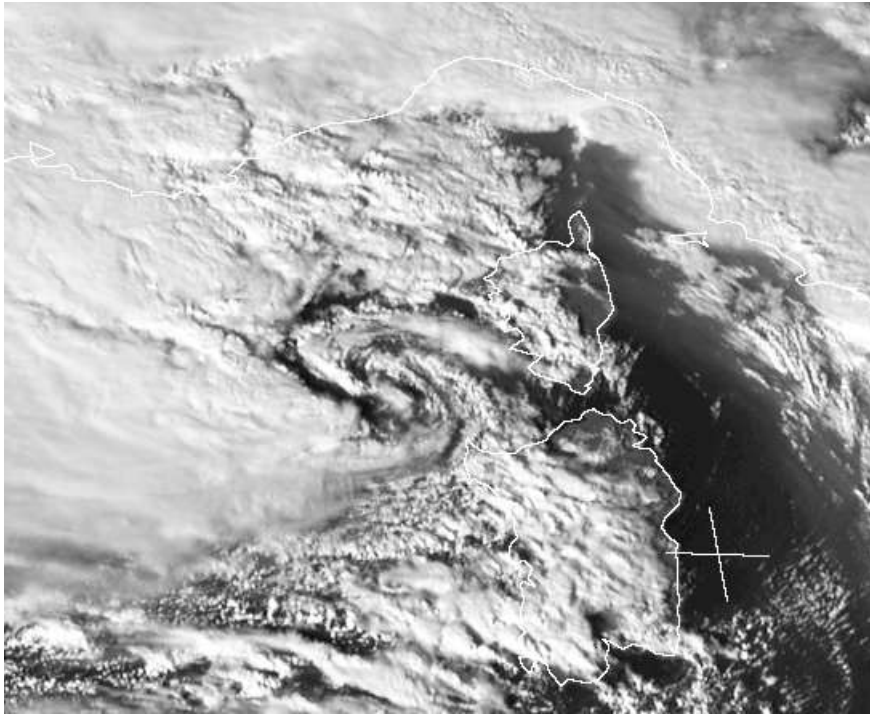
(a)
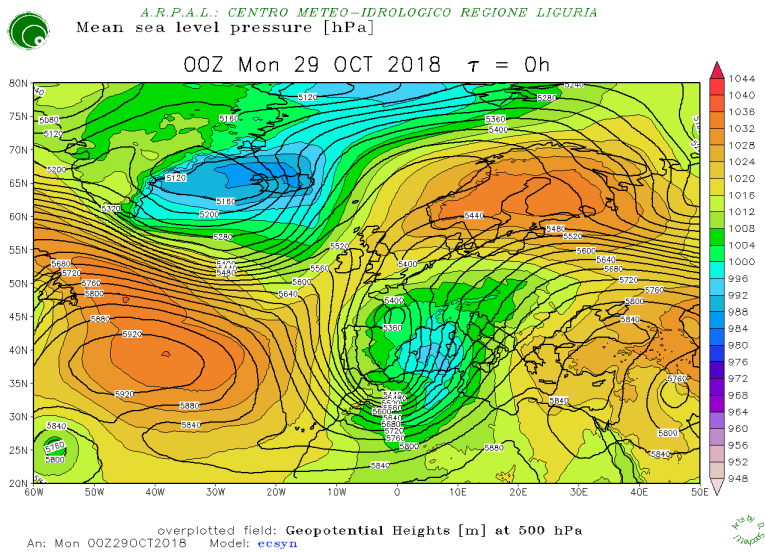
(b)

Figure 3.1:

a) Image acquired by the Meteosat Spinning Enhanced Visible satellite (wavelength 0.4 μm) at 14 UTC on 29 October 2018 (SEVIRI). The image highlights the presence of a cyclonic circulation to the West of Corsica (Cyclone Vaia).

b) Map of analysis of geopotential height at 500 hPa (lines) and of mean sea level pressure (shaded) at 00 UTC of 29 October 2018 of the global European reference ECSYN-*European Center SYNoptic model* model corresponding to the IFS model (model of the ECMWF with a resolution of about 10 km).

Mesoscale analysis of the event

The cyclonic event mainly affected the regions of Northern Italy: Liguria, Emilia-Romagna, Trentino Alto Adige, Friuli Venezia Giulia and Veneto.
Below are brief descriptions of the event and of the impacts on the territory of each region affected, extracted from the meteorological reports of each respective regional meteorological agency.

Liguria: Between 27 and 29 October, Liguria was affected by a phase of severe weather. On the day of 27 October, in the central part of Liguria heavy precipitation occurred due to the formation of a line of convergence at the ground between winds from the south-east and from the south-west, while on the day of 28 October light thunderstorms were observed only in the first part of the day. On the morning of 29 October, a *V-shape*[2] storm system developed, characterized by the formation of a *squall line*[3] starting from North-Western Corsica which reached La Spezia causing stationary stormy precipitations. Winds were measured at the ground from the south with sustained speed between strong ($75-88$ km/h according to the Beaufort scale classification) and stormy (or fortunale, $103-117$ km/h according to the Beaufort scale classification) with gusts up to hurricane (>118 km/h according to the Beaufort scale classification, gust over 180 km/h) for a duration of more than 12 hours. The most noteworthy phenomenon was the sea storm that occurred in the final part of the day which caused extensive damage along the coast, with a maximum recorded wave height of 10.3 m and a period of 12 s. [18]

---

[2]Powerful linear mesoscale storm systems with the characteristic "V" shape and passing over a particularly mild sea, can take on a self-healing nature and can also give rise to whirling phenomena. The most violent storms are at the vortex of the "V".

[3]Intense and extensive storm systems lined up for hundreds of kilometers. To form they need a cooler or colder air rush that invades a region occupied by warmer air. These systems always occur in correspondence with intense cold fronts. The storms of a *squall line* are generally preceded by the *shelf cloud* and when they pass they give rise to storms with hail, lightning floods and violent gusts.

Emilia-Romagna: The days of 27 and 28 October were characterized by widespread rainfall that affected the whole region. On 29 October, some precipitation systems passed through the region, transporting desert dust, a *squall line* in the afternoon and a further storm line in the evening were observed. The effects at the ground have been severe, from landslides, to floods and also damages due to the strong wind. [7]

Trentino Alto Adige-Friuli Venezia Giulia-Veneto: During 27 October, rainfall was more relevant for its persistence than for its intensity. Southerly winds were recorded, from strong $(50-61$ km/h according to the Beaufort scale classification) to locally very strong (more than 50 km/h of average wind, 102 km/h of maximum recorded gust) over the Prealps. The 28 and 29 October were characterized by heavy rain showers including thunderstorms and the persistence of strong winds $(50-61$ km/h according to the Beaufort scale classification) with gusts up to 192 km/h on 29 October, in the Prealps. The strong and persistent gusts caused the uprooting of trees on vast forest surfaces, devastating the arboreal heritage, which has become secular in some of the Dolomite forests. The strong Sirocco wind has also caused intense sea storm with widespread erosion of the beaches in almost all the Veneto coasts. [1]

Study of the evolution of the Q-vector following the trajectory of the cyclone

For each case study, two types of time evolution maps are reported. The first map (located on the left of the pages) shows the following variables:

1. Mean sea level pressure highlighting the surface cyclone (continuous black lines)

2. Potential temperature expressed in $°C$ at 850 hPa (magenta lines)

3. Q-vector (black arrows, with units of $2 * 10^{-11} \frac{m^2}{kgs}$ shown at the bottom right)

4. Divergence of the Q-vector (colored)

The second map (located to the right of the pages) shows:

1. Equivalent potential temperature at 850 hPa expressed in $°C$

2. Wind expressed in knots at 850 hPa

To study the temporal evolution of Vaia, the domain between the latitudes $20°N - 60°N$ and the longitudes $-25°W - 25°E$ was chosen in order to exclude the presence of other cyclonic structures. In the domain, as can be seen from the Figure 3.2 to the Figure 3.5, the lateral edges (5 degrees) lack the Q-vector and divergence data (present in each case analyzed). This is due to the calculation of the difference-centered derivatives necessary for the calculation of the Q-vector and its divergence. Each image shows the numerical values, following the trajectory of the cyclone, of the minimum pressure (mslp) (whose position is indicated by the blue point), the maximum Q-vector and the maximum convergence of the Q-vector (position indicated by the blue triangle).

To proceed with the analysis of the event, from Figure 3.2 to Figure 3.5, it is antici-
pated that the Q-vector, which provides information on baroclinicity, assumes values
of the order of magnitude between 10^{-13} to 10^{-11} $\frac{m^2}{kgs}$.

The cyclone Vaia shows a Q-vector of the order of magnitude of 10^{-11} $\frac{m^2}{kgs}$ for 30
consecutive hours, from before its formation (12 UTC of 28 October) up to six hours
before the maximum deepening, when the Q-vector values become of the order of
10^{-12} $\frac{m^2}{kgs}$ (18 UTC of 29 October) (from Figure 3.4 c) to Figure 3.5 a)). The maxi-
mum value of Q-vector is $1.44 * 10^{-11}$ $\frac{m^2}{kgs}$ reached at 18 UTC on 28 October (Figure
3.2 c)), 24 hours before the cyclone intensifies. As for the divergence of the Q-vector,
of about $-18 * 10^{-18}$ $\frac{m}{kgs}$, it is reached at 18 UTC on 28 October (Figure 3.2 c)).
The information that can be inferred on the basis of the comparison with the values
attained for the other cases (see following sections) are:

- The Q-vector values indicate that intense frontogenesis has occurred, associated
  with explosive cyclogenesis, that is the deepening in 24 h of 24 hPa [25].

- The divergence values (equal to $-18*10^{-18}$ $\frac{m}{kgs}$) indicate that ascending motions
  were not very intense since, through the analysis carried out in chapter 5, as in
  other cases values of $-30 * 10^{-18}$ $\frac{m}{kgs}$ were observed (SEE CHAPTER 5).

Figure 3.6, shows the evolution of the mean sea level pressure (blue line), the conver-
gence (negative divergence), multiplied by 10^{18} (green line) and the Q-vector module
in red, multiplied by 10^{11}.
A further consideration was made by analyzing this Figure 3.6:

- The absolute maximum of convergence of the Q-vector, associated with the
  upward vertical motions, is attained 24 hours before (18 UTC of the 28 October)
  of the maximum cyclonic deepening (18 UTC del 29 ottobre).

As for the θ_e[4], from panels b) and d) from Figure 3.2 to Figure 3.5, it is clear that
intense warm advection has occurred, reaching values of above 40° C at 850 hPa in
Northern Europe.

---

[4]Equivalent potential temperature.

(a)

(b)

(c)

(d)
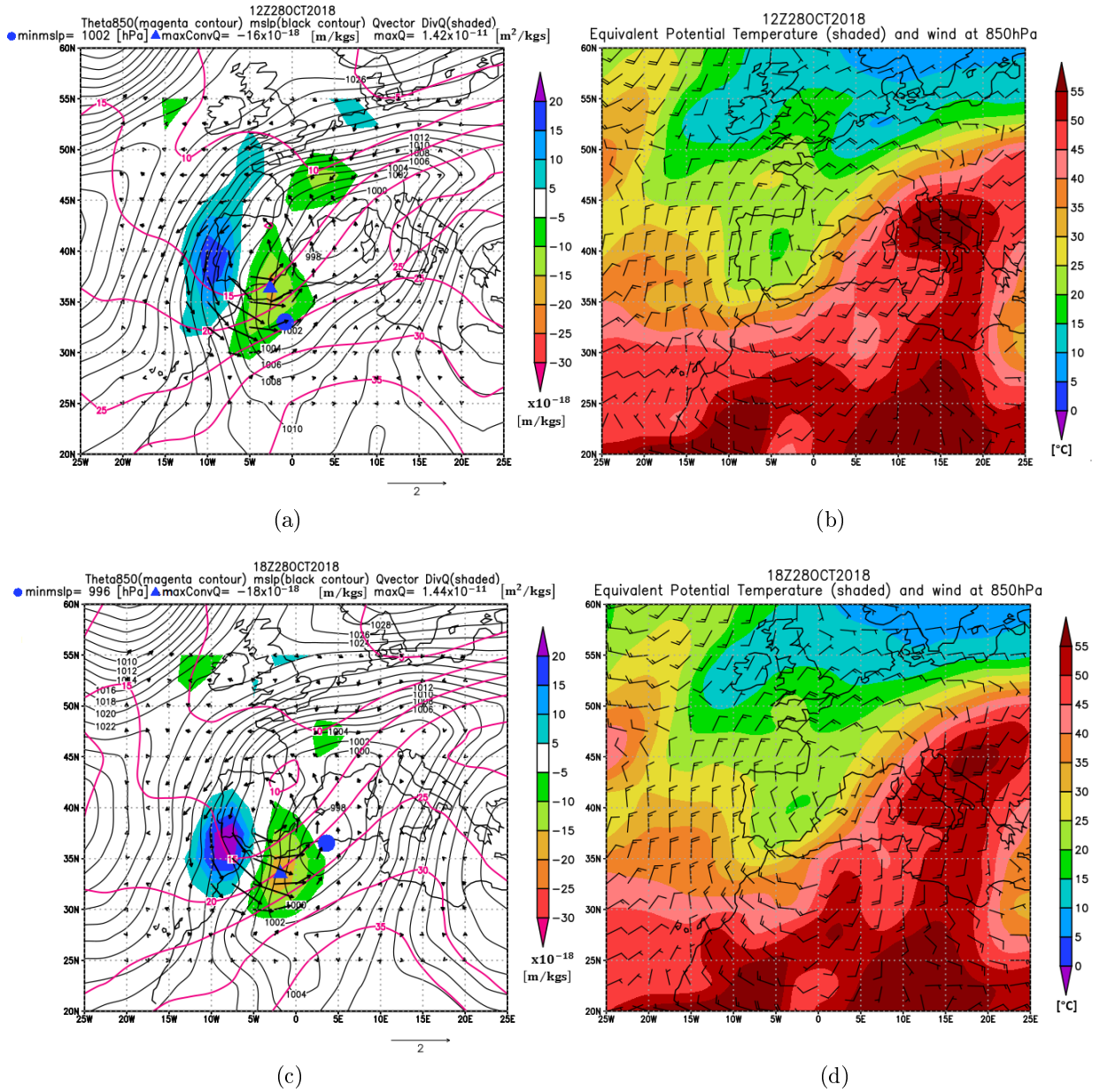
Figure 3.2:
a) e c) Map of mslp (black contour), Θ (850 hPa) (magenta contour), Q-vector (black arrows, with units of $2 * 10^{-11} \frac{m^2}{kgs}$) and Q-vector divergence (shaded) referring respectively to 12 and 18 UTC on 28 October 2018. The figure shows the numerical values assumed following the trajectory of the cyclone, the pressure low (mslp) (whose position is indicated by the blue dot), the maximum Q-vector present in the domain and the maximum convergence of the Q-vector multiplied by 10^{18} (position indicated by the blue triangle).
b) and d) θ_e at 850 hPa referring to 12 and 18 UTC respectively on 28 October 2018.

35

(a)

(b)

(c)

(d)

Figure 3.3:

a) e c) Map of mslp (black contour), Θ (850 hPa) (magenta contour), Q-vector (black arrows, with units of $2*10^{-11}\ \frac{m^2}{kgs}$) and Q-vector divergence (shaded) referring to 00 and 06 UTC respectively on 29 October 2018. The figure shows the numerical values assumed following the trajectory of the cyclone, the pressure low (mslp) (whose position is indicated by the blue dot), the maximum Q-vector present in the domain and the maximum convergence of the Q-vector multiplied by 10^{18} (position indicated by the blue triangle).

b) and d) θ_e at 850 hPa referring to 00 and 06 UTC respectively on 29 October 2018.
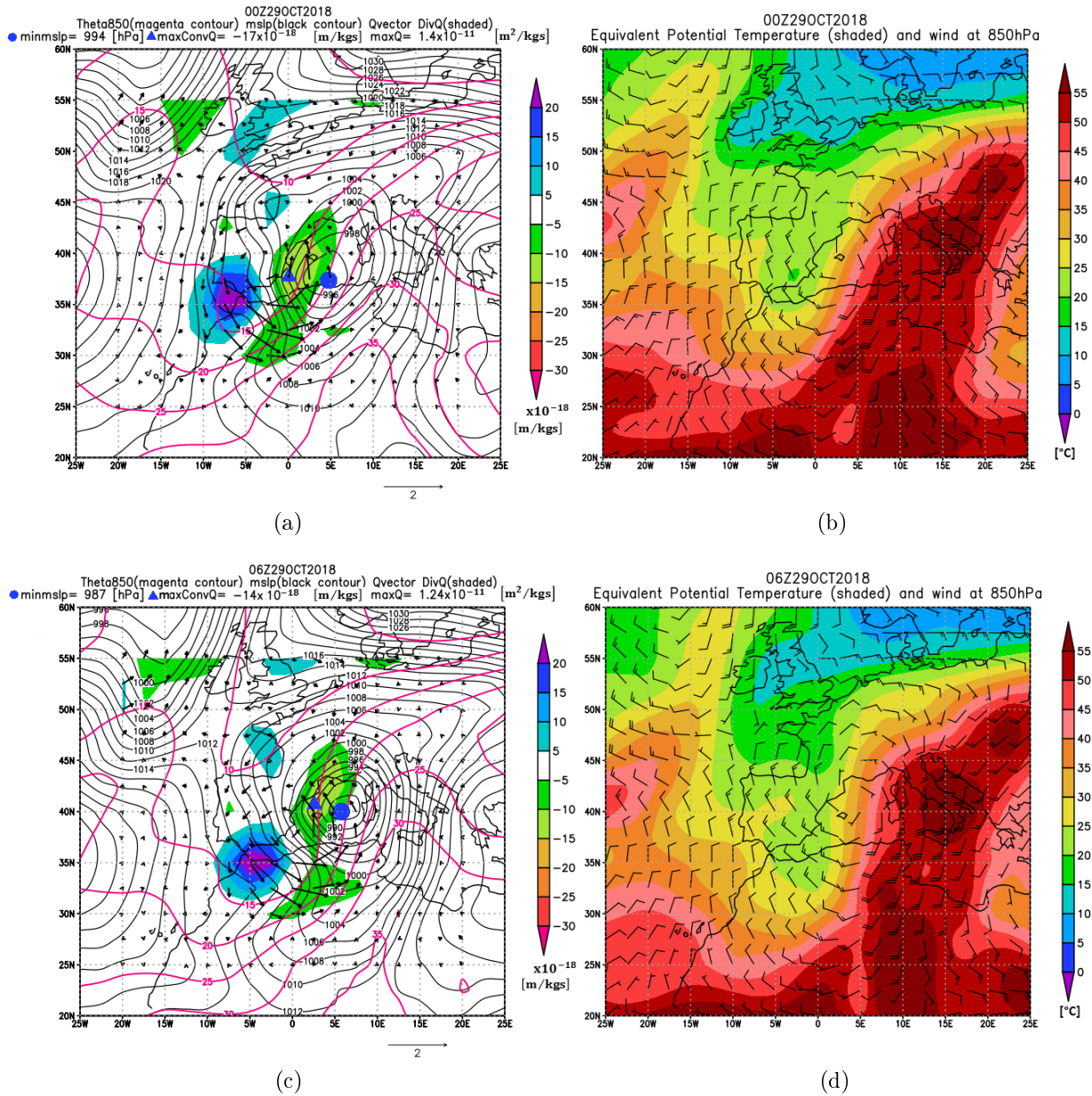
(a)

(b)

(c)

(d)

Figure 3.4:
a) e c) Map of mslp (black contour), Θ (850 hPa) (magenta contour), Q-vector (black arrows, with units of $2 * 10^{-11} \frac{m^2}{kgs}$) and Q-vector divergence (shaded) referring to 12 and 18 UTC respectively on 29 October 2018. The figure shows the numerical values assumed following the trajectory of the cyclone, the pressure low (mslp) (whose position is indicated by the blue dot), the maximum Q-vector present in the domain and the maximum convergence of the Q-vector multiplied by 10^{18} (position indicated by the blue triangle).
b) and d) θ_e at 850 hPa referring to 12 and 18 UTC respectively on 29 October 2018.

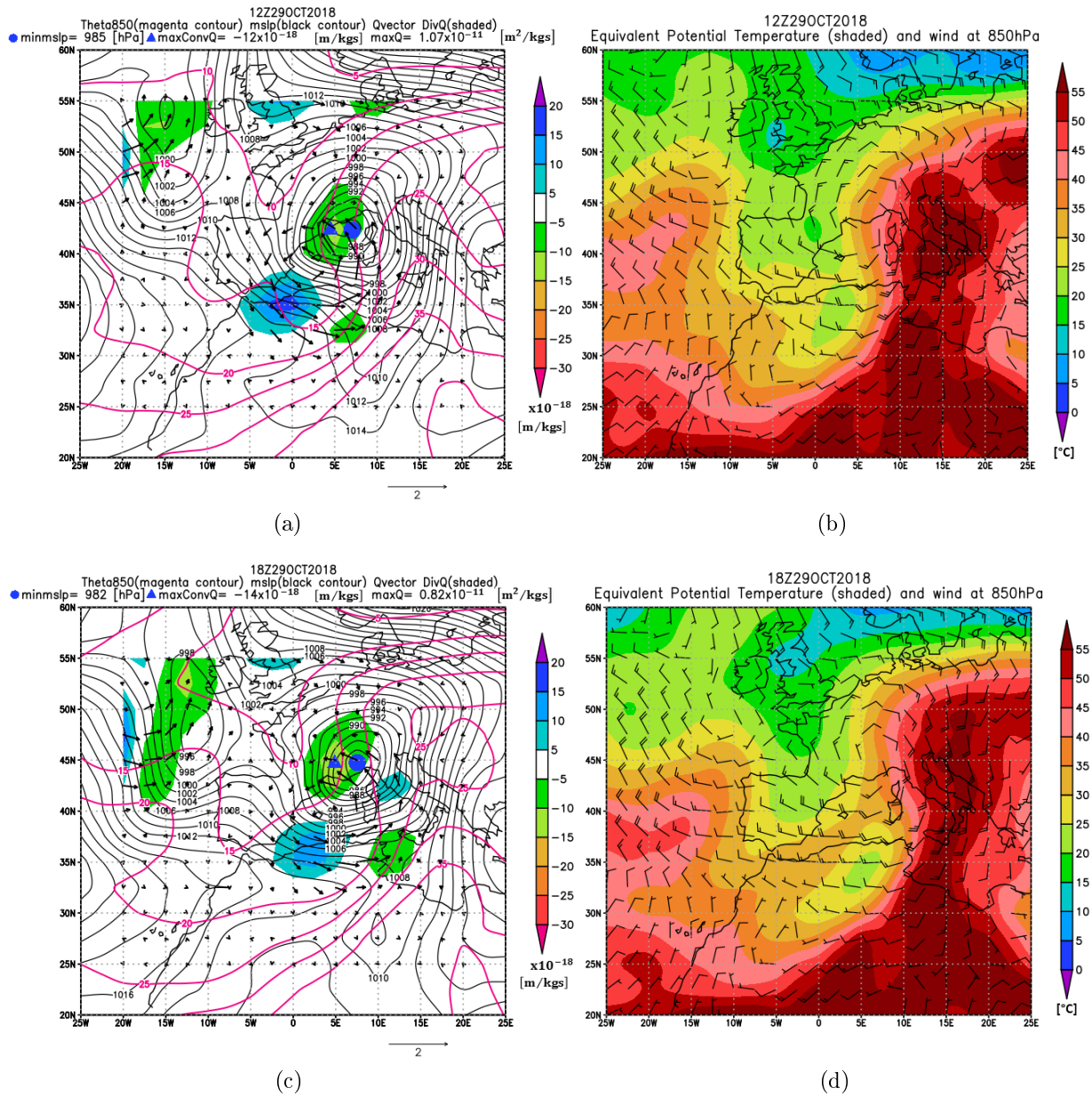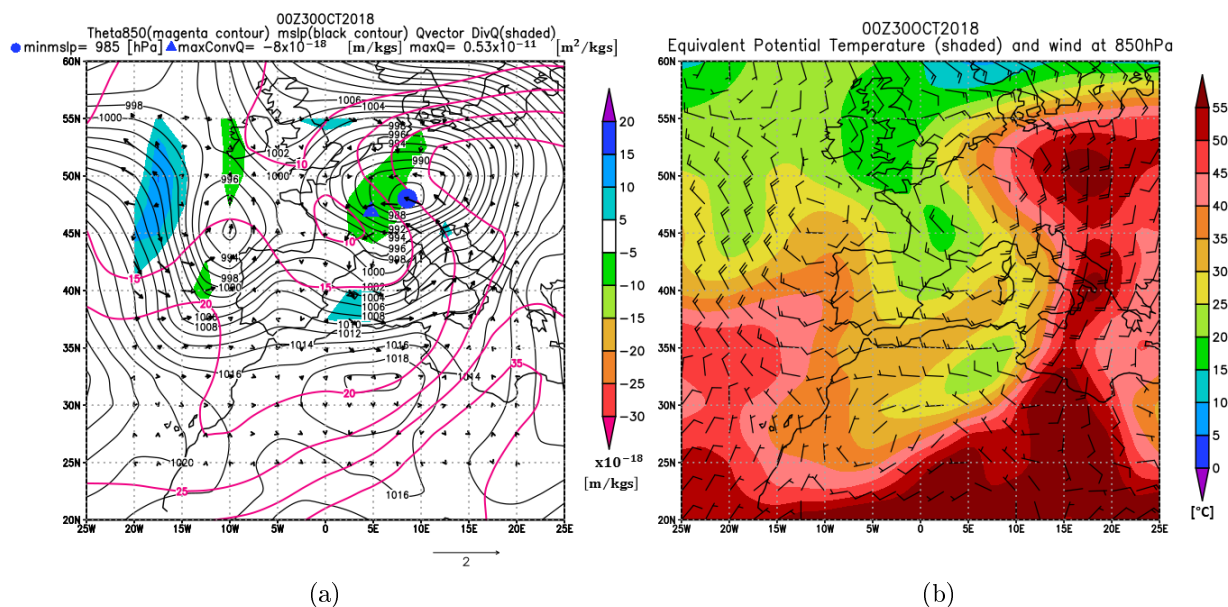(a)   (b)

Figure 3.5:
a) Map of mslp (black contour), Θ (850 hPa) (magenta contour), Q-vector (black arrows, with units of $2 * 10^{-11}$ $\frac{m^2}{kgs}$) and Q-vector divergence (shaded) at 00 UTC on 30 October 2018. The figure shows the numerical values assumed following the trajectory of the cyclone, the pressure low (mslp) (whose position is indicated by the blue dot), the maximum Q-vector present in the domain and the maximum convergence of the Q-vector multiplied by 10^{18} (position indicated by the blue triangle).
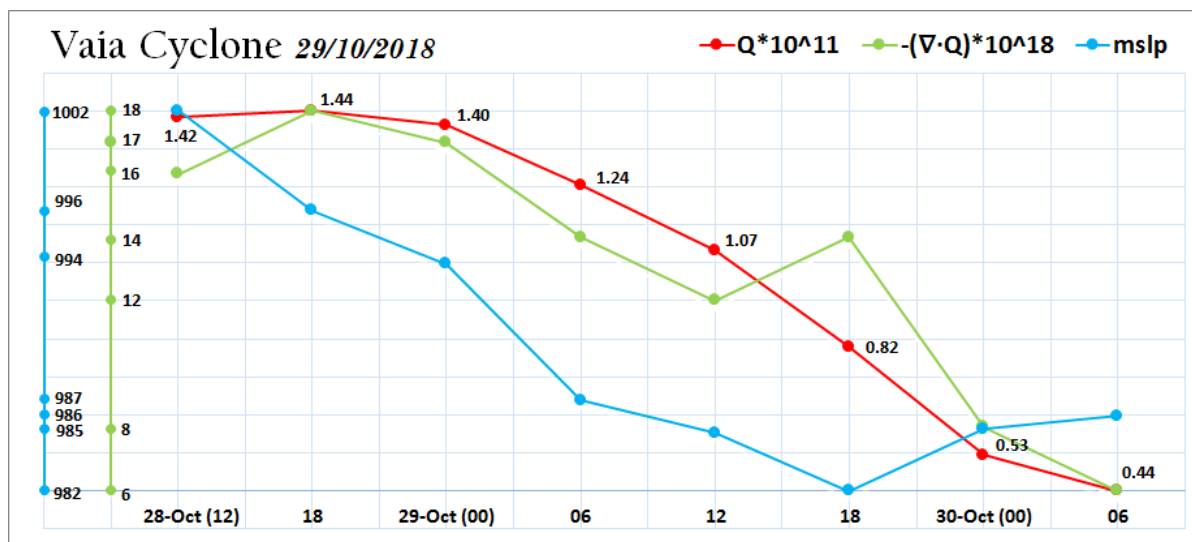b) and d) θ_e at 850 hPa at 00 UTC on 30 October 2018.

Figure 3.6: Temporal evolution, from 12 UTC on 28 October to 6 UTC on 30 October, of the mean sea level pressure (blue line), the maximum convergence of Q-vector (green line) and the Q-vector (red line).

3.2   Other cases

3.2.1   Cyclone Klaus, *23-24 January 2019*

Synoptic analysis

The synoptic scenario on 22 January was characterized by a wide anticyclonic area over the Atlantic Ocean, with a strong pressure gradient along its eastern border, responsible for intense North-Westerly flows over Southern France, and a vast low pressure system over the European area. On 23 January, over the Alps between France and Italy, a cyclone appeared which presented explosive development, due to the presence of the *jet stream* at high altitude (Figure 3.7). Italy, in the days of 22, 23 and 24 January 2019, was affected by a sudden drop in temperatures down to values around zero and by snowfall (Figure 3.8 shows analysis map referring to January 24) [10].
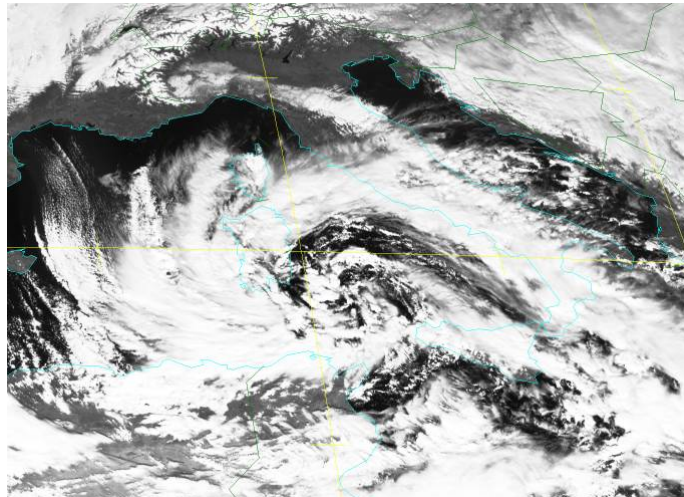
Figure 3.7: Image acquired by the Meteosat Spinning Enhanced Visible satellite (wavelength 0.4 *μm*) at 12 UTC on 24 January 2019 (SEVIRI). The image highlights the presence of a cyclonic circulation over the Western Mediterranean Sea (Cyclone Klaus).
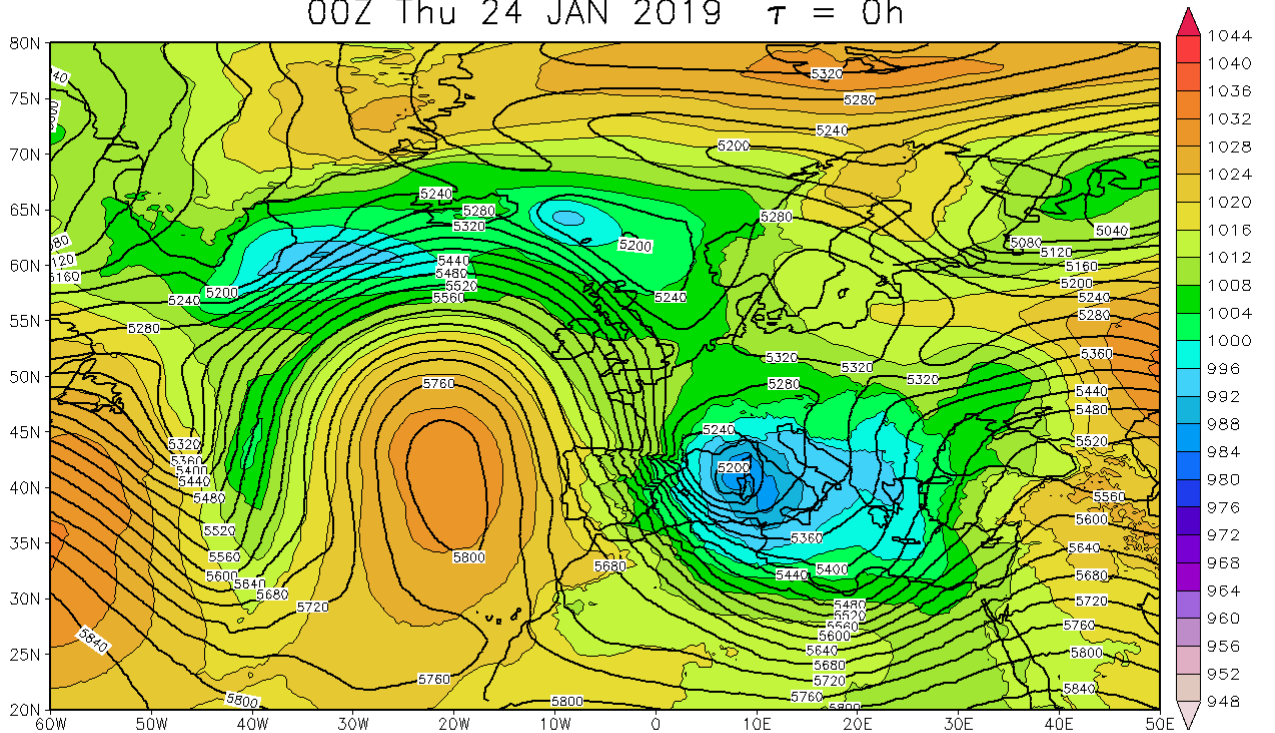
Figure 3.8: Analysis map of geopotential height at 500 hPa (contour) and of mean sea level pressure (shaded) at 00 UTC of 24 January 2019 of the global European reference ECSYN-*European Center SYNoptic model* model corresponding to the IFS model (model of the ECMWF with a resolution of about 10 km).

Study of the evolution of the Q-vector following the trajectory of the cyclone

To study the temporal evolution of the cyclone Klaus, a domain was chosen between the latitudes $20°N - 65°N$ and longitudes $-15°W - 40°E$.

Cyclone Klaus, like Vaia and Anton, underwent an explosive-type development. However unlike the latter, it has become an occluded system as soon as it entered the Mediterranean Sea. The Q-vector well represents a weak frontogenesis in the Mediterranean area, highlighting values that do not reach the order of magnitude of 10^{-11} $\frac{m^2}{kgs}$. As for the divergence of the Q-vector, the maximum value is $-13 * 10^{-18}$ $\frac{m}{kgs}$ reached at 12 UTC on 24 January (Figura 3.10 c)).

In Figure 3.12, it is observed that the maximum pressure deepening occurs at 06 UTC on 24 January and the maximum convergence of the Q-vector occurred 6 hours later.

As for the θ_e (observing panels b) and d) from Figure 3.9 to 3.11) there is no intense advection of cold air and a few hours after its entry on the Mediterranean Sea, cyclone Klaus is in an occlusion phase (Figure 3.10 b)). The intensification of the low can be presumably attributed to the jet associated with the sack.

The time evolution maps of the most significant moments are shown below.

(a)

(b)

(c)

(d)

Figure 3.9: a) e c) Map of mslp (black contour), Θ (850 hPa) (magenta contour), Q-vector (black arrows, with units of $2 * 10^{-11} \frac{m^2}{kgs}$) and Q-vector divergence (shaded) referring to 06 and 18 UTC respectively on 23 January 2019. The figure shows the numerical values assumed following the trajectory of the cyclone, the pressure low (mslp) (whose position is indicated by the blue dot), the maximum Q-vector present in the domain and the maximum convergence of the Q-vector multiplied by 10^{18} (position indicated by the blue triangle).

b) and d) θ_e at 850 hPa referring to 06 and 18 UTC respectively on 23 January 2019.

Figure 3.10: a) e c) Map of mslp (black contour), Θ (850 hPa) (magenta contour), Q-vector (black arrows, with units of $2*10^{-11}$ $\frac{m^2}{kgs}$) and Q-vector divergence (shaded) referring to 06 and 12 UTC respectively on 24 January 2019. The figure shows the numerical values assumed following the trajectory of the cyclone, the low (mslp) (whose position is indicated by the blue dot), the maximum Q-vector present in the domain and the maximum convergence of the Q-vector multiplied by 10^{18} (position indicated by the blue triangle).
b) and d) θ_e at 850 hPa referring to 06 and 12 UTC respectively on 24 January 2019.

(a)　　　　　　　　　　　　　　　　　(b)
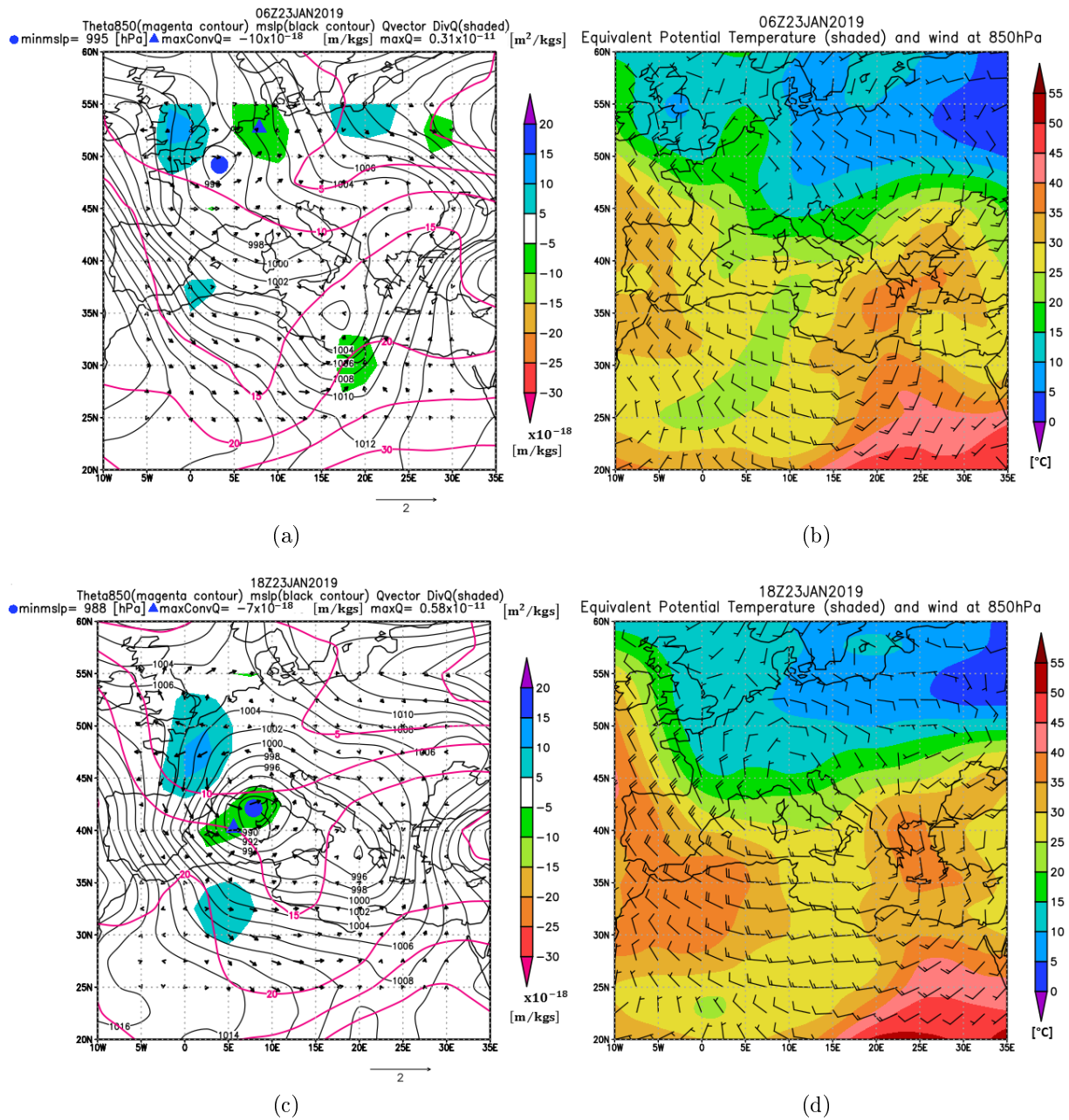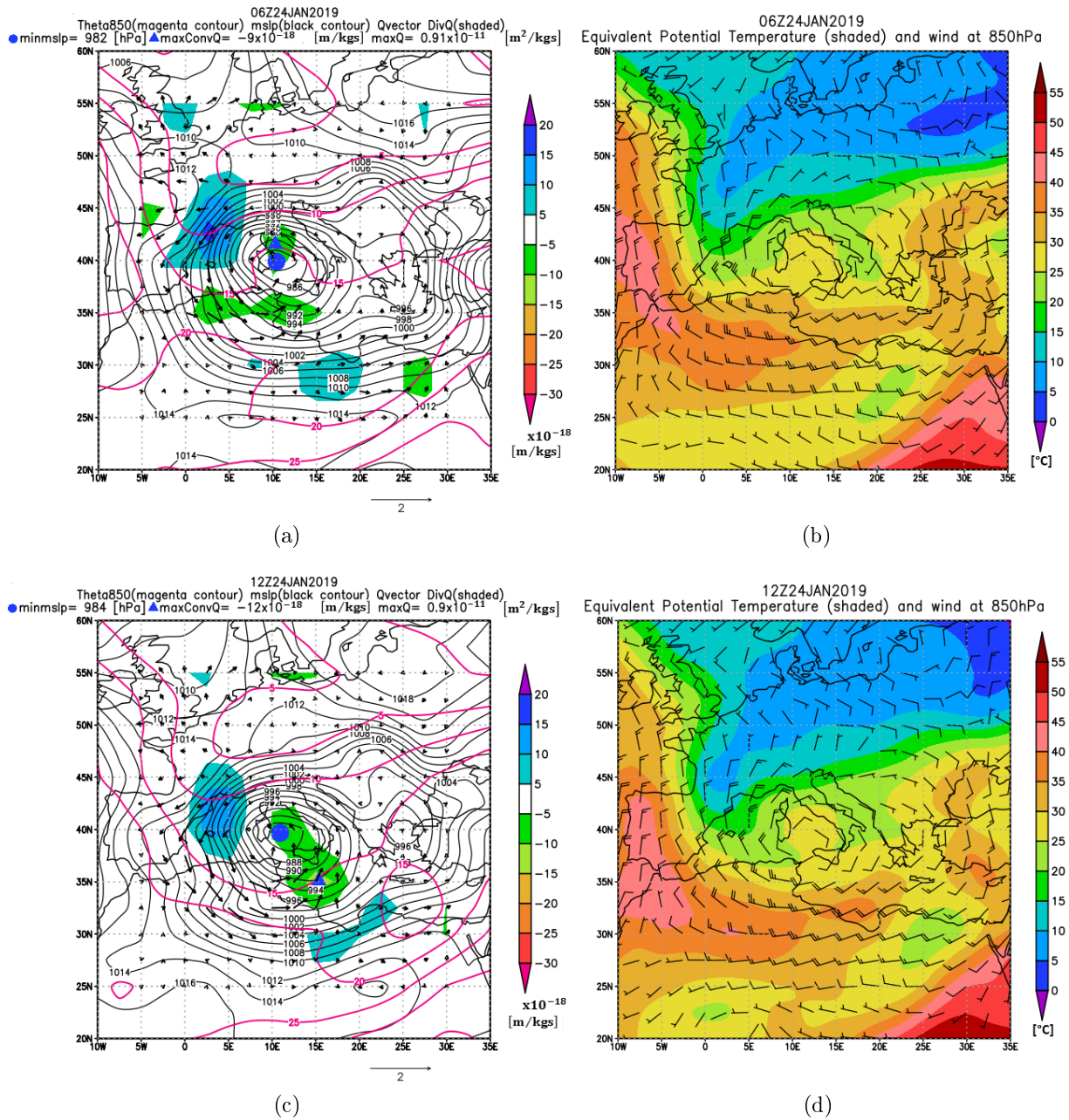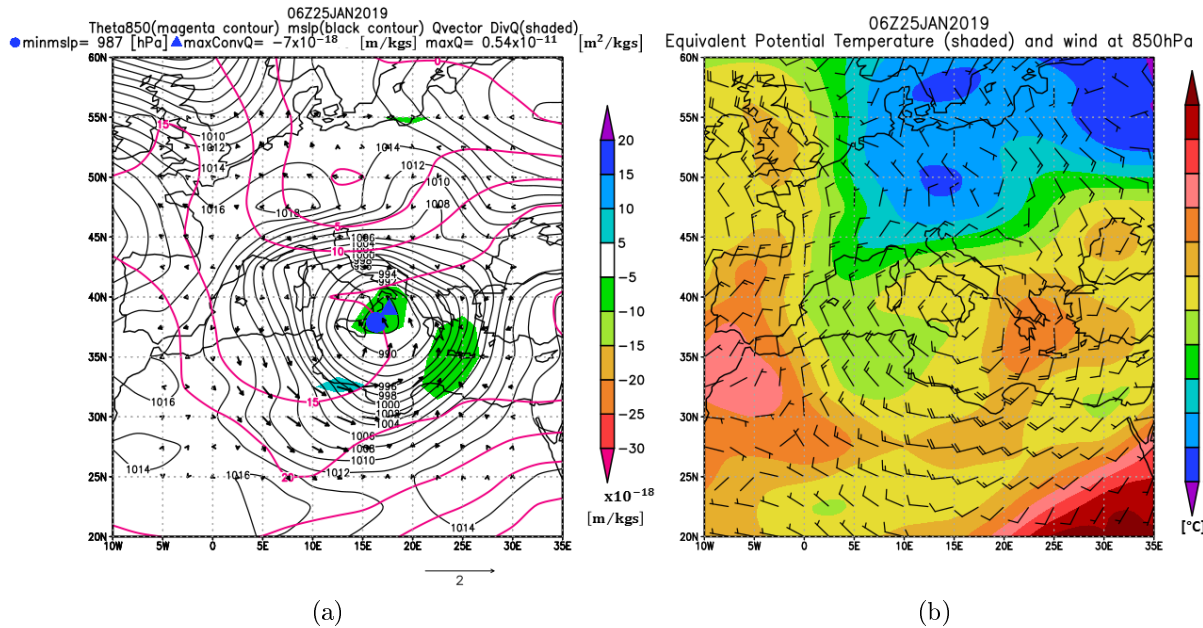
Figure 3.11: a) Map of mslp (black contour), Θ (850 hPa) (magenta contour), Q-vector (black arrows, with units of $2*10^{-11}\ \frac{m^2}{kgs}$) and Q-vector divergence (shaded) at 06 UTC on 25 January 2019. The figure shows the numerical values assumed following the trajectory of the cyclone, the pressure low (mslp) (whose position is indicated by the blue dot), the maximum Q-vector present in the domain and the maximum convergence of the Q-vector multiplied by 10^{18} (position indicated by the blue triangle).
b) and d) θ_e at 850 hPa at 06 UTC on 25 January 2019.

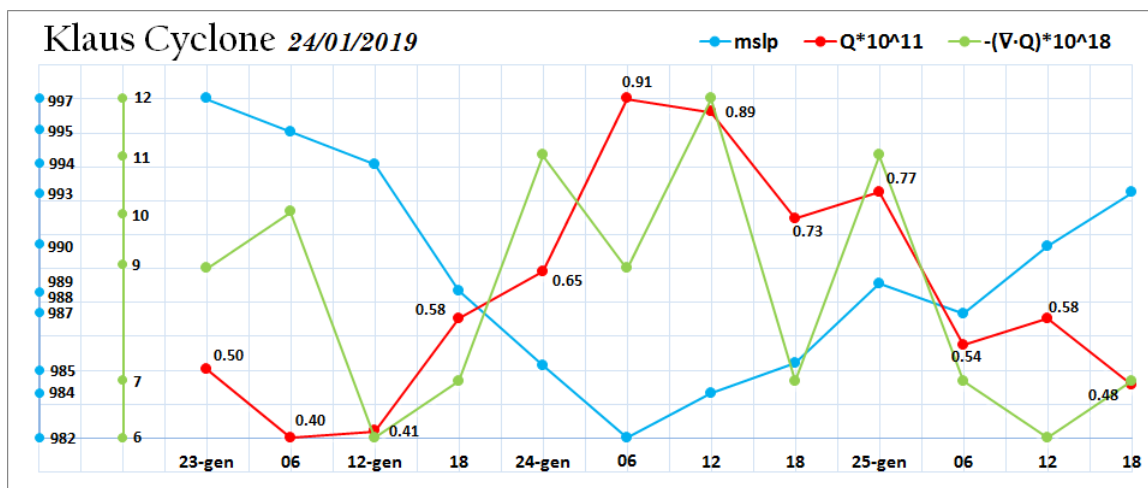Figure 3.12: Temporal evolution, from 00 UTC on 23 January to 18 UTC on 25 January, of the mean sea level pressure (blue line), of the maximum convergence of Q-vector (green line) and of the Q-vector (red line).

44

3.2.2   Cyclone Qendresa, *6-7 November 2014*

Synoptic analysis

In the first week of November 2014 a large part of the Italian peninsula was affected by the effects, mostly associated with intense rainfall, of a large depression area present on the Western Mediterranean (see Figure 3.14 a)).

On 6 November 2014 a weak expansion of an anticyclone over the Atlantic favored the descent of North-Atlantic cold air over Europe. The trough has deepened reaching North Africa, being hindered in its Eastward motion by an anticyclonic area present on Russia. The interaction of the trough with the Atlas chain on 6 November gave rise to the formation of a low. This low moved northward when, in the early hours of 7 November (Figure 3.14 b)), on South of Sicily it evolved into a TLC structure (*Tropical Like Cyclone*) [17].

A TLC is characterized [20] by:

- Warm core (Figure 3.13 a))

- Vorticity maximum at 850 hPa (Figure 3.13 b))

- Limited extension on a spatial scale (a few hundred km) (Figure 3.14 a))

- Presence of a cloudless eye (Figure 3.14 a))

- Marked convective activity (Figure 3.14 a))

Cyclone Qendresa has these characteristics, shown in the following figures:

(a)

(b)
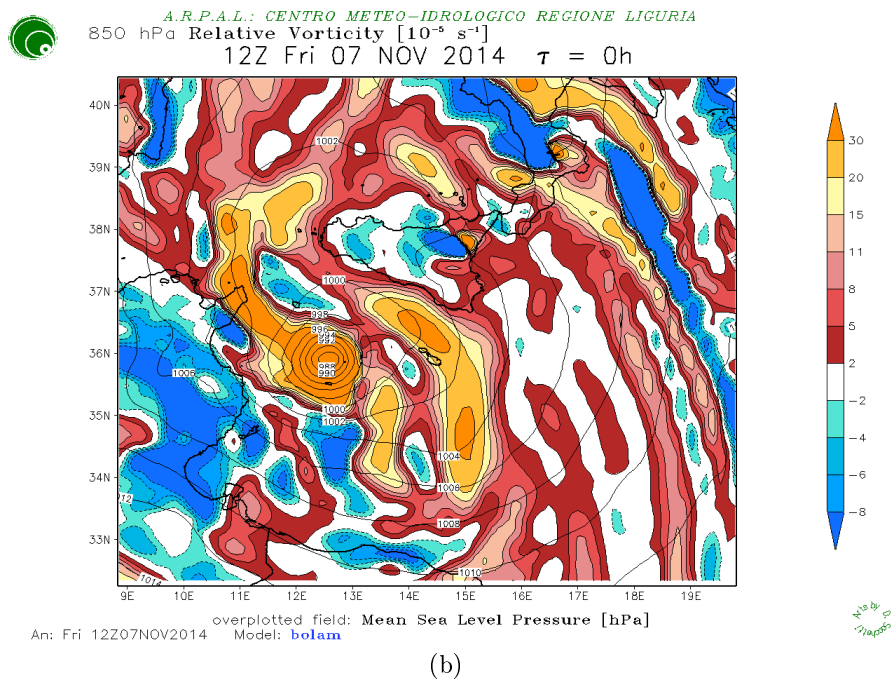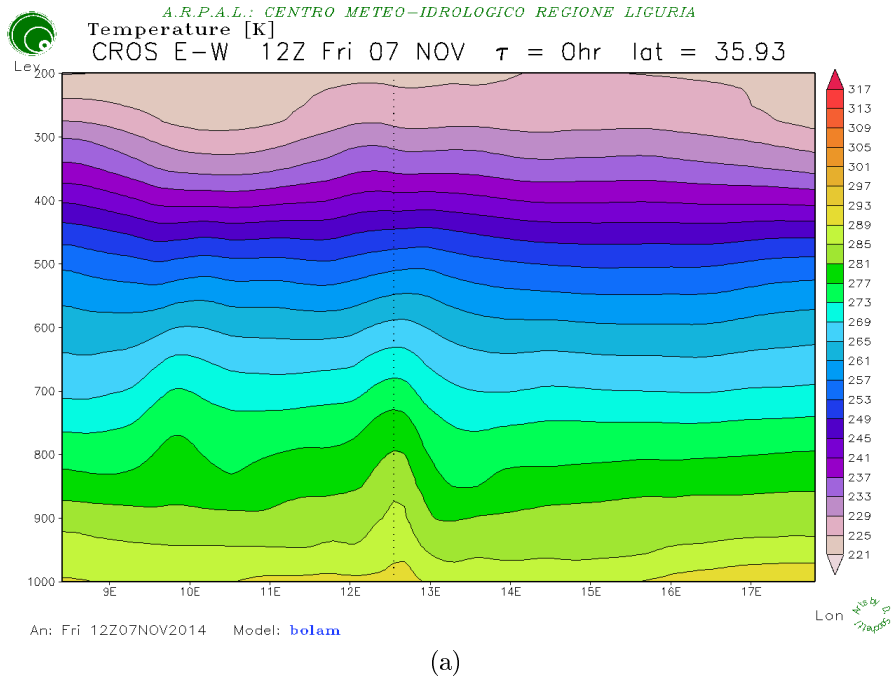
Figure 3.13:
a) Vertical Cross Section of Temperature in K (analysis map, at 12 UTC of 7 November 2014, of the BOLAM high resolution hydrostatic model).
b) Vorticity at 850 hPa at 12 UTC on 7 November 2014 (analysis map of the BOLAM high resolution hydrostatic model).
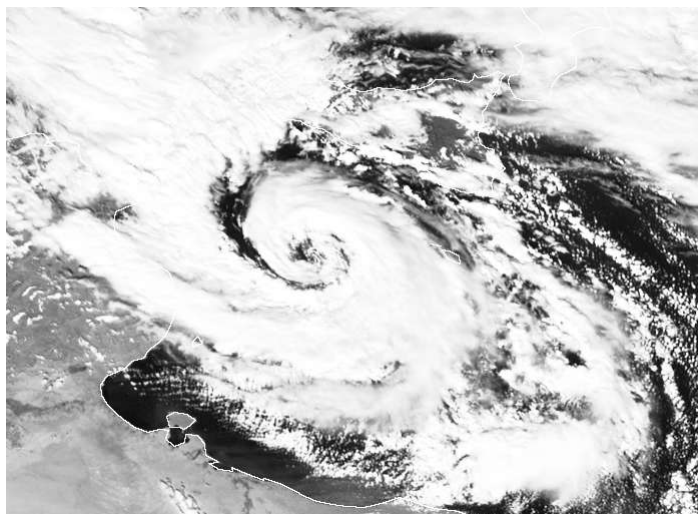
(a)
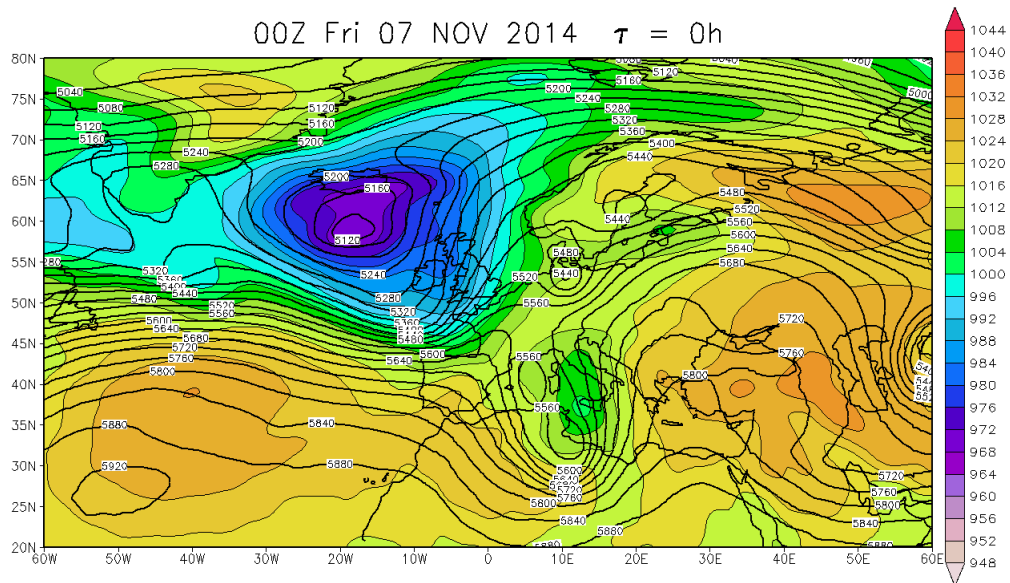
(b)

Figure 3.14:
a) Image acquired by the Meteosat Spinning Enhanced Visible satellite (wavelength 0.4 *mum*) at
12 UTC on November 7, 2014 (SEVIRI). The image highlights the presence of a cyclonic circulation
between Tunisia and Sicily (Cyclone Qendresa).
b) Map of analysis of the geopotential height at 500 hPa (contour) and of mean sea level pressure
(shaded) at 00 UTC on 7 November 2014 of the GFS model initialized at 00 UTC on 7 November
2014.

Study of the evolution of the Q-vector following the trajectory of the cyclone

To study the temporal evolution of the cyclone Qendresa, a domain was chosen between the latitudes $15°N - 50°N$ and the longitudes $-15°W - 35°E$.
Analyzing the evolution of the Q-vector (from Figure 3.15 to 3.17) it is observed, in this case that:

- The Q-vector takes on an order of magnitude of 10^{-11} $\frac{m^2}{kgs}$ in an instant during the extra-tropical phase (Figure 3.15 c)). Subsequently, with the change of dynamics in TLC, it assumes values of the order of magnitude of 10^{-12} $\frac{m^2}{kgs}$ (Figura 3.16 a)). This can be explained by the fact that in the TLC phase there is no longer the frontogenetic dynamics typical of extra-tropical cyclones but the dynamics dominated by heat exchanges typical of tropical type cyclones.

- The Q-vector associated with the cyclone Qendresa, compared with Vaia, assumes an order of magnitude of 10^{-11} $\frac{m^2}{kgs}$ during the phase of maximum baric intensification (Figure 3.15 c)).

- For ascending motions, the divergence of Q-vector assumes values less than or equal to $-14 * 10^{-18}$ $\frac{m}{kgs}$, that is, not particularly intense.

- The decrease in the Q-vector, from 7 November (Figure 3.16 a)), is consistent with the decrease in horizontal temperature gradients during the occlusion phase.

  From the graph in Figure 3.18 it is observed that:

- The absolute maximum convergence of the Q-vector, associated with upward vertical motions, occurs 24 hours before the maximum cyclonic deepening.

The time evolution maps of the most significant moments are shown below. Looking at cases b) and d) from Figure 3.15 to Figure 3.17 a front is not identified because the baroclinic structure quickly transforms into barotropic and in fact the Q-vector does not assume high values (that is, it does not reach the order of magnitude 10^{-11} $\frac{m^2}{kgs}$).

(a)   (b)

(c)   (d)

Figure 3.15: a) e c) Map of mslp (black contour), Θ(850 hPa) (magenta contour), Q-vector (black arrows, with units of $2 * 10^{-11} \frac{m^2}{kgs}$) and Q-vector divergence (shaded) referring respectively to 00 and 12 UTC on 6 November 2014. The title of the Figure shows the numerical values assumed following the trajectory of the cyclone, the pressure low (mslp) (whose position is indicated by the blue dot), the maximum Q-vector present in the domain and the maximum convergence of the Q-vector multiplied by 10^{18} (location indicated by the blue triangle).
b) e d) θ_e at 850 hPa referring to 00 and 12 UTC respectively on 6 November 2014.

49

(a)

(b)

(c)

(d)
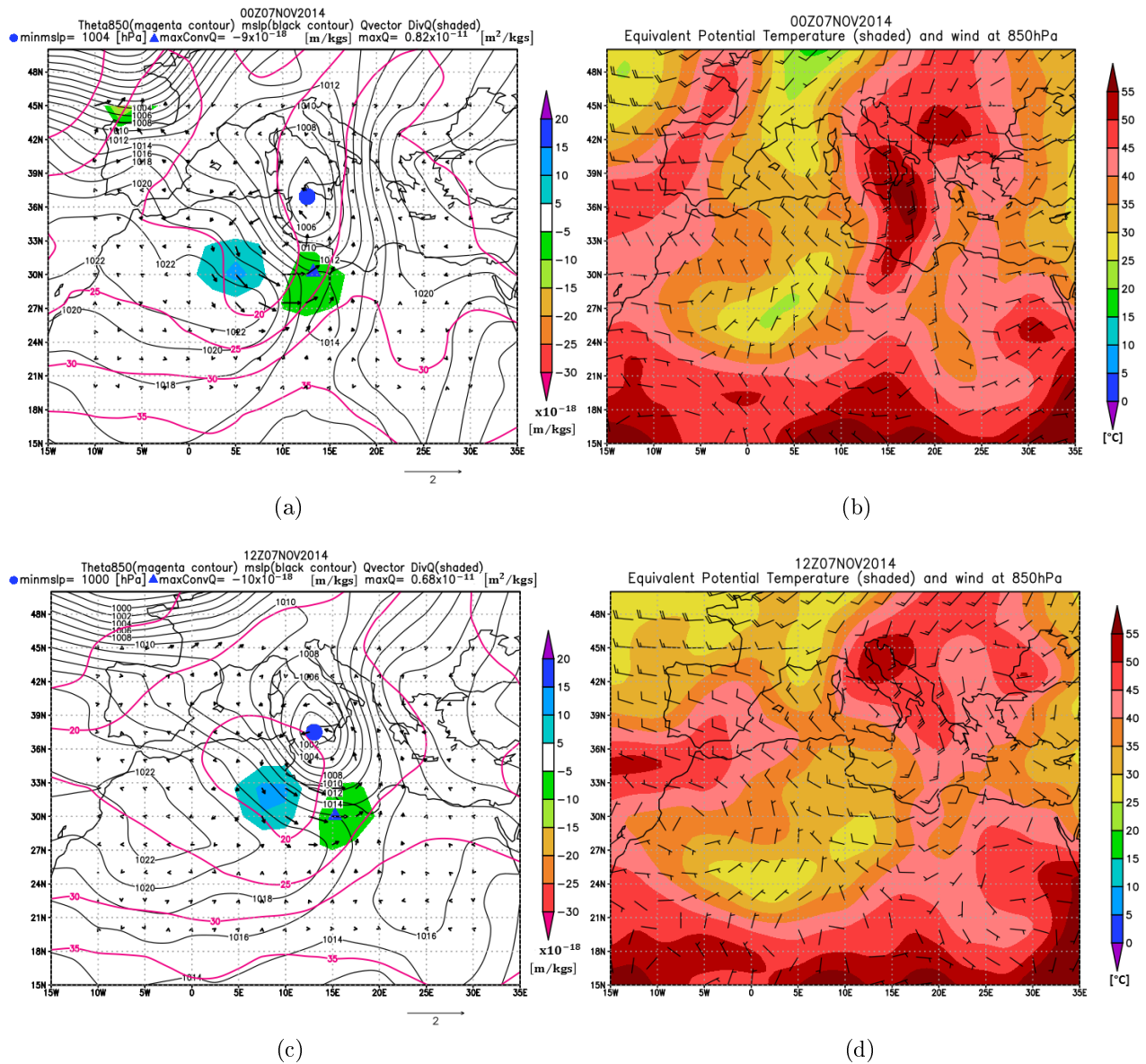
Figure 3.16: a) e c) Map of mslp (black contour), $\Theta(850\text{ hPa})$ (magenta contour), Q-vector (black arrows, with units of $2 * 10^{-11} \frac{m^2}{kgs}$) and Q-vector divergence (shaded) referring to 00 and 12 UTC respectively on 7 November 2014.c

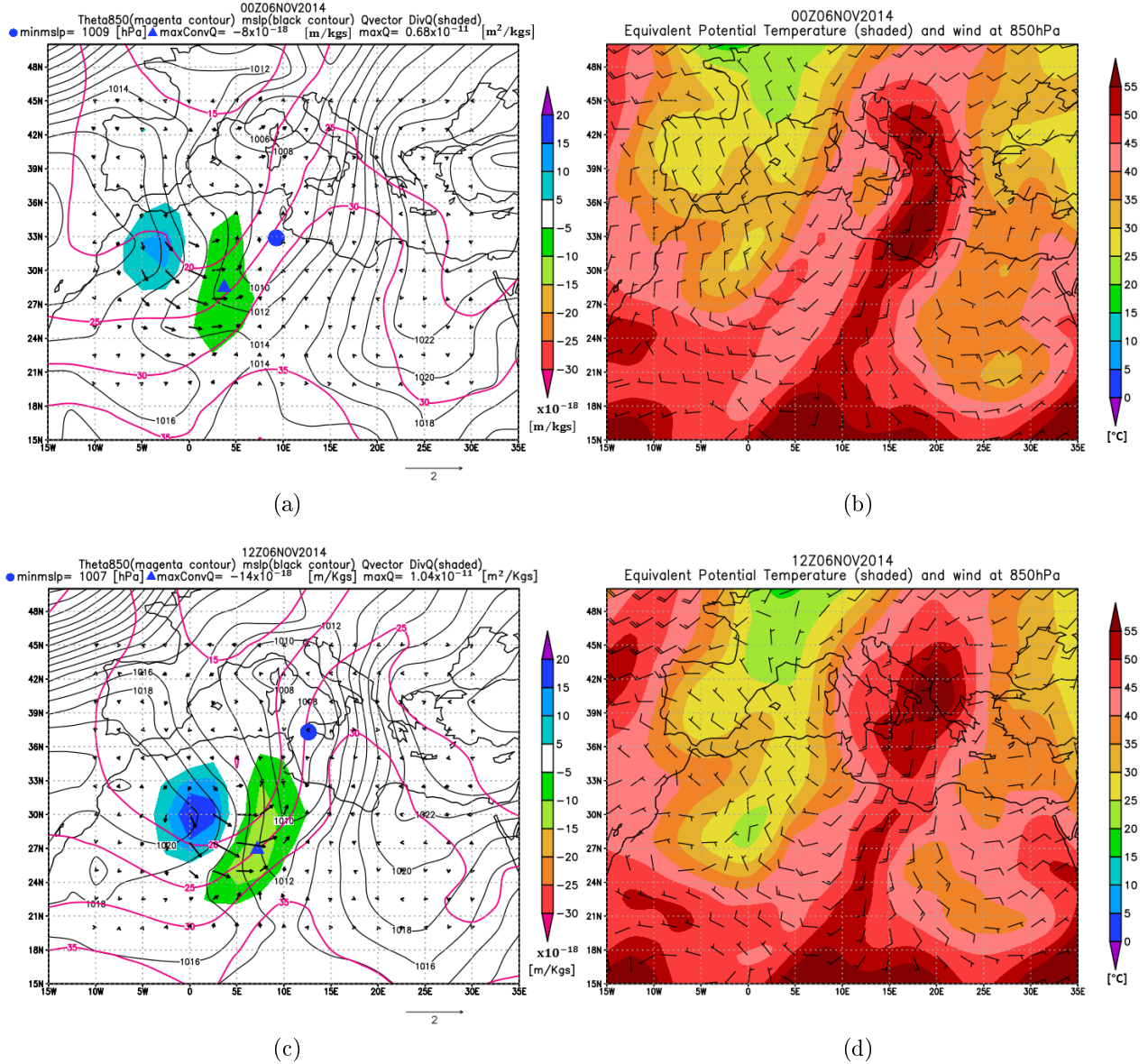b) e d) θ_e at 850 hPa referring to 00 and 12 UTC respectively on 7 November 2014.
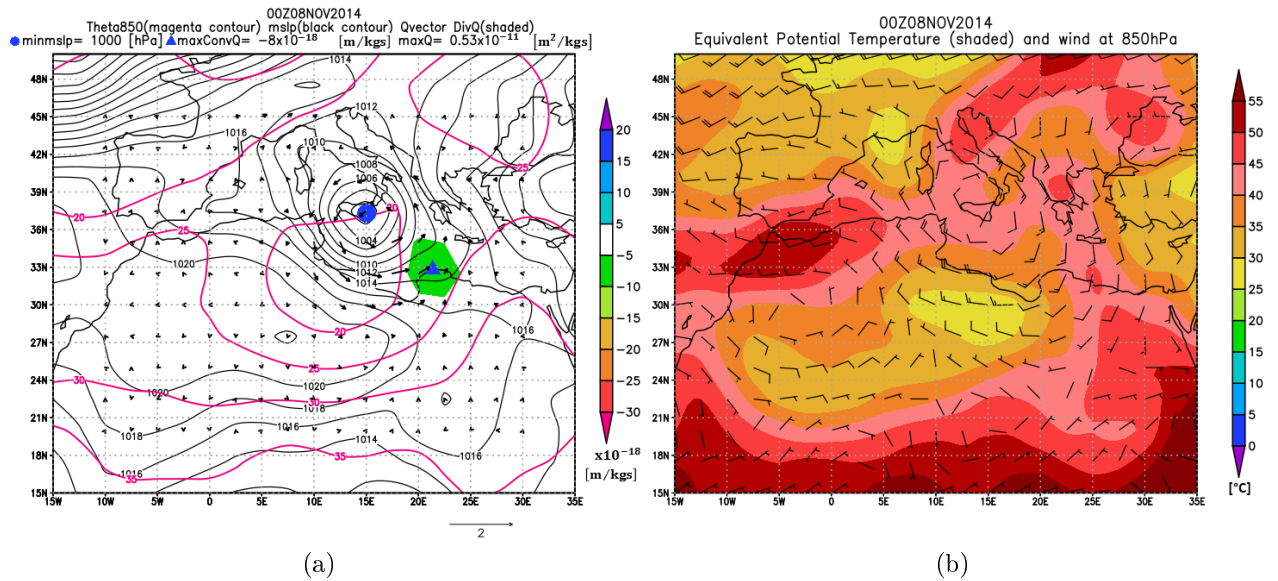
Figure 3.17: a) Map of mslp (black contour), Θ(850 hPa) (magenta contour), Q-vector (black arrows, with units of $2 * 10^{-11} \frac{m^2}{kgs}$) and Q-vector divergence (shaded) at 00 UTC on 8 November 2014. The title of the Figure shows the numerical values assumed following the trajectory of the cyclone, the minimum pressure (mslp) (whose position is indicated by the blue dot), the maximum Q-vector present in the domain and the maximum convergence of the Q-vector multiplied by 10^{18} (location indicated by the blue triangle).

b) θ_e at 850 hPa at 00 UTC of 8 November 2014.
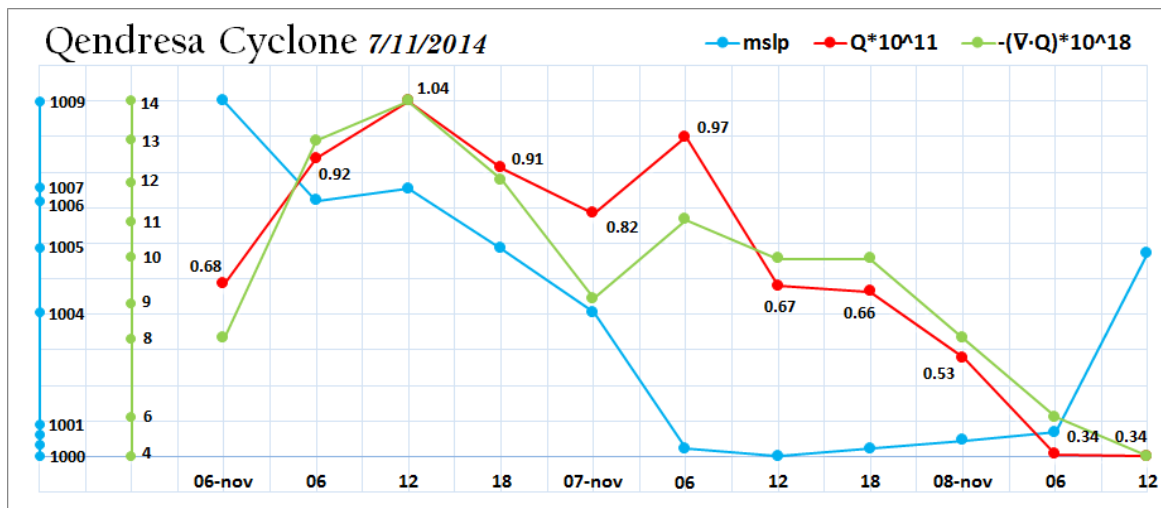
Figure 3.18: Temporal evolution, from 00 UTC on 6 November to 12 UTC on 8 November, and of mean sea level pressure (blue line), the maximum convergence of Q-vector (green line) and the Q-vector (red line).

3.2.3 Cyclone Anton, *5 March 2015*

Synoptic analysis

Between 4 and 5 March Tuscany was affected by an event characterized by stormy winds ($62-102$ km/h according to the Beaufort scale classification) with intense gusts ($103-117$ km/h according to the classification of the Beaufort scale) which caused a lot of damage including: demolished trees, uncovered roofs, torn billboards and problems with road and rail traffic. The synoptic situation, starting from 3 March, was characterized by the presence of a large area of high pressure from the Atlantic to the Balkans which, during the 4 March, moved towards higher latitudes close to Iceland. This configuration favored the descent, on the Mediterranean, of cold air in the middle-lower troposphere along the descending branch of high pressure, associated with the formation of a pressure minimum South of the Alps (Figure 3.19 a)). The latter quickly reached the value of 997 hPa on the middle of the Tyrrhenian Sea (Figure 3.19 b)) where it stayed for many hours. Meanwhile, between 4 and 5 March morning, the Atlantic ridge strengthened to reach ground values in the Bay of Biscay of 1043 hPa. As a result, a pressure gradient of over 40 hPa has developed between northern France and the Tyrrhenian Sea. On 5 March winds reached the remarkable intensity of over 150 km/h on the Tuscan-Emilian and Ligurian Apennines, probably due to the combination of different factors [2]:

1. Strong pressure gradient

2. Katabatic effect; formed because the cold air, coming from the north-east, is forced to cross the Apennines pouring into the leeward areas (Tuscany) where milder lighter air was present. The air mass has therefore undergone a significant acceleration in its downward motion.

3. Explosive cyclogenesis with the consequent ignition of the isallobaric wind[5]

---

[5]Wind that tends to blow from regions where there are sudden baric rises to adjacent regions where the exact opposite occurs.
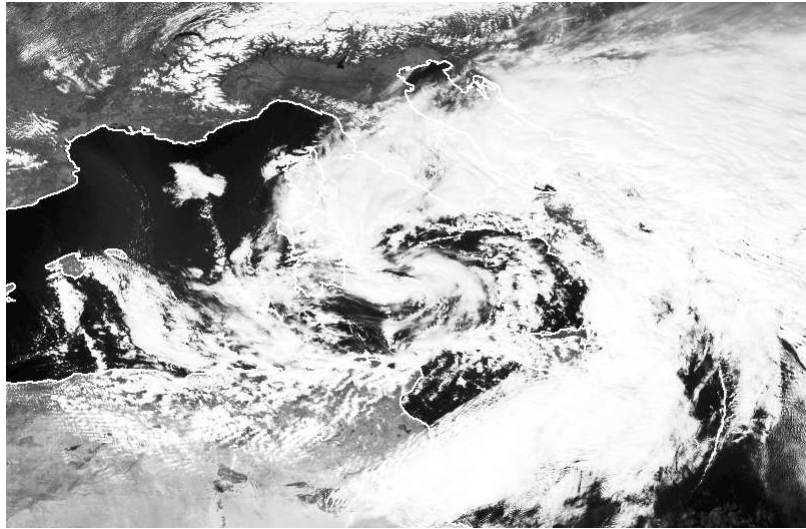
(a)
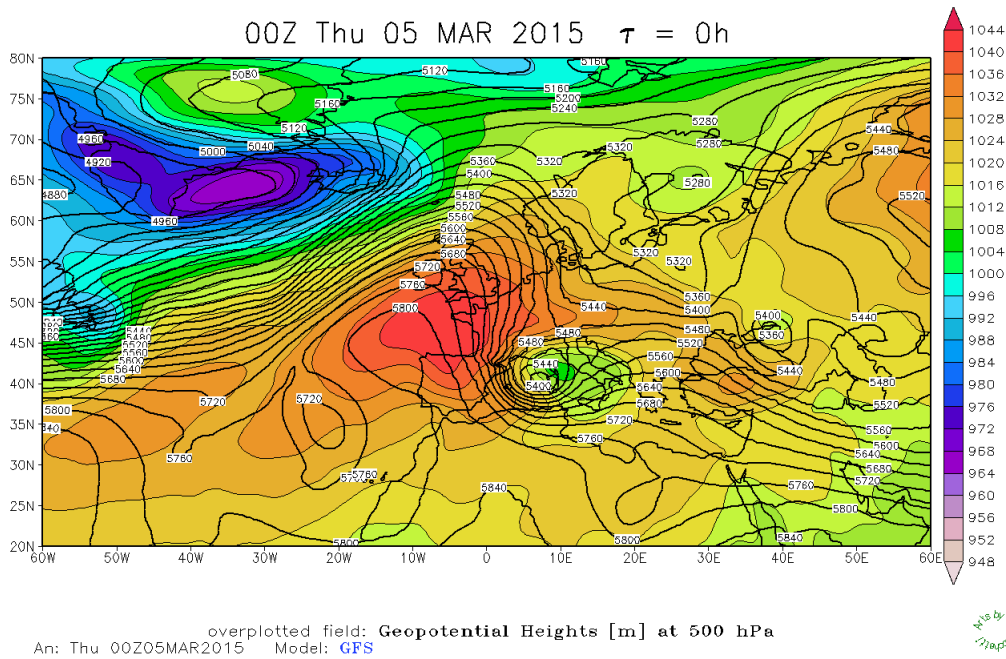
(b)

Figure 3.19:
a) Image acquired by the Meteosat Spinning Enhanced Visible satellite (wavelength 0.4 μm) at 12 UTC on 5 March 2015 (SEVIRI). The image highlights the presence of a cyclonic circulation on the Tyrrhenian Sea (Cyclone Anton).
b) Map of analysis of the geopotential height at 500 hPa (contour) and of pressure at medium sea level (shaded) at 00 UTC on 5 March 2015 of the GFS model initialized at 00 UTC on 5 March 2015.

Study of the evolution of the Q-vector following the trajectory of the cyclone

To study the temporal evolution of the cyclone Anton, a domain was chosen between the latitudes $25°N - 55°N$ and the longitudes $-15°W - 30°E$.

As can be seen from panels a) and d) from Figure 3.20 to Figure 3.22, the cyclone Anton shows a Q-vector of the order of magnitude of 10^{-11} $\frac{m^2}{kgs}$ for 18 consecutive hours, about 12 hours after its formation. The maximum value of Q-vector ($1.47 * 10^{-11}$ $\frac{m^2}{kgs}$ reached at 06 UTC on 5 March; Figure 3.21 c)), is comparable to the maximum value reached by the Vaia case ($1.44 * 10^{-11}$ $\frac{m^2}{kgs}$).

However, it is important to note some differences:

- The two events occurred in two different seasons (Vaia in autumn and Anton in winter) and therefore heat exchanges of different magnitude occurred.

- The Q-vector, in Vaia, assumes the order of magnitude of 10^{-11} $\frac{m^2}{kgs}$ 6 hours before the formation of the low (thus indicating a tendency to frontogenesis independent of cyclone development), while in Anton, it reaches that order of magnitude 24 hours after formation.

- The maximum negative divergence (i.e. convergence) of the Q-vector associated with the ascending motions, in Vaia, assumed in a single instant, is $-18 * 10^{-18}$ $\frac{m}{kgs}$ (Figure 3.2 c)), while in Anton, the value reaches $-29 * 10^{-18}$ $\frac{m}{kgs}$ from the 18 UTC of the 4 March (Figure 3.20 c)) at 06 UTC on 5 March (Figure 3.21 c)). This intensity may have been influenced, at least in part, by the contribution of vertical motions due to the presence of the orography.

- Compared to the cyclone Vaia, in which the maximum Q-vector occurs simultaneously with the maximum negative divergence of the Q-vector, associated with the ascending motions (Figure 3.24 a)), in Anton, the maximum negative divergence already occurs 12 hours before reaching the maximum value of Q-vector (Figure 3.24 b) and Figure 3.21 c)).

Further considerations have been made by analyzing the graph in Figure 3.23.
In particular, it is observed that:

- The maximum baric deepening occurred at 18 UTC on 5 March is preceded by the maximum convergence of the Q-vector associated with the ascending vertical motions (Q-vector divergence value of $-29 * 10^{-18}$ $\frac{m}{kgs}$ isible in Figure 3.20 c)).

As for the θ_e, from Figure 3.20 to 3.22, panels c) and d), there is no intense advection of cold air and the intensification of the minimum is attributable to other dynamic factors (see the first two points reported in the list in the synoptic analysis section).

(a)

(b)

(c)

(d)

Figure 3.20: a) e c) Map of mslp (black contour), Θ (850 hPa) (magenta contour), Q-vector (black arrows, with units of $2 * 10^{-11} \frac{m^2}{kgs}$) and Q-vector divergence (shaded) referring to 06 and 18 UTC respectively on 4 March 2015. The figure shows the numerical values assumed following the trajectory of the cyclone, the pressure low (mslp) (whose position is indicated by the blue dot), the maximum Q-vector present in the domain and the maximum convergence of the Q-vector multiplied by 10^{18} (position indicated by the blue triangle).

b) and d) θ_e at 850 hPa referring to 06 and 18 UTC respectively on 4 March 2015.

(a)

(b)

(c)

(d)

Figure 3.21: a) e c) Map of mslp (black contour), Θ (850 hPa) (magenta contour), Q-vector (black arrows, with units of $2 * 10^{-11} \frac{m^2}{kgs}$) and Q-vector divergence (shaded) referring to 00 and 06 UTC respectively on 5 March 2015. The figure shows the numerical values assumed following the trajectory of the cyclone, the pressure low (mslp) (whose position is indicated by the blue dot), the maximum Q-vector present in the domain and the maximum convergence of the Q-vector multiplied by 10^{18} (position indicated by the blue triangle).

b) and d) θ_e at 850 hPa referring to 00 and 06 UTC respectively on 5 March 2015.

(a)

(b)

(c)

(d)

Figure 3.22: a) e c) Map of mslp (black contour), Θ (850 hPa) (magenta contour), Q-vector (black arrows, with units of $2*10^{-11} \frac{m^2}{kgs}$) and Q-vector divergence (shaded) referring to 18 UTC on March 5 and 00 UTC on March 6, 2015 respectively. The figure shows the numerical values assumed following the trajectory of the cyclone, the pressure low (mslp) (whose position is indicated by the blue dot), the maximum Q-vector present in the domain and the maximum convergence of the Q-vector multiplied by 10^{18} (position indicated by the blue triangle).

b) e d) θ_e at 850 hPa referring to 18 UTC on 5 March and 00 UTC on 6 March 2015 respectively.
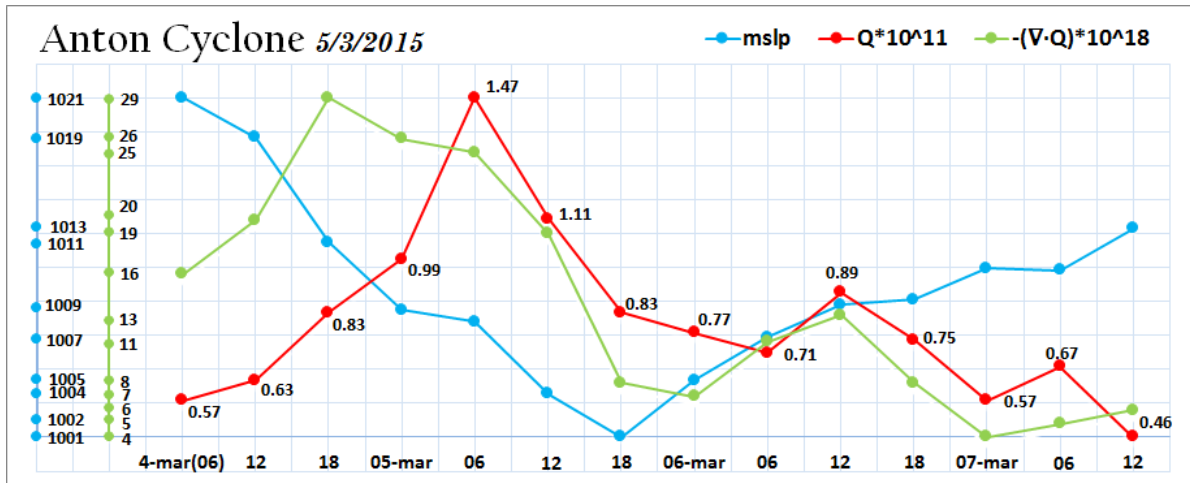
Figure 3.23: Temporal evolution, from 06 UTC on March 4 to 12 UTC on March 7, of the mean sea level pressure (blue line), the maximum convergence of Q-vector (green line) and the Q-vector (red line).
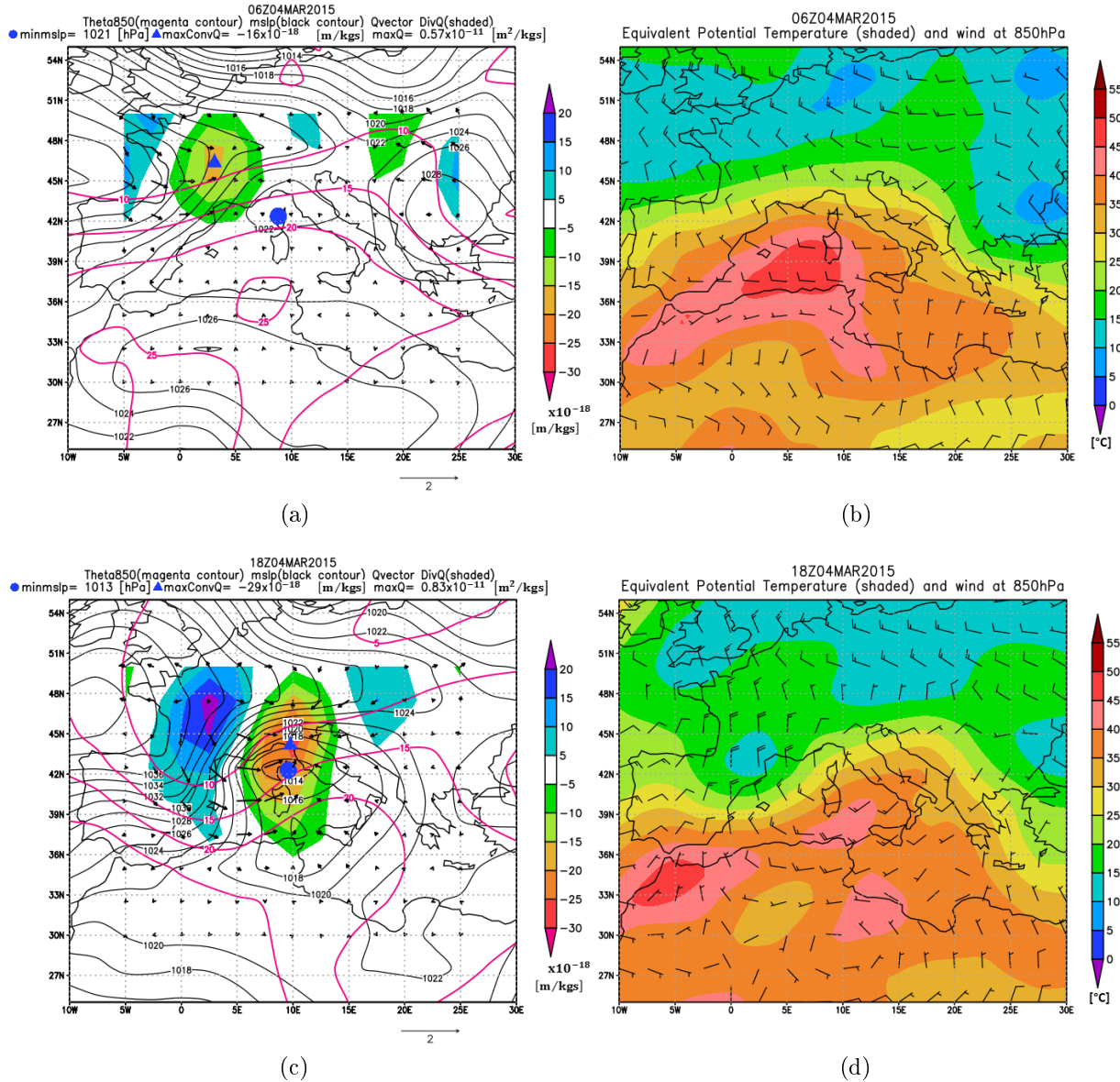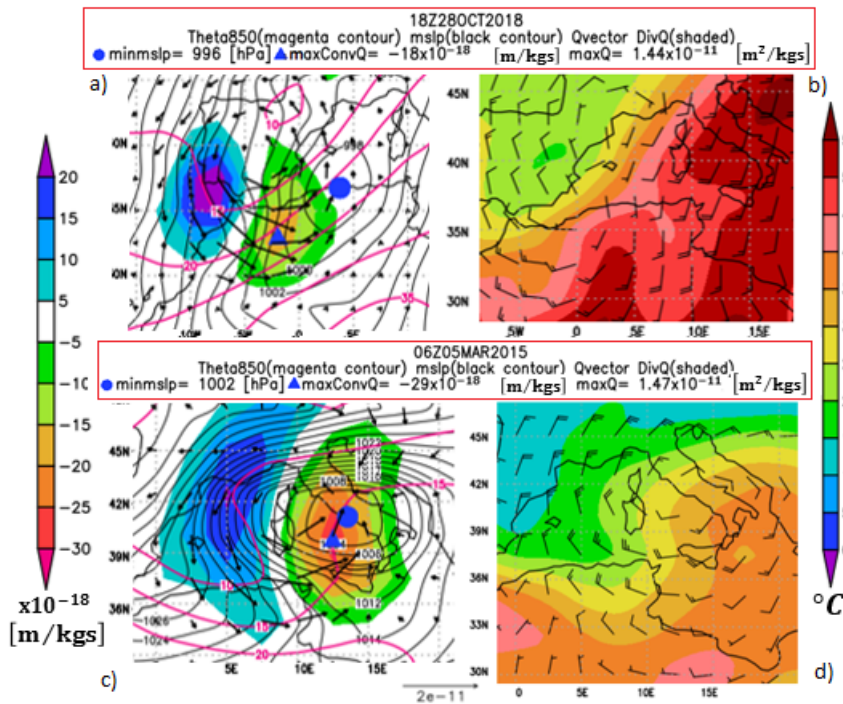

Figure 3.24: a) Map of mslp (black contour), Θ (850 hPa) (magenta contour), Q-vector (black arrows, with units of $2 * 10^{-11} \frac{m^2}{kgs}$) and divergence of the Q-vector (shaded sx); b) Θ_e (850 hPa) (shaded dx) and wind (knots); at 18 UTC on 28 October 2018.
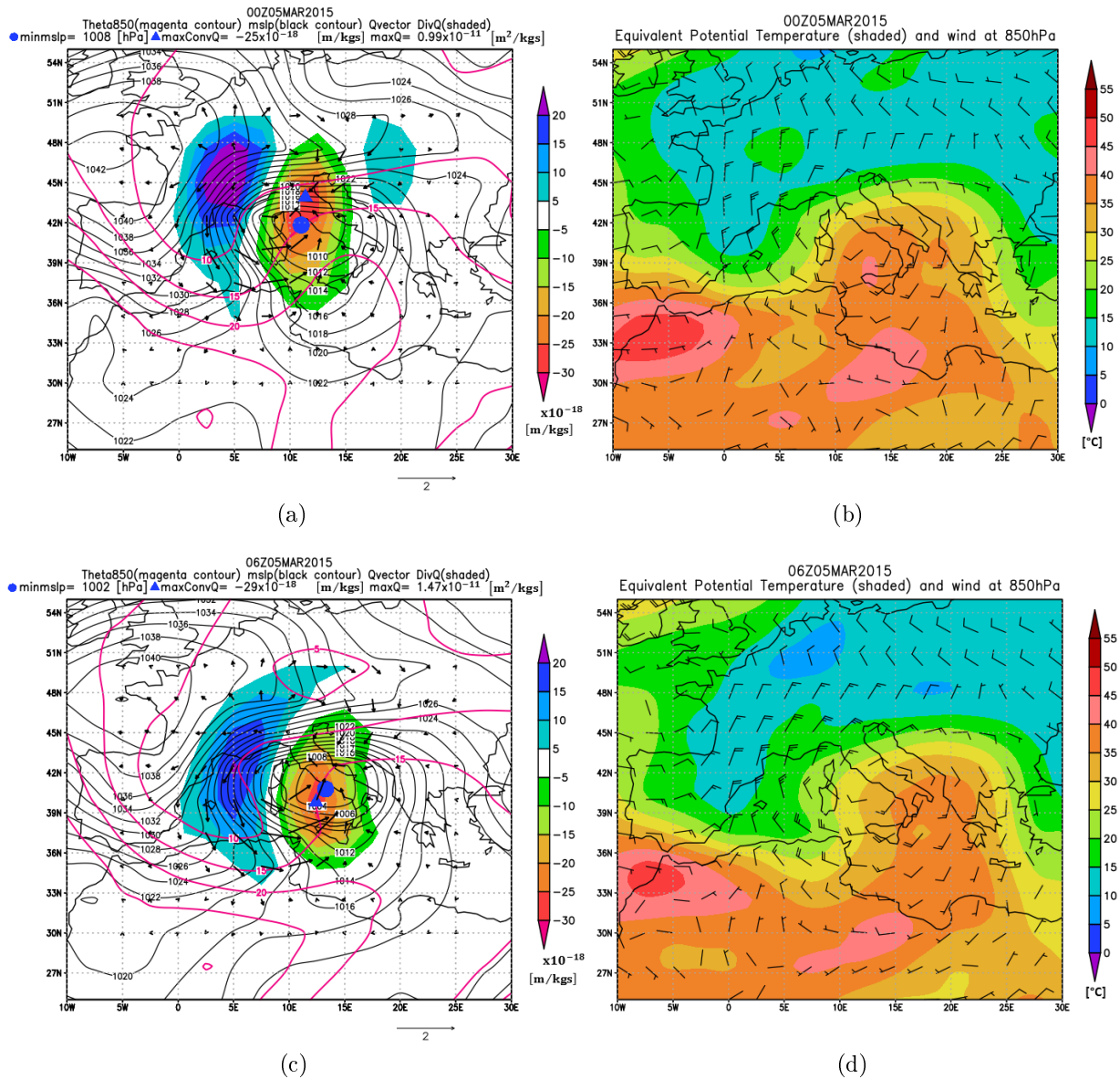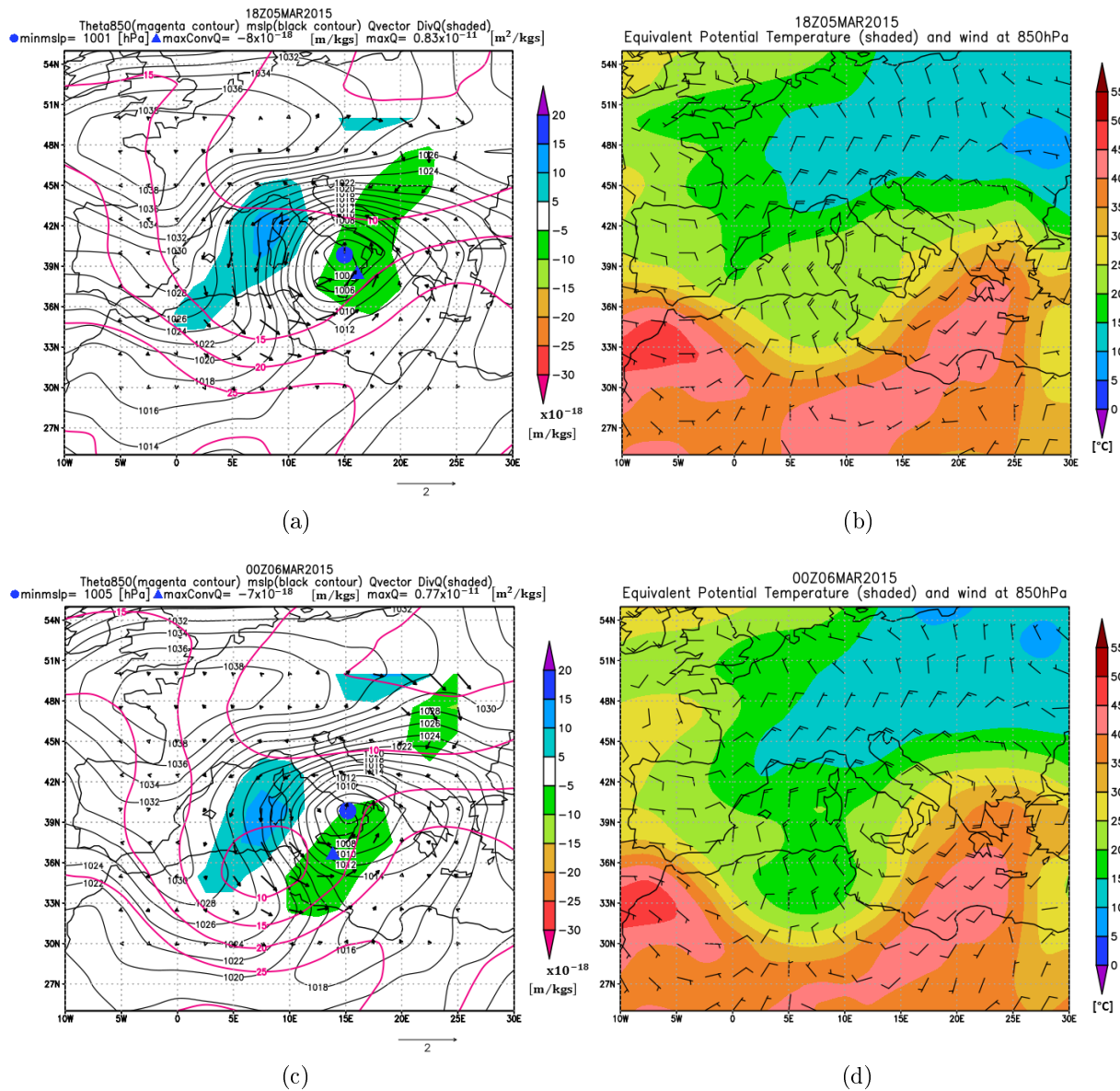c) Map of mslp (black contour), Θ (850 hPa) (magenta contour), Q-vector (black arrows, with units of $2 * 10^{-11} \frac{m^2}{kgs}$) and divergence of the Q-vector (shaded sx); d) Θ_e (850 hPa) (shaded dx) and wind (knots); at 06 UTC 5 March 2015 (b)).

58

Comparison of the frontogenesis function between the cyclone Anton and Vaia

From the Figure 3.24 (panels a) and b)), it is observed that the Q-vector values assumed by the cyclones Anton and Vaia are almost coincident but, observing the equivalent potential temperature at 850 hPa (panels c) and d)), it can be seen that the horizontal thermal gradient of the cyclone Anton, given that it is in an occlusion, is less than that of the cyclone Vaia. Therefore it is reasonable that the high value of Q-vector assumed by Anton, comparable to that of Vaia, is due to the contribution given by the horizontal variation of the geostrophic wind rather than by the horizontal thermal gradient. To confirm this hypothesis, the function Frontogenesis (the formula used is reported in chapter 1) [16] has been graphed together with the most significant images for the comparison between the two cyclones shown in Figure 3.25 and in Table 3.1 with all the values assumed by the frontogenesis function during the temporal evolution of low.

The Q-vector was calculated at an altitude of 500 hPa but for the Frontogenesis function the level of 850 hPa was considered, since this altitude, in the meteorological forecast phase, is used to identify, using the equivalent potential temperature and wind, frontal structures.

Observing Table 3.1, and recalling that the maximum cyclonic deepening of Vaia and Anton occurs respectively at 18 UTC on 29 October 2018 and 5 March 2015, it is observed that the Frontogenesis maxima are assumed 6 hours before the maximum cyclonic deepening. The cyclone Vaia assumes a Frontogenesis value higher than that assumed by the cyclone Anton; respectively $7K/ms$ and $6K/ms$. Therefore, observing the frontogenesis values obtained, we can support the hypothesis that, with the same value of Q-vector, in the cyclone Anton dominates the horizontal gradient of the geostrophic wind rather than the temperature gradient, as instead happens for the cyclone Vaia .

Time (cyclone Vaia)	F (10^{-10} $\frac{K}{ms}$)	Time (cyclone Anton)	F (10^{-10} $\frac{K}{ms}$)
12 UTC 28/10/18	3	12 UTC 4/03/15	2
18 UTC 28/10/18	3	18 UTC 4/03/15	5
00 UTC 29/10/18	5	00 UTC 5/03/15	5
06 UTC 29/10/18	5	06 UTC 5/03/15	5
12 UTC 29/10/18	7	12 UTC 5/03/15	6
18 UTC 29/10/18	7	18 UTC 5/03/15	6
00 UTC 30/10/18	3	00 UTC 6/03/15	5
06 UTC 30/10/18	2	06 UTC 6/03/15	4

Table 3.1: Frontogenesis values taken during the temporal evolution of the cyclones Vaia and Anton.
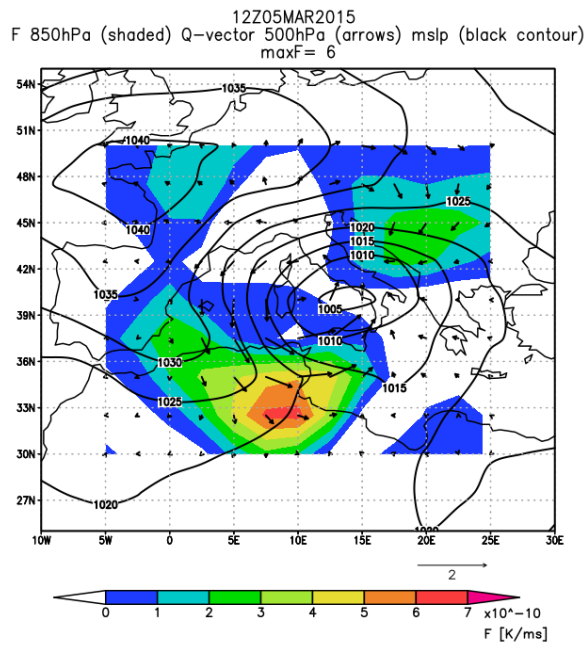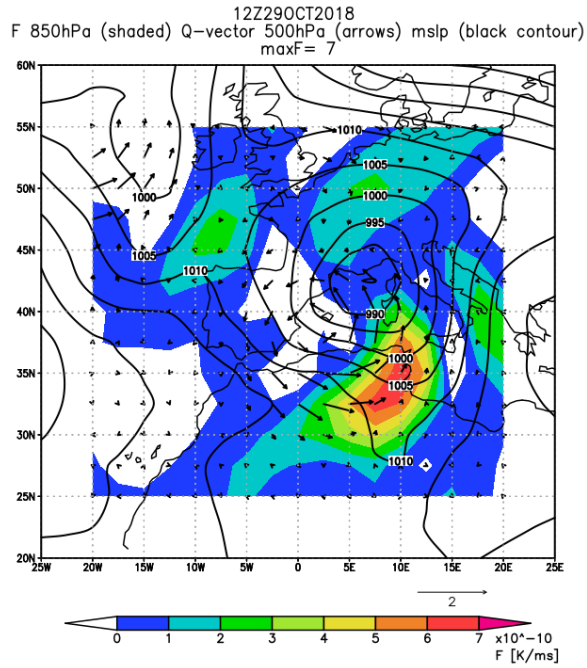
(a)

(b)

Figure 3.25:
a) Map showing the Frontogenesis function F graphed at 850 hPa (shaded), the Q-vector at 500 hPa (black arrow) and the mslp (black contour), at 12 UTC on 29 October 2018.
b) Map showing the Frontogenesis function F graphed at 850 hPa (shaded), the Q-vector at 500 hPa (black arrow) and the mslp (black contour), at 12 UTC on 5 March 2015.

Conclusions

The Q-vector has been computed and analysed for some cyclonic events.
The cyclone of reference for the whole thesis is the cyclone of the 29 October 2018, named Vaia from the free university of Berlin, and the Q-vector associated with it has been plotted and compared with other cyclones. In total, 4 cyclones were taken into consideration and from the analysis the following observations can be made on the Q-vector and on the divergence of the Q-vector.

- Different response of the vector Q-vector:

  Q-vector in Vaia is maximum (equal to $1.44*10^{-11} \frac{m^2}{kgs}$) before the formation of the low (Frontogenesis anticipates the development of the cyclone) and subsequently decreases assuming values of the order of magnitude 10^{-12} $\frac{m^2}{kgs}$ (Vaia-explosive cyclogenesis).

  Q-vector in Anton grows up to the maximum value (equal to $1.47*10^{-11} \frac{m^2}{kgs}$) a few hours before the maximum deepening and then decreases assuming values of the order of magnitude $10^{-12} \frac{m^2}{kgs}$ (Anton-explosive cyclogenesis)

  Q-vector in Klaus grows up to the moment of maximum cyclonic deepening and then decreases but never reaches the order of magnitude of $10^{-11} \frac{m^2}{kgs}$ (Klaus-explosive cyclogenesis).

  Q-vector in Qendresa is maximum (equal to $1*10^{-11} \frac{m^2}{kgs}$) in the extra-tropical phase and then decreases assuming values of the order of magnitude $10^{-12} \frac{m^2}{kgs}$ in the TLC phase where maximum cyclonic deepening is observed (Qendresa-extra-tropical cyclone in the first phase -TLC in the second phase).

- Divergence of the Q-vector:

  DivQ-Vaia absolute maximum value (equal to $-18*10^{-18} \frac{m}{kgs}$) before the formation on the ground of the low and relative maximum in the instant of maximum cyclonic deepening (equal to $-14*10^{-18} \frac{m}{kgs}$).

  DivQ-Anton maximum value (equal to $-29*10^{-18} \frac{m}{kgs}$) before the maximum cyclonic deepening.

  DivQ-Klaus maximum value (equal to $-13*10^{-18} \frac{m}{kgs}$) during maximum cyclonic deepening.

  DivQ-Qendresa absolute maximum value (equal to $-14*10^{-18} \frac{m}{kgs}$) during the extra-tropical phase.

  The temporal trend of the divergence values of the Q-vector, of the various cases, seems to mirror that of the Q-vector except in the case of Klaus.

Important information can therefore be drawn from these observations:

- The Q-vector reaches values of the order of magnitude $1 * 10^{-11} \frac{m^2}{kgs}$ only in cases of baroclinic cyclogenesis and "switches off" in the barotropic phase as seen by analyzing the maps of the cyclone Qendresa, which in the second part of evolution assumes barotropic characteristics.

- High convergence values of Q-vector are not needed to observe cyclones that have caused significant damage at the ground as deduced by studying the cyclone Vaia, which assumes an approximately average value (see chapter 5: on a record of 41 years we observe values of divergences of Q-vector also of almost $-30 * 10^{-18} \frac{m}{kgs}$).

- The Q-vector shows values of order of magnitude $10^{-11} \frac{m^2}{kgs}$ when an intense geostrophic wind variation occurs (depending on the shape assumed) and/or of intense horizontal thermal gradient (as for Vaia); in the case of the cyclone Klaus it can be assumed that it does not occur because it is in an occlusion.

- Comparing the maximum values of Q-vector, the only one that reaches a value similar to Vaia is Anton. Further analysis was performed to answer why these Q-vector values were approximately equal. In particular, the hypothesis was proposed that the high values in Anton derive from the variation of the geostrophic wind rather than from the thermal gradient and by graphing the Frontogenesis function this hypothesis was confirmed.

- In all cases, except in Vaia, if the Q-vector reaches the order of magnitude $1 * 10^{-11} \frac{m^2}{kgs}$, it assumes the maximum value when the cyclone has already formed. In the case of Vaia the maximum value of Q-vector is assumed a few hours before the development of the cyclone on the ground, therefore indicating that the conditions favorable for the development of an intense frontal structure anticipate those relating to an intense cyclogenetic development.

- Not all baroclonic cyclones reach the order of magnitude $1*10^{-11} \frac{m^2}{kgs}$ of Q-vector comparable to Vaia (see Klaus).

Chapter 4

Sensitivity Tests to identify the intensification mechanisms of the cyclone Vaia and to analyze the sensitivity of the Q-Vector.

The second part of the thesis aims at understanding the processes that have contributed to the deepening of the cyclone Vaia and at studying the sensitivity of the Q-vector and divergence.

For this purpose, *sensitivity tests* were carried out using the non-hydrostatic meteorological model MOLOCH (at a grid spacing of 1.5 km) initialized with the analyses of the ECMWF (*European Center for Medium-range Weather Forecasts*) of 15 UTC, 28 October 2018.

4.1   Meteorological numerical models

The atmosphere is a chaotic dynamical system and the physical processes that characterize it are described by partial derivative equations (PDE) that cannot be resolved analytically. Therefore it is necessary to use numerical models capable of simulating the state and the thermo-dynamic evolution of the atmosphere. Once you have established an initial condition and provided the boundary conditions, the model numerically solves the equations in a discretized space, producing a prediction of the evolution of the atmospheric variables. In addition, parameterization schemes are implemented in the models to deal with physical processes, such as radiative transfer and turbulence, which are not explicitly described in the dynamics equations. There are two categories of models:

1. General circulation models or global models (GCM - *Global Ciculation Model*), among which the main ones are the IFS (*Integrated Forecasting System of the ECMWF*) and the GFS (*Global Forecasting System* of the NCEP - *National Center for Environmental Prediction* of the United States).

2. Limited area models (LAM - *Limited Area Model*), which are divided into hydrostatic (as the BOLAM - *BOlogna Limited Area Model*) and non-hydrostatic (as the MOLOCH - *LOCAL model in Hybrid coordinates*).

High resolution non-hydrostatic models, unlike hydrostatic ones, are able to explicitly describe convective phenomena. For this study, the non-hydrostatic MOLOCH model nested in the BOLAM hydrostatic model was used. The latter receives the initial and boundary conditions from the fields of the global model of the ECMWF.
The BOLAM [4],[3] and MOLOCH models [15],[24] have been developed at the CNR-ISAC in Bologna and are used daily to make operational forecasts, as well as for research purposes. On the web page: (http://www.isac.cnr.it/dinamica/projects/forecasts/) it is possible to consult the numerical forecasts and also find a detailed description.

Figures 4.1 a) and 4.1 b) represent the scheme of the procedure followed to perform the simulations starting from the initial conditions of the ECMWF model at 15 UTC, 28 October 2018.
The steps followed to perform the simulations are shown in Figure 4.1 (numbers in orange) and can be summarized in 4 phases:

1. Creation of the domain of integration and interpolation of the physiographic databases (soil / vegetation fields / orography)

2. Pre-processing: interpolation of meteorological fields on the model grid to prepare the initial condition and the boundary conditions

3. Simulation

4. Post-processing: interpolation of the model output on standard isobaric levels or elevations in order to generate the graphics

This procedure was carried out first for the BOLAM run and subsequently for the MOLOCH model.

(a)

(b)
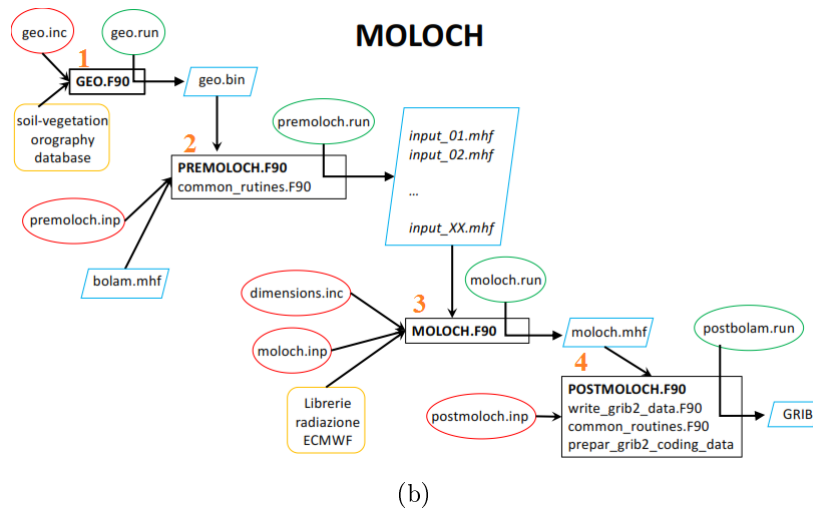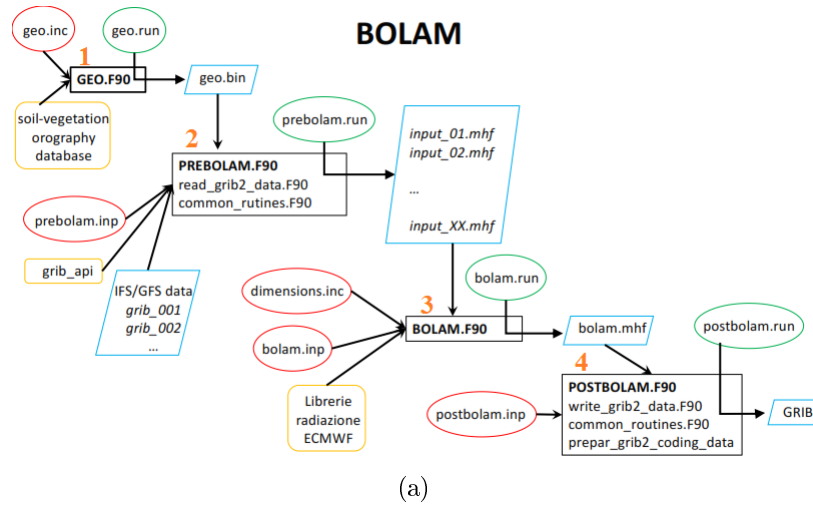
Figure 4.1:
Illustrative diagram of the different phases necessary to perform a run with the BOLAM model a) and subsequently with the MOLOCH b). As shown in Figures a) and b), the simulation configuration and management files are circled in red and green, the input or output data in blue, the codes in black and the databases and libraries in yellow.

4.2 Sensitivity Tests

Sensitivity tests are numerical experiments carried out with a meteorological model, which consist in modifying some aspects of the simulation, such as for example the calculation of some physical processes or the conditions surrounding the simulations and possibly the integration domain, to see how the atmospheric system evolution changes with respect to a simulation taken as a reference. The *sensitivity tests* were compared with the control run (RUN CNTR), corresponding to the configuration used for the operational runs at the ARPAL weather center (Regional Agency for the Protection of the Environment of Liguria region). The following sensitivity experiments were performed:

1. RUN BOUNDARYSUD: reduction by 75% of the specific humidity entering the South boundary, thus reducing the contribution of moisture transport from remote tropical areas.

2. RUN NOLH: zeroing the contribution of latent heat release of all the processes related to the phase changes (for example, condensation) in the atmosphere.

3. RUN NOSFCFLUX: zeroing of the contribution of both sensitive and latent surface heat fluxes all over the sea points of the domain.

For sake of clarity, in the following the Figures are organized always in the following way:

- Top left: RUN CNTR A)

- Top right: RUN BOUNDARYSUD B)

- Bottom left: RUN NOLH C)

- Bottom right: RUN NOSFCFLUX D)

4.2.1 Which physical processes have contributed most to the development of the cyclone Vaia?

Below are mean sea level pressure images (MSLP) considered significant to highlight the differences between the different runs and therefore understand the role of the different contributions.
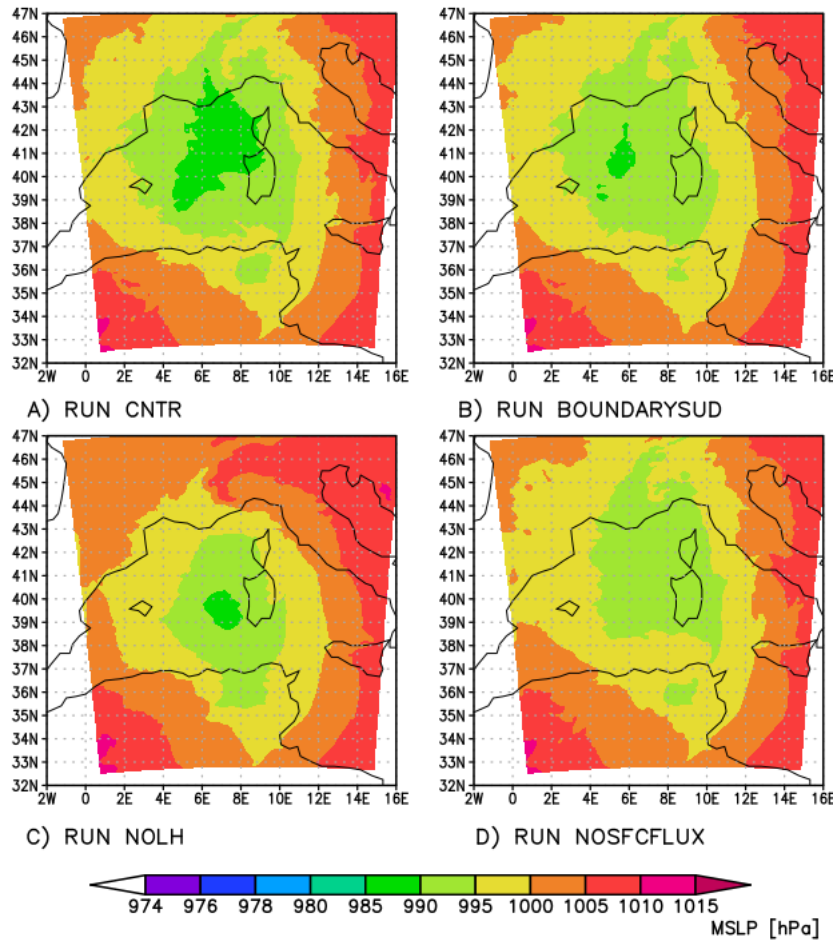
Figure 4.2: Comparison between the mslp *patterns*, referring to 06 UTC of 29 October 2018, between the run CNTR A) and the different runs of the *sensitivity* experiments.

In Figure 4.2, in which the surface pressure fields referring to 06 UTC of 29 October 2018 are compared in the various experiments, that is, at the instant corresponding to the first phase of cyclone development, it is evident that the cases B) and C) differ only slightly from the control run A) while case D), in which the heat fluxes from the sea surface have been removed, shows a weaker deepening of the low. This means that in the first phase of development, sensitive heat and humidity (latent heat) fluxes from the sea surface played an important role while the release of the latent heat into the atmosphere did not significantly affect the cyclone deepening.

A similar analysis was conducted at 15 UTC on 29 October 2018, that is in the phase of maximum cyclone development (Figure 4.3).
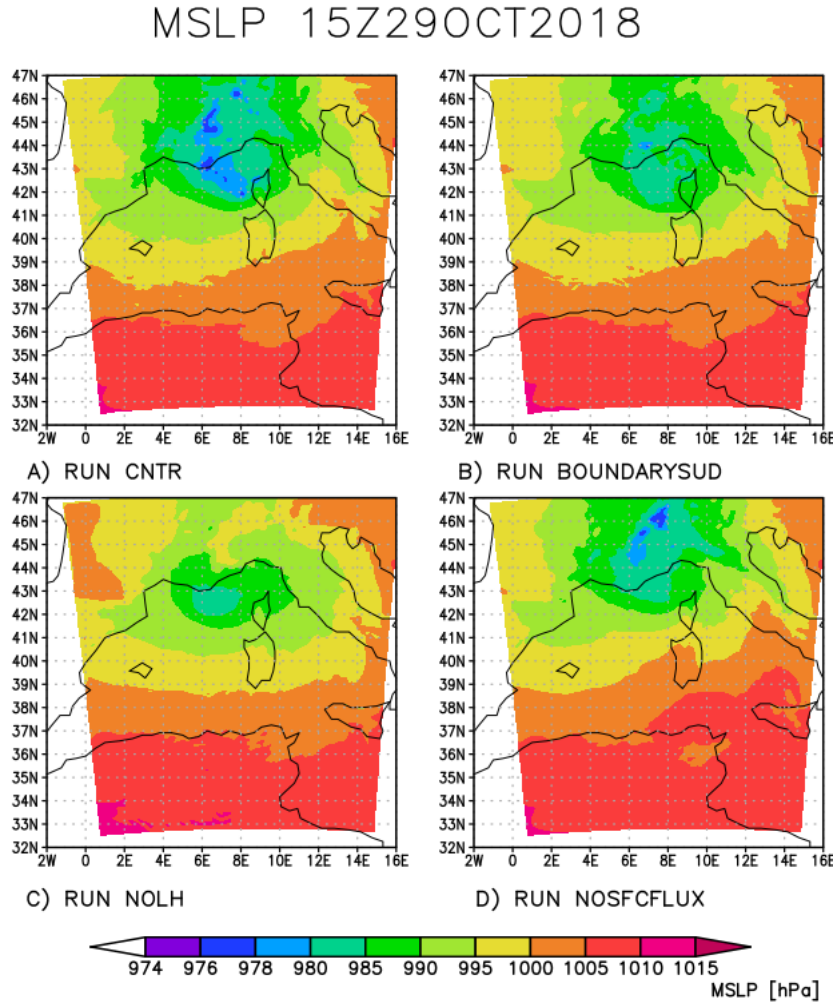
Figure 4.3: Comparison between the mslp *patterns*, referring to 15 UTC of 29 October 2018, between the run CNTR A) and the different runs of the *sensitivity* experiments.

In this phase the pressure *pattern* of case D) is similar to that of the control run: this means that in the mature phase the heat fluxes from the sea did not provide a significant contribution. The most relevant difference with respect to the control run is the position of the low. Compared to what was observed in the first phase of development, cases B) and C) show instead a decidedly shallower low compared to the control run: this indicates that the release of latent heat played an important role in this phase. This interpretation is also confirmed by what is shown by the analysis of the equivalent potential temperature (θ_e - *equivalent potential temperature*)[1] (Figure

---

[1]*potential temperature that a parcel of air would have if all its moisture were condensed and the*

4.4) and of the precipitable water (PW - *precipitation water*) [2] (Figure 4.5).

It can be seen that:

- In case B), the advection of warm and humid air (identified by the areas with $\theta_e > 305$ K (θ_e, Figure 4.4) is much weaker than in the control run with consequent lower values of precipitable water (Figure 4.5). Having drastically reduced the contribution of humidity coming from tropical areas, the quantity of water vapor in the atmosphere transported towards the cyclone on the Mediterranean has been reduced. In doing so, the fuel for condensation has been effectively removed, therefore indirectly decreased the release of latent heat.

- In case C), the field of θ_e (Figure 4.4) is similar to that of the control run except from the vicinity of the area experiencing the most intense pressure drop but, it is observed that the quantity of precipitable water (Figure 4.5) is smaller. The result can be explained considering that, by removing the release of latent heat, the atmosphere is colder, and therefore the condensation of the water vapor occurs more easily, since the saturation point is reached earlier. In addition, the vapor is extracted from the atmosphere in the form of precipitation. This hypothesis is confirmed by the cumulative rain map, in which, case C) highlights higher cumulated rainfall than the control run (Figure 4.6).

---

resultant latent heat used to warm the parcel. The temperature of an air parcel can be brought to its equivalent potential value by raising the parcel from its original level until all the water vapor in the parcel has condensed and fallen out and then compressing the parcel adiabatically to a pressure of 1000 hPa.(J. R. Holton, 2004)

[2]*thickness of liquid water, measured in mm (or Kg/m^2), resulting from the condensation of all the water vapor contained in a vertical atmosphere column over an area of one square centimeter.*
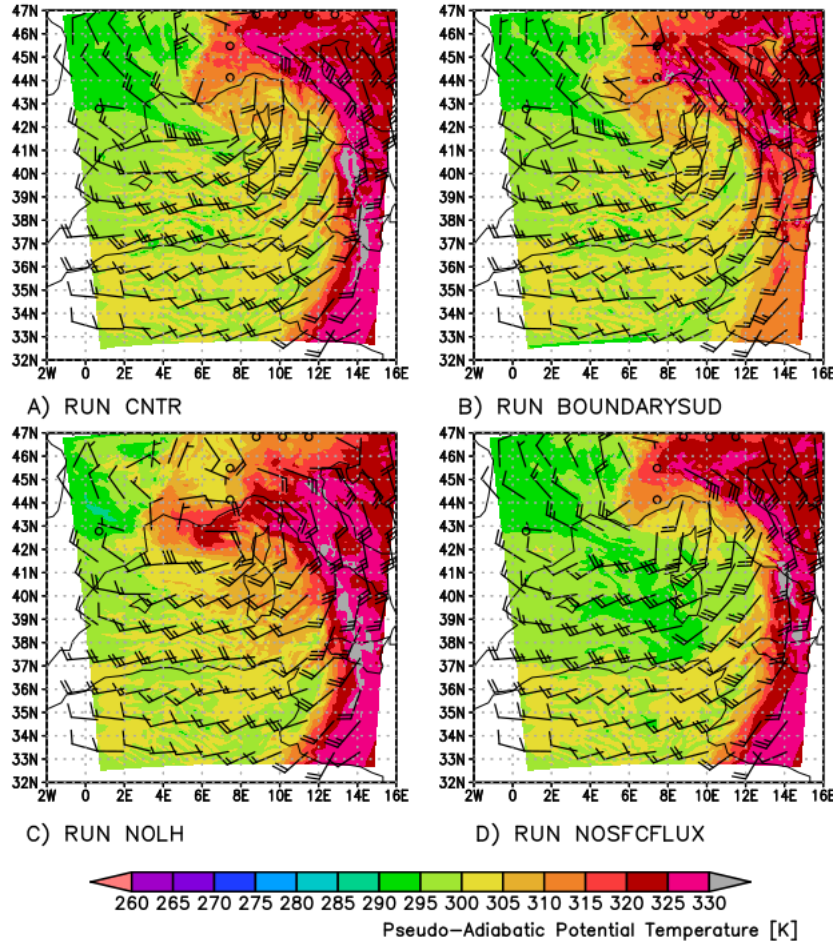
Figure 4.4: Comparison between the *patterns* of potential temperature equivalent to 850 hPa, referred to the 15 UTC of 29 October 2018, between the run CNTR A) and the different runs of the *sensitivity* experiments.

Figure 4.5: Comparison between the *patterns* of precipitable water, referred to the 15 UTC of 29 October 2018, between the run CNTR A) and the different runs of the *sensitivity* experiments.

Figure 4.6: Comparison between the *patterns* of cumulative rainfall in 33 hours, referred from 16 UTC on 28 October to 00 UTC on 30 October, between the run CNTR A) and the different runs of the *sensitivity* experiments.

What happens using a different integration domain?

To carry out the sensitivity analysis on the Q-vector for the Vaia cyclone, the simulations have been run again but on a larger domain. The comparison between the results of the *sensitivity tests* in the two different domains allows to draw some further conclusions on the relevant physical processes. The integration domain between $23.79°N - 47.79°N$ latitude and $-18.33°W - 21.45°E$ longitude has been called DOM1 (Figure 4.7). In the following figures, however, in order to facilitate the comparison of the results with that obtained in the experiments with MOLOCH on the small domain (indicated as DOMO in Figure 4.7 red box) the outputs have been displayed on the same area, that is between $32.43°N - 46.98°N$ latitude and $-1.2°W - 16.29°E$ longitude (that is the same coordinates as the red box in Figure 4.7).

From the comparison between Figures 4.3 and 4.8, it is observed that the most evident differences between the runs on the two domains are in the RUN CNTR A) and in the RUN BOUNDARYSUD B).

By comparing the CNTR RUNs of Figures 4.3 and 4.8, it is observed that the variation of the integration domain produces an effect, albeit marginal, on the pressure field associated with Vaia. These differences, however, are compatible with the perturbation that the different *setup* implies to the numerical integration. On the contrary, the differences between case B) of Figures 4.3 and 4.8 are more marked. It is important to note that, in the large domain, the decrease in humidity by 75 % on the southern boundary does not entail the reduction of the vapor transported from the tropical regions, as this boundary is located further South than the latitude in which this transport takes place. Therefore the comparison of the simulations on the two domains allows us to conclude that the contribution of humidity coming from remote regions with respect to the Mediterranean was significant for the deepening of the cyclone Vaia. A previous study in fact [8] has shown the important role of an *atmospheric river* in the lower troposphere capable of carrying high quantities of moisture from the tropics to the Mediterranean. In certain synoptic situations, an *atmospheric river*, may develop in correspondence of the *low-level jet* positioned ahead of the cold front associated with an extra-tropical cyclone. To further highlight the effect of the *atmospheric river* maps of precipitable water are provided (Figure 4.5 B and Figure 4.9 B). It is presumable that, in the absence of the *atmospheric river*, the shift of the position of the *boundary south*, would not have produced significant differences between the two domains (also in the deepening of the low). Therefore, the comparison of the *sensitivity tests* of the two domains, allowed to support our previous conclusion: in the first phase of development of the cyclone the contribution of heat fluxes from the sea was significant; in the second phase, the transport of humidity by the *atmospheric river* provided a critical contribution to the deepening of the cyclone Vaia.
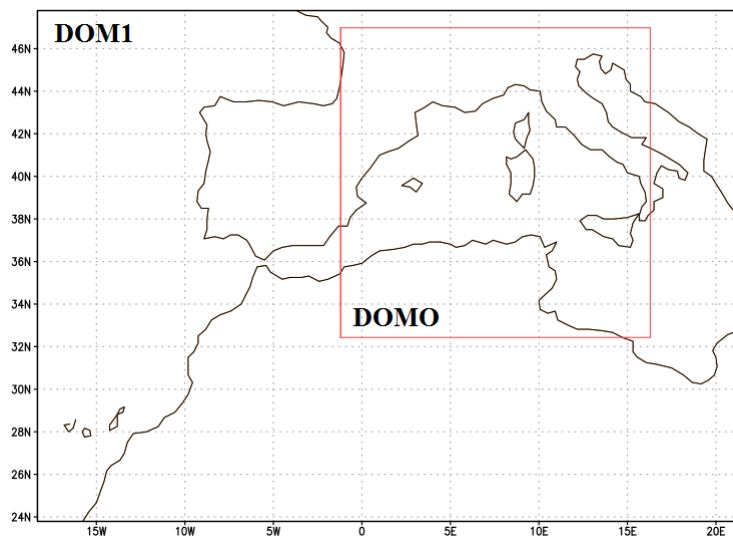
Figure 4.7: Enlarged domain of MOLOCH and the zoom (red box) which was considered to compare the sensitivity tests carried out on the original domain of MOLOCH.
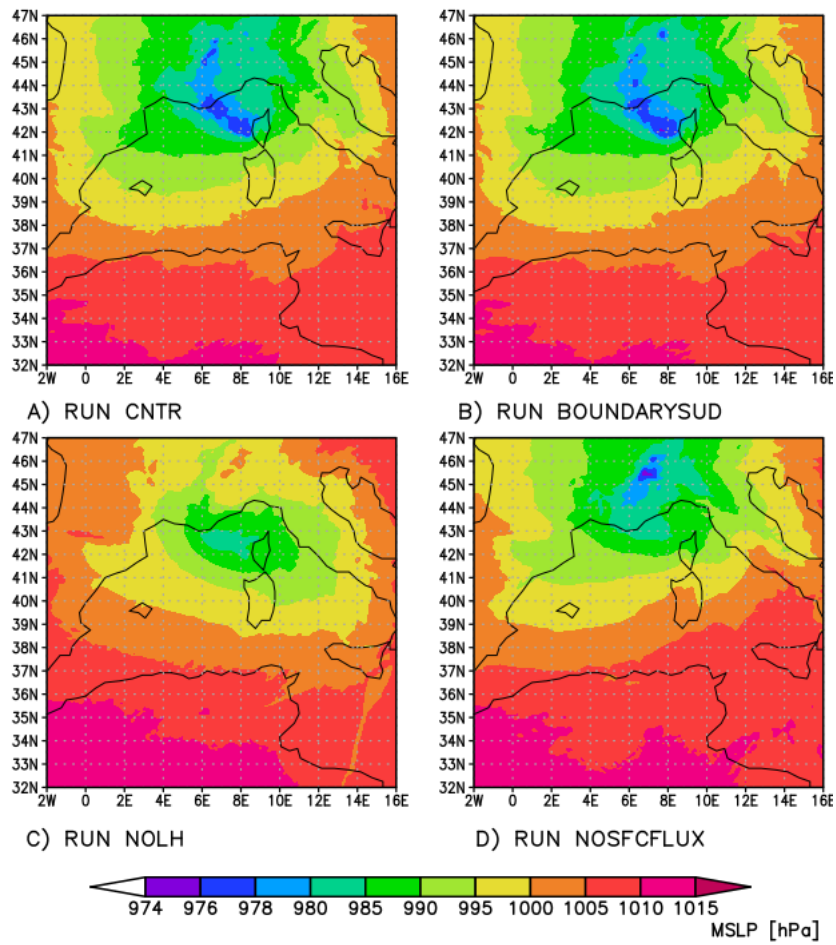
Figure 4.8: Comparison between the mslp *patterns*, referring to 15 UTC of 29 October 2018, between the run CNTR A) and the different runs of the *sensitivity* experiments.
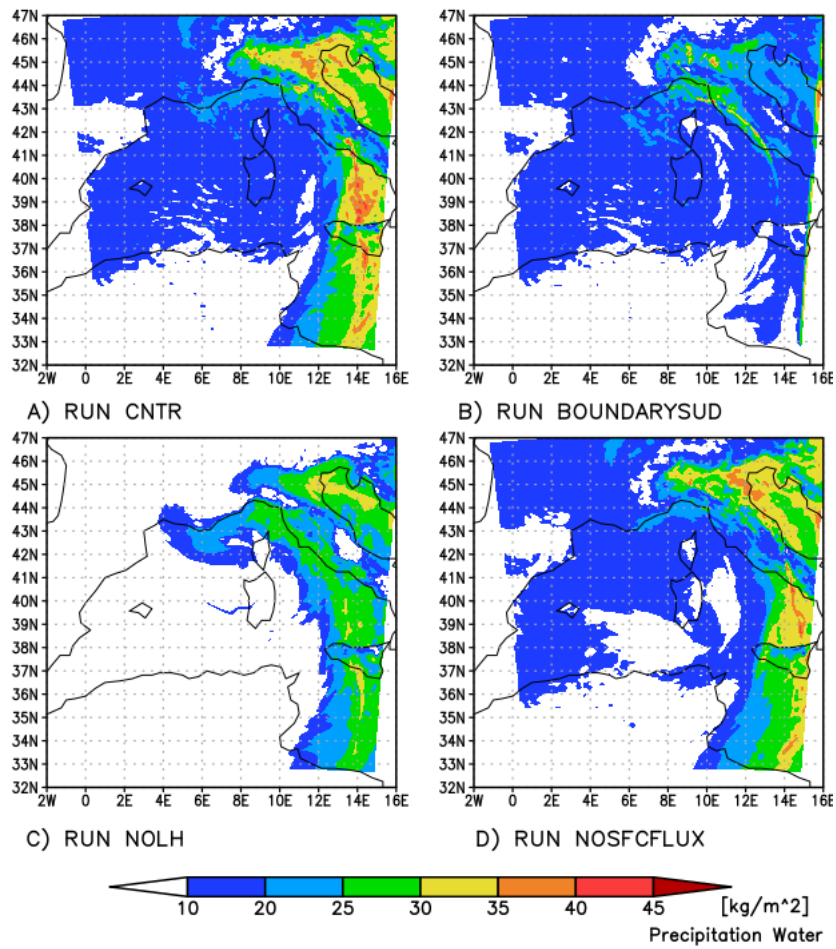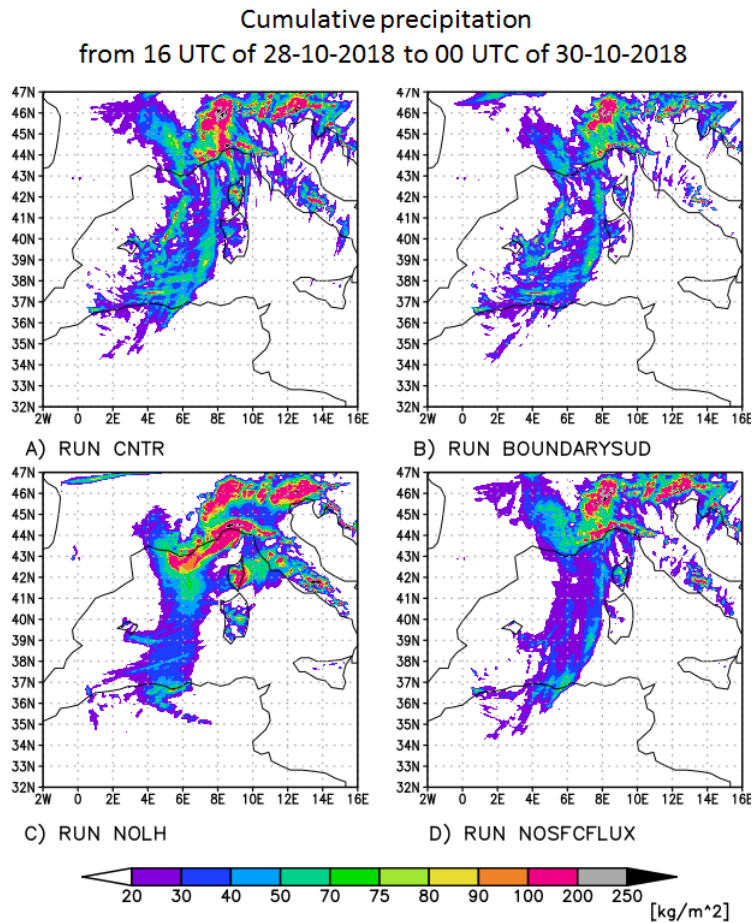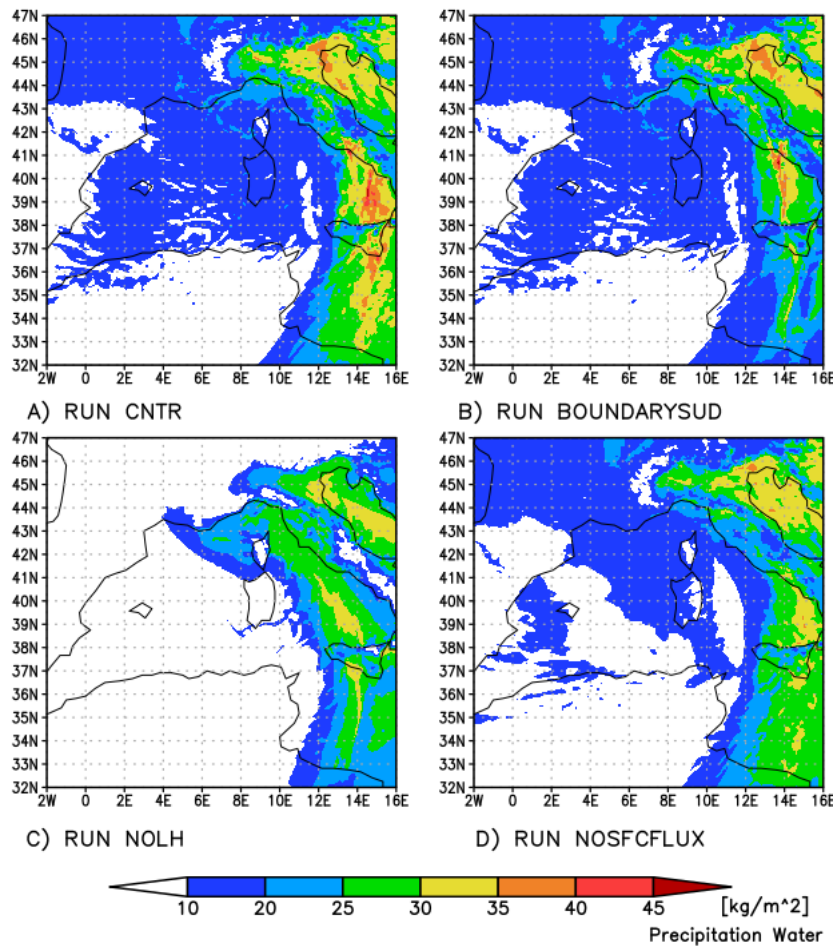
Figure 4.9: Comparison between the *patterns* of precipitable water, referred to the 15 UTC of 29 October 2018, between the run CNTR A) and the different runs of the *sensitivity* experiments.

4.2.2 Sensitivity of the Q-vector and associated divergence

A final analysis was conducted on the sensitivity of the Q-vector and its divergence. Both the Q-vector and the divergence in the cyclone Vaia have already been analyzed in chapter 2, using NCEP reanalysis, but it was considered interesting to evaluate their sensitivity with respect to the processes analyzed in the *sensitivity tests* carried out with the MOLOCH model, that means heat fluxes from the sea surface, transport of humidity and release of latent heat in the atmosphere. It is important to underline that the results come from different *datasets*; the initial and boundary conditions for the simulations performed with the MOLOCH model are provided by the ECMWF, while the NCEP reanalyses are produced through the GFS model. The Q-vector has a noisy field if plotted at high resolution, thus it was necessary to regrid the MOLOCH fields from a high resolution of 0.02 degrees to a lower resolution of 2.5 degrees. In both cases, the Q-vector displays the maximum value at 18 UTC on 28 October 2018. At this time Figure 4.10 shows the *outputs* of the *sensitivity tests* carried out with MOLOCH, from which the following observations can be made:

- The Q-vector and divergence values of case B) deviate for the first decimal place from the control run. Therefore it can be assumed that, at least in the first phase of cyclone development, the removal of 75% of specific humidity does not produce significant changes in the Q-vector. Note that, using the large domain, this experiment does not remove the *atmospheric river*. This explain the very low impact observed.

- The only case in which both the Q-vector and its divergence differ from the control run is C). The removal of latent heat release in the atmosphere led to an increase in the value of the Q vector and in the divergence.
  It can be assumed that in the control run, the release of latent heat favors the vertical and ageostrophic circulation (it favors the heating of the particles in the lower troposphere, therefore the vertical ascending motions in the warm sector), which tends to reduce the thermal gradients and therefore also the values of Q-vector. In fact, vertical circulation induces a downward movement behind the cold front (therefore adiabatic heating) and upward movement ahead of the front (adiabatic cooling partially compensated by diabatic effects), which therefore has the effect of reducing the horizontal thermal gradient and therefore the Q-vector. In case C) the contribution of the latent heat is turned off, therefore the vertical circulation is reduced, the thermal gradients do not decrease and therefore the Q-vector values are higher.

- The Q-vector and divergence values of case D) are identical to those of the control run. Therefore it can be assumed that, at least in the first phase of cyclone development, the removal of latent heat fluxes from the sea does not affect the Q-vector values. This can be explained by the fact that the fluxes have not had enough time yet to impact on the dynamics.
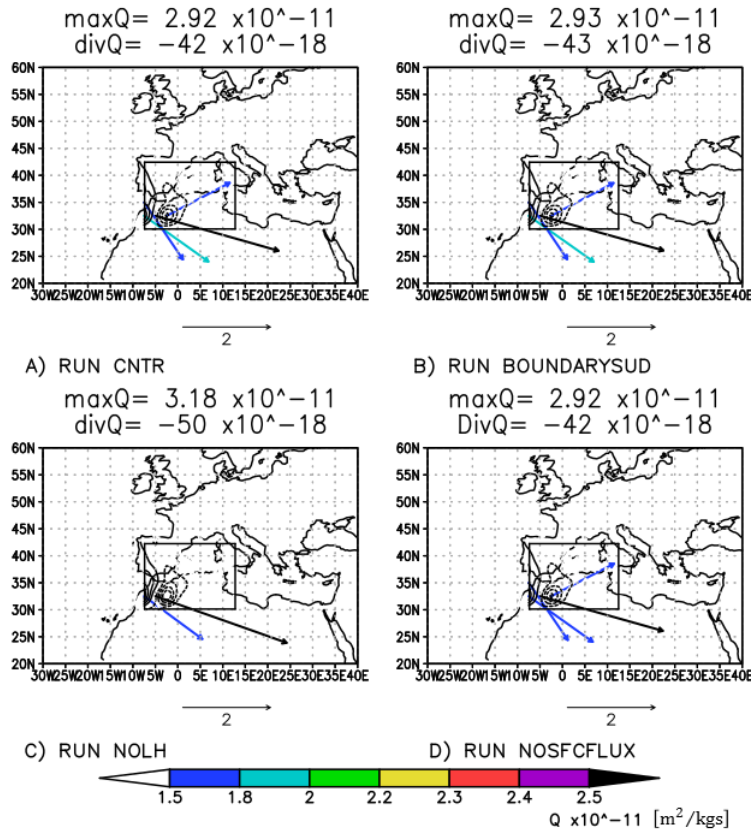
Figure 4.10: Comparison between the Q-vector and associated divergence, at 18 UTC of 28 October 2018, between the run CNTR A) and the different runs of the *sensitivity* experiments. The colored vectors represent the Q-vector with a modulus larger than $1.5 * 10^{-11} \frac{m^2}{kgs}$ while the black contours represent the divergence of the Q-vector. Above each panel, the maximum values of Q-vector (MaxQ) and divergence (divQ) of the domain have been reported.

Finally, to obtain additional information, it was decided to analyse the temporal evolution of the Q-vector values and its divergence for the *sensitivity tests* in Figure 4.11 and make a comparison with the CNTR run.
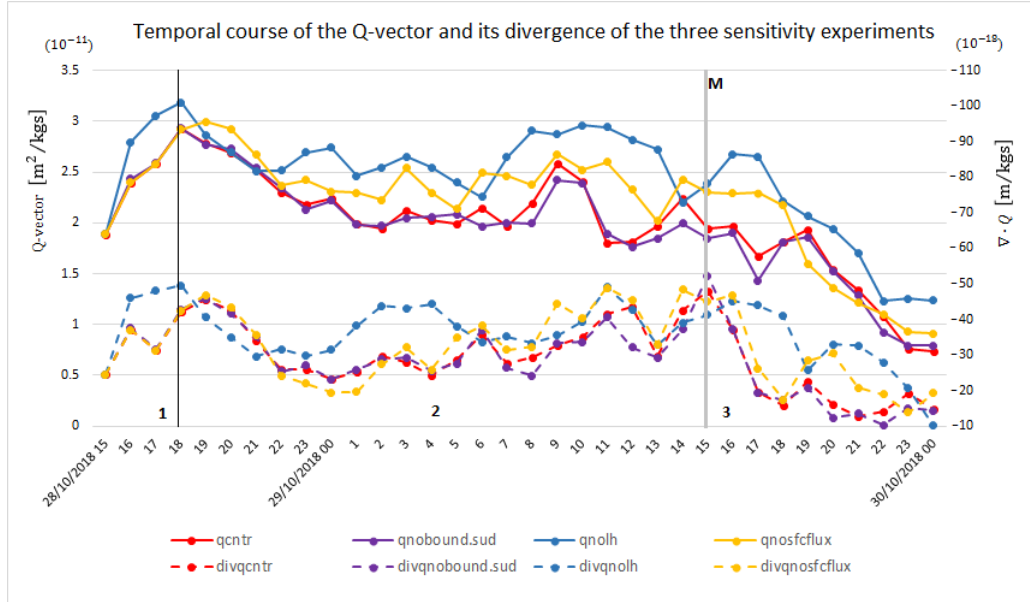
Figure 4.11: Temporal evolution of the Q-vector values and divergence computed for the *sensitivity tests*, compared with the control run. The solid lines represent the values of Q-vector and the dotted lines represent, the divergence of the Q-vector. The gray line (M) identifies the phase of maximum cyclone deepening. Boxes 1, 2 and 3 identify the phases of formation, development and maturity of the cyclone Vaia.

Figure 4.11 defines three distinct time phases:

PHASE 1 identifies the formation of the cyclone Vaia (from 15 UTC on 28 Oct. to 18 UTC on 28 Oct.)

PHASE 2 identifies the rapid development of the cyclone (from 18 UTC on 28 Oct. to 15 UTC on 29 Oct.)

PHASE 3 corresponds to the cyclone's maturity (from 15 UTC on 29 Oct. to 00 UTC on 30 Oct.)

The following conclusive observations can be made from the comparison of *sensitivity tests* with the CNTR run:

RUN CNTR-NOBOUNDARYSUD:

The trends of Q-vector and divergence are nearly identical.
This can be explained by the fact that the contribution of humidity coming from the *Atmospheric River* is not removed as it is already present in the domain.

79

RUN CNTR-NOLH:

In almost all 34 hours of analysis, the evolution of the Q-vector values and the divergence are similar for the CNTR and NOLH runs. In the NOLH run, however, the values are always higher, for the reasons described above.

RUN CNTR-NOSFCFLUX:

PHASE 1 The values of the Q-vector and the divergence almost coincide with those of the CNTR run, because the impact of the fluxes from the surface had not enough time yet to change the dynamics.

PHASE 2 The values of the divergence of the Q-vector are very similar to the values present in the run CNTR, while the values of the Q-vector are in between those of the run CNTR (red line) and the NOLH run(blue line).

PHASE 3 The values of the Q-vector and its divergence are mainly comprised between the CNTR run (red line) and the NOLH run (blue line).

Therefore, this confirm the hypothesis that surface latent and sensible heat fluxes from the sea provide a smaller contribution than the latent heat release in the mature stage.

Conclusions

- From the original domain of the MOLOCH model, the processes that contributed to the deepening of the Vaia cyclone are: in the first phase of development, the fluxes of sensible heat and humidity (latent heat) from the surface while the release of latent heat in the atmosphere did not provide a significant influence. Instead, the release of latent heat in the atmosphere played an important role in the mature phase. The analysis of the results on a larger domain identifies the role of an important physical phenomenon for the deepening of the cyclone Vaia: in the second phase (the mature one), the contribution of humidity carried by the *atmospheric river* turned out to be critical.

- From the study of the sensitivity of the Q-vector and the divergence, the only experiment that differs significantly from the control is the one in which the release of latent heat into the atmosphere is removed (case C) Figure 4.10). In this experiment the values of Q-vector and divergence are systematically higher than the reference run. This has been attributed to the weakening of vertical circulation in the absence of heat release, which maintains more intense thermal gradients.

Chapter 5

Climatological analysis

5.1 Climatological analysis

To understand how Vaia fits into the climatology of Mediterranean cyclones and if it can actually be considered a "rare" event, not only for the effects on the ground but also for the Q-vector values associated with it, it was proposed to continue the study with a climatological analysis of Mediterranean cyclogenesis.

It was decided to use the Q-vector theory to identify cyclones starting from NCEP reanalysis data from 1979 to 2020. Subsequently, this dataset was compared with a dataset from the MEDEX archive to check whether the selected cyclones were correct. In literature there is an archive of Mediterranean cyclones developed within the MEDEX project - *MEditerranean EXperiment* [14] and this archive is composed of three types of datasets:

- Analysis gribs from ECMWF forecast model (0.5x0.5 degrees lat/lon); entire Mediterranean; from June 1998 to May 2004 [12].

- Analysis gribs from HIRLAM forecast model (0.5x0.5 degrees lat/lon); Western Mediterranean (up to $18°E$); from June 1995 to May 2004 [19].

- Gribs from ERA-40 reanalysis (from ECWWF) (1.125.5x1.125 degrees lat/lon); entire Mediterranean; from September 1957 to August 2002 [6].

It was therefore decided to compare the results obtained in the present study using the Q-vector theory with the dataset created using the HIRLAM model, more suitable as regards the time period investigated. This dataset, from the MEDEX archive, was not used from the beginning in this thesis work for two reasons: firstly it is not updated in the recent years and consequently the cyclone Vaia is not included; secondly it holds all the cyclones and not just the most intense ones. For these two reasons, we have chosen to follow the method proposed here, to identify the most intense cyclones and with Q-vector values comparable to those of the Vaia cyclone.

During the verification phase, the comparison between the two datasets confirmed that the events selected with the Q-vector theory are all cyclones.

The following discussion explains how the Mediterranean cyclone dataset is created

using the Q-vector theory.

It is important to highlight that the work carried out has only a qualitative value and would need further investigation.

In particular, only the months of maximum baroclinicity were analyzed, from September to March. For each available instant of time, that is every six hours, the values of Q-vector and its divergence were calculated, on an area that mainly includes the Central-Western part of the Mediterranean. On this domain, between the latitude coordinates $15°N - 55°N$ longitude $20°W - 30°E$, the maximum values of Q-vector were first calculated. Having found that the order of magnitude of Q-vector ranges between $10^{-13} \frac{m^2}{kgs}$ and $10^{-11} \frac{m^2}{kgs}$ it became necessary to identify which order of magnitude was representative of events comparable to Vaia. For this purpose, observing the values of Q-vector assumed by the cyclone Vaia, it was hypothesized that the order of magnitude of the Q-vector was reasonable to define its specificity. Thus the first selection was made, that is, it was decided to keep the cases in which the Q-vector values equaled or exceeded the reference value $1 * 10^{-11} \frac{m^2}{kgs}$. Finally, the event dataset was further refined in a "subjective" way, i.e. by analyzing the ground pressure maps - potential temperature at 850 hPa - Q-vector - divergence of Q-vector by selecting the events meeting the following criteria:

1. Presence of a pressure low

2. The cyclone affected the Mediterranean Sea during its dynamic evolution

3. The calculated maximum Q-vector value was actually corresponding to the identified minimum pressure and not to any other structures present on the same domain at the same time.

In the event of a negative outcome, even for only one criterion, the event has been definitively discarded. With regard to the selected events, those that affected the eastern Mediterranean were excluded, since other dynamics come into play.

One of the biggest difficulties encountered was answering the third question, as the dataset has low resolution (2.5 x 2.5 degrees). Furthermore, the maximum Q-vector values were not always positioned near the minimum pressure. In conclusion, as regards the answer to this question, it is believed that the subjective method used here may be affected by a certain margin of uncertainty for some events. The main trajectories performed by the pressure low on the area of interest, have been reported in Figure 5.1, in which the red arrows represent the paths of the cyclones that have been examined, while the dotted paths represent those of the cyclones excluded.

The procedure described above led to the identification of 90 potentially significant events, that is baroclinic systems that could have produced widespread damage to the ground soil over large areas such as the cyclone Vaia. There is a further difficulty encountered in the "verification" phase, that is when we have tried to find historical evidence of the damage to the ground caused by cyclones, corresponding to the dates selected by this study, as events more distant in time are often not documented online (presumably in cases where the event did not affect large and largely urbanized portions of territory, or if it did not produce significant damage).

Figure 5.1: Trajectories

5.1.1 Statistical analysis

To carry out statistical analyses on the data, it was considered appropriate to separate the events into two groups with reference to the astronomical season (autumn (23 Sep - 21 Dec) and winter (22 Dec - 20 Mar)) in which they occurred. The astronomical season is used since in September from 1979 to 2020 there are no significant events and therefore it is okay to start from September 23 while if the weather season (autumn (1 Sep - 30 Nov) and winter (1 Dec) had been used - 28/29 Feb)) the events detected in March would have been lost which, as it will be seen, are important. In this way, two groups were considered, of which 39 events were found to fall in the autumn astronomical season and 51 in the winter astronomical season and for each group a reference cyclone was chosen: the cyclone *Vaia* of 29 October 2018 for the autumn category and the cyclone *Anton* of 5 March 2015 for the winter one because it was already analyzed in chapter 3.

On both samples, the following analyses were conducted:

- Intensity frequency of the Q-vector and its divergence

- Correlation between Q-vector and divergence

Finally, taking into consideration all the events, a comparison was made on the temporal trend of Q-vector and divergence to try to highlight any seasonal climatological trend.

AUTUMN

The 39 events selected are listed in the table in Figure 5.2 where, for each event, the maximum value of Q-vector and associated divergence and the date of occurrence was reported.

N°	Date	Q-vector ($10^{-11} \frac{m^2}{kgs}$)	$\nabla \cdot Q$ ($10^{-18} \frac{m}{kgs}$)
1	21/12/1979	1.06	-18
2	19/12/1980	1.12	-13
3	01/12/1983	1.18	-11
4	23/11/1987	1.10	-16
5	05/12/1990	1.06	-16
6	09/12/1990	1.37	-18
7	20/12/1991	1.08	-27
8	22/10/1993	1.10	-12
9	04/11/1993	1.17	-13
10	04/11/1995	1.23	-14
11	12/12/1995	1.04	-12
12	24/11/1996	1.10	20
13	01/12/1996	1.06	-17
14	21/12/1998	1.09	-11
15	06/11/1999	1.07	-16
16	19/11/1999	1.13	-25
17	22/11/1999	1.10	-17
18	14/10/2000	1.08	-9
19	10/11/2001	1.46	-24
20	13/12/2001	1.23	-17
21	03/12/2003	1.21	-17
22	12/12/2003	1.19	-13
23	13/11/2004	1.06	-9
24	13/11/2005	1.22	-12
25	03/12/2008	1.50	-24
26	14/12/2008	1.05	-16
27	10/10/2011	1.00	-15
28	28/10/2012	1.09	-23
29	08/12/2012	1.02	-19
30	10/10/2013	1.23	-17
31	17/11/2013	1.05	-16
32	22/10/2014	1.14	-15
33	06/11/2014	1.04	-14
34	10/12/2014	1.24	-16
35	13/12/2014	1.12	-13
36	13/11/2017	1.21	-13
37	28/10/2018	1.44	-18
38	11/11/2019	1.39	-18
39	16/11/2019	1.16	-15

Figure 5.2: List of events selected for the autumn season (23 Sep - 21 Dec).

Frequency of the Q-vector and divergence

Analyzing the Figure 5.3, which shows the frequency of the maximum Q-vector value associated with the cyclones in the 39 autumn cases, it is observed that:

- 41% of events has a Q-vector value between $(1 - 1.1)10^{-11} \frac{m^2}{kgs}$

- 28% of events has a Q-vector value between $(1.1 - 1.2)10^{-11} \frac{m^2}{kgs}$

- 18% of events has a Q-vector value between $(1.2 - 1.3)10^{-11} \frac{m^2}{kgs}$

- 5% of events has a Q-vector value between $(1.3 - 1.4)10^{-11} \frac{m^2}{kgs}$

- 8% of events has a Q-vector value between $(1.4 - 1.5)10^{-11} \frac{m^2}{kgs}$
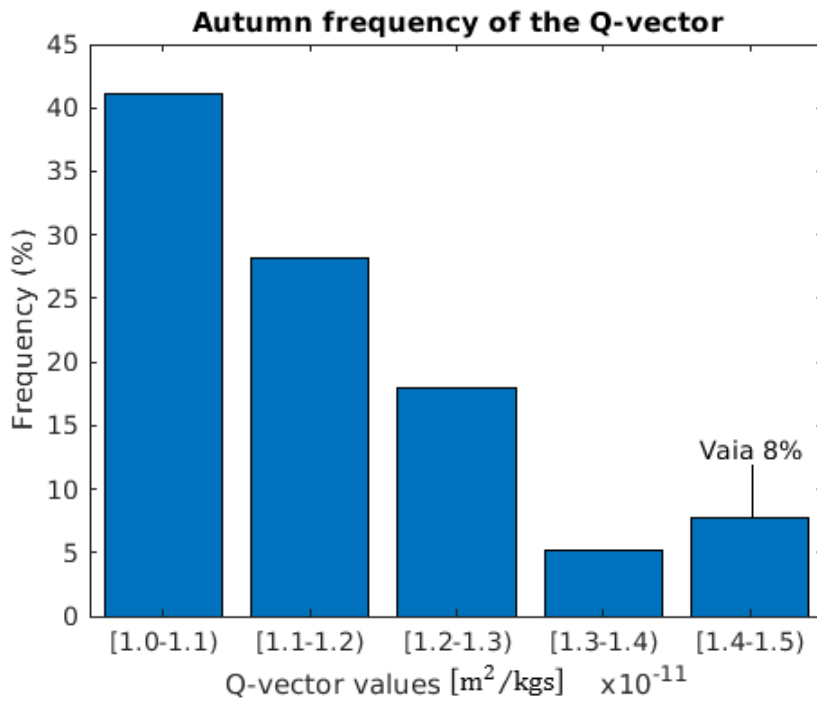
Figure 5.3: Frequency of Q-vector values in the autumn season from 1979 to 2020.

The cyclone Vaia falls in this latter class of events, consisting of only 3 cyclones in 41 years; this indicates that events with Q-vector values including $(1.4 - 1.5)10^{-11} \frac{m^2}{kgs}$ have been observed rarely in the fall season in the past 40 years. To assess the rarity against the whole sample, percentiles were used. Vaia falls into the $95th$ percentile and this seems to confirm the hypothesis that it was a rare event, as regards the Q-vector values.

The Figure (5.4) shows the frequency distribution of the divergence of the Q-vector from which it is observed that:

- about 8% of events has a Q-vector divergence value between $-(8-11)10^{-18}\,\frac{m}{kgs}$

- about 26% of events has a Q-vector divergence value between $-(11-14)10^{-18}\,\frac{m}{kgs}$

- about 31% of events has a Q-vector divergence value between $-(14-17)10^{-18}\,\frac{m}{kgs}$

- about 20% of events has a Q-vector divergence value between $-(17-20)10^{-18}\,\frac{m}{kgs}$

- about 0% of events has a Q-vector divergence value between $-(20-23)10^{-18}\,\frac{m}{kgs}$

- about 13% of events has a Q-vector divergence value between $-(23-26)10^{-18}\,\frac{m}{kgs}$

- about 2% of events has a Q-vector divergence value between $-(26-29)10^{-18}\,\frac{m}{kgs}$
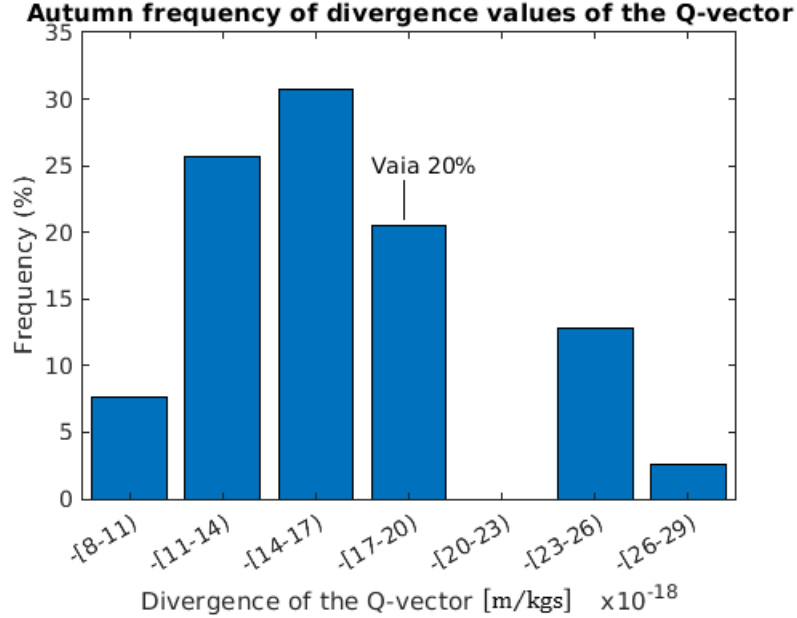

Figure 5.4: Frequency of Q-vector divergence values in the autumn season from 1979 to 2020.

In light of this distribution, we have tried to understand why there were no events with divergence of the Q-vector between $-(20-23)10^{-18}\,\frac{m}{kgs}$. The divergence values were analysed again for each year and it was found that, a value belonging to this

range, was assumed by 8 of the 39 events but that did not occur at the same time as the maximum Q-vector value. Remember that the selection was made on the values of Q-vector calculated with the associated divergence taken at that same instant.

In the frequency distribution of the divergence of the Q-vector, the cyclone Vaia falls into the 4th group with 20% of the total of cases (8 events out of 39). Viewed in terms of percentiles, it falls into the $80th$ percentile so, taking into account only this variable, it cannot be said that the dynamics of this extreme event were rare.

Correlation between Q-vector and divergence of the autumn season

Below, in Figure 5.5, the correlation between Q-vector and its divergence for the autumn season has been reported.

Looking at Figure 5.5, the whole sample of autumn events turns out to be divided into two groups; one more populated - precisely composed of 34 events - on the left, with Q-vector values less than $1.30 * 10^{-11}$ $\frac{m^2}{kgs}$ and divergence between $-(8 - 28) * 10^{-18}$ $\frac{m}{kgs}$ and one on the right, with only 5 events with a Q-vector greater than $1.30 * 10^{-11}$ $\frac{m^2}{kgs}$ e with divergence values in the range $-(17 - 25) * 10^{-18}$ $\frac{m}{kgs}$.

The next step was to try to answer the question of whether there was a correlation between the extent of the effects on the ground of a cyclogenetic event and the values of Q-vector and divergence associated with it. As already mentioned, it was not possible to find documents attesting to the damage to the ground caused by all events. Information was found only for the events indicated in Figure 5.5 with a red dot, the blue square indicating the cyclone Vaia.
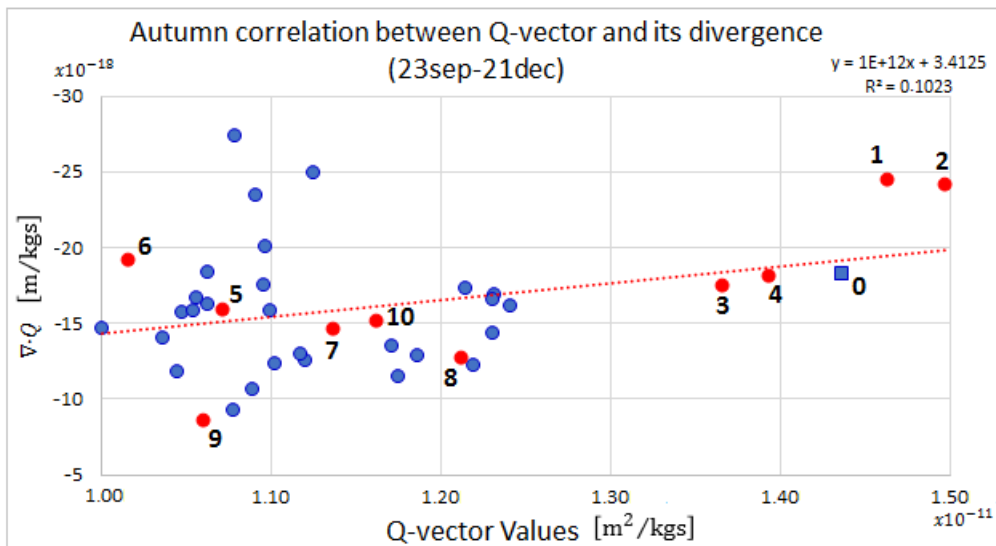
Figure 5.5: Correlation between Q-vector and its divergence in the autumn months, from 23 September 1979 to 21 December 2019.

The events identified by the red dot and the cyclone Vaia, in Figure 5.5, have been numbered and inserted in the following table, in which the Q-vector and divergence values, assumed by the events, associated with the weather effects are specified:

$N°$	Date	Q-vector ($10^{-11} \frac{m^2}{kgs}$)	$\nabla \cdot$ Q ($10^{-18} \frac{m}{kgs}$)	
0	28OCT2018	1.44	-18	Sea storm Liguria (Vaia)
1	10NOV2001	1.46	-24	Sea storm Cagliari
2	3DEC2008	1.50	-24	Sea storm Puglia
3	9DEC1990	1.37	-17	Snowfall
4	11NOV2019	1.39	-18	Sea storm Liguria
5	6NOV1999	1.07	-16	Sea storm Emilia-Romagna
6	8DEC2012	1.02	-19	Sea storm Bologna-Gargano
7	22OCT2014	1.14	-15	Sea storm Sardegna Occ.
8	13NOV2017	1.21	-13	Sea storm Cagliari
9	13NOV2004	1.06	-9	Sea storm Calabria-Lampedusa
10	16NOV2019	1.16	-15	Sea storm Toscana

Table 5.1: Summary table in which the Q-vector and divergence values, assumed by events, associated with meteorological effects, are specified.

- The events are mostly associated with sea storm, which means the presence of marked baric gradients and extended wind *fetch* winds.

Looking at the Table 5.1, it is clear that there are no flood events among those selected. It is important to underline that in this study a specific in-depth analysis was not conducted for this type of event but, since large-scale flood events are typically associated with blocking situations, it is believed that they are incompatible with high Q-vector values that, in contrast, indicate fast and non-stationary dynamics.

WINTER

The 51 events that occurred from 22 December to 20 March were listed in the table in Figure 5.6, where for each event, the value of Q-vector and associated divergence and the date of occurrence was reported:

N°	Date	Q-vector $(10^{-11} \frac{m^2}{kgs})$	$\nabla \cdot Q$ $(10^{-18} \frac{m}{kgs})$	N°	Date	Q-vector $(10^{-11} \frac{m^2}{kgs})$	$\nabla \cdot Q$ $(10^{-18} \frac{m}{kgs})$
1	23/12/1979	1.20	-15	27	19/01/2005	1.15	-13
2	31/12/1979	1.09	-31	28	27/01/2005	1.19	-20
3	03/01/1980	1.16	-26	29	29/01/2005	1.38	-24
4	08/01/1981	1.36	-17	30	14/02/2005	1.34	-24
5	12/01/1981	1.02	-7	31	30/12/2005	1.07	-22
6	21/01/1981	1.07	-18	32	31/01/2006	1.06	-17
7	19/03/1981	1.15	-16	33	23/02/2006	1.05	-15
8	16/03/1983	1.02	-7	34	19/03/2007	1.11	-16
9	27/12/1983	1.22	-22	35	04/03/2008	1.16	-26
10	02/03/1984	1.07	-26	36	05/03/2008	1.08	-9
11	05/01/1985	1.18	-28	37	12/01/2009	1.12	-10
12	16/01/1985	1.32	-25	38	21/01/2009	1.32	-20
13	14/01/1987	1.22	-19	39	12/02/2010	1.06	-17
14	13/02/1987	1.21	-19	40	06/01/2012	1.04	-22
15	06/02/1991	1.00	-11	41	05/02/2012	1.38	-26
16	08/01/1994	1.05	-10	42	09/03/2012	1.07	-19
17	06/02/1994	1.17	-11	43	19/01/2013	1.04	-25
18	13/01/1995	1.01	-15	44	26/12/2013	1.08	-13
19	28/02/1995	1.00	-12	45	01/02/2014	1.05	-15
20	11/01/1996	1.16	-13	46	31/12/2014	1.18	-13
21	08/02/1996	1.16	-15	47	05/02/2015	1.14	-8
22	02/01/1999	1.33	-18	48	05/03/2015	1.47	-29
23	31/01/1999	1.23	-9	49	17/02/2016	1.61	-18
24	23/02/1999	1.02	-15	50	28/02/2016	1.16	-15
25	31/01/2003	1.31	-14	51	05/02/2019	1.22	-17
26	05/02/2003	1.14	-25				

Figure 5.6: List of events selected for the winter season (22 Dec - 20 Mar).

Frequency of the Q-vector and divergence

From the Figure 5.7 which shows the frequency distribution of the values of Q-vector, of the 51 cases subject to study, it is observed that:

- 39% of events has a Q-vector value between $(1-1.1)10^{-11}\ \frac{m^2}{kgs}$

- 29% of events has a Q-vector value between $(1.1-1.2)10^{-11}\ \frac{m^2}{kgs}$

- 12% of events has a Q-vector value between $(1.2-1.3)10^{-11}\ \frac{m^2}{kgs}$

- 16% of events has a Q-vector value between $(1.3-1.4)10^{-11}\ \frac{m^2}{kgs}$

- 2% of events has a Q-vector value between $(1.4-1.5)10^{-11}\ \frac{m^2}{kgs}$

- 0% of events has a Q-vector value between $(1.5-1.6)10^{-11}\ \frac{m^2}{kgs}$

- 2% of events has a Q-vector value between $1.6*10^{-11}\ \frac{m^2}{kgs}$

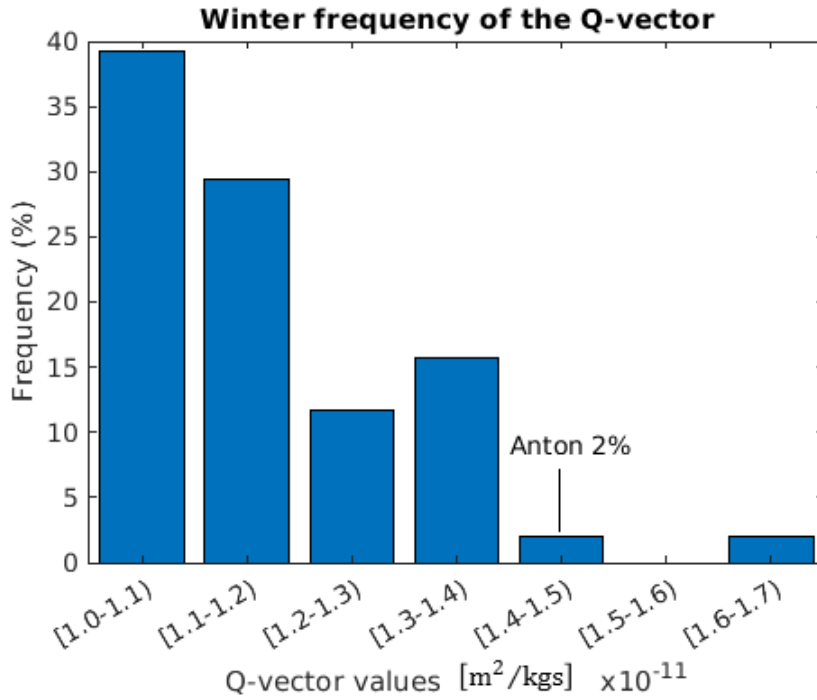Figure 5.7: Frequency of Q-vector values in the winter season from 1979 to 2020.

Also in this case, as for the autumn one, we tried to understand why there were no events in the class of Q-vector between $(1.5-1.6)10^{-11}\ \frac{m^2}{kgs}$. Analyzing the entire sample of events that occurred in that season, it was possible to observe that the events that assumed a value of Q-vector in this *range* were located on the African

continent, therefore outside the domain of interest. The Q-vector of the cyclone Anton, taken as a reference for the analysis of the winter data sample, is in the range between $(1.4 - 1.5)10^{-11}$ $\frac{m^2}{kgs}$, which includes 2% of the selected cases. This means that in 41 years only 1 event has recorded these values, indicating its rarity. In fact, the Q-vector value assumed by the cyclone Anton corresponds to the $98th$ percentile.

From the Figure (5.8), which represents the frequency distribution of the divergence values of the Q-vector, it is observed that:

- about 6% of events has a Q-vector divergence value between $-(5-8)10^{-18}$ $\frac{m}{kgs}$

- about 10% of events has a Q-vector divergence value between $-(8-11)10^{-18}$ $\frac{m}{kgs}$

- about 12% of events has a Q-vector divergence value between $-(11-14)10^{-18}$ $\frac{m}{kgs}$

- about 23% of events has a Q-vector divergence value between $-(14-17)10^{-18}$ $\frac{m}{kgs}$

- about 17% of events has a Q-vector divergence value between $-(17-20)10^{-18}$ $\frac{m}{kgs}$

- about 8% of events has a Q-vector divergence value between $-(20-23)10^{-18}$ $\frac{m}{kgs}$

- about 14% of events has a Q-vector divergence value between $-(23-26)10^{-18}$ $\frac{m}{kgs}$

- about 8% of events has a Q-vector divergence value between $-(26-29)10^{-18}$ $\frac{m}{kgs}$

- about 2% of events has a Q-vector divergence value between $-29*10^{-18}$ $\frac{m}{kgs}$

The divergence of the Q-vector associated with Anton falls within the class of values between $-(26-29)10^{-18}$ $\frac{m}{kgs}$ populated only by the 8% of cases: this means that values of this order of magnitude have been observed other 4 times in the past 41 years; the divergence value assumed by the cyclone Anton corresponds to the $98th$ percentile. So in this case, it can be said that the cyclone Anton, since it belongs to the $98th$ percentile for both the Q-vector and divergence values, was a rare event.
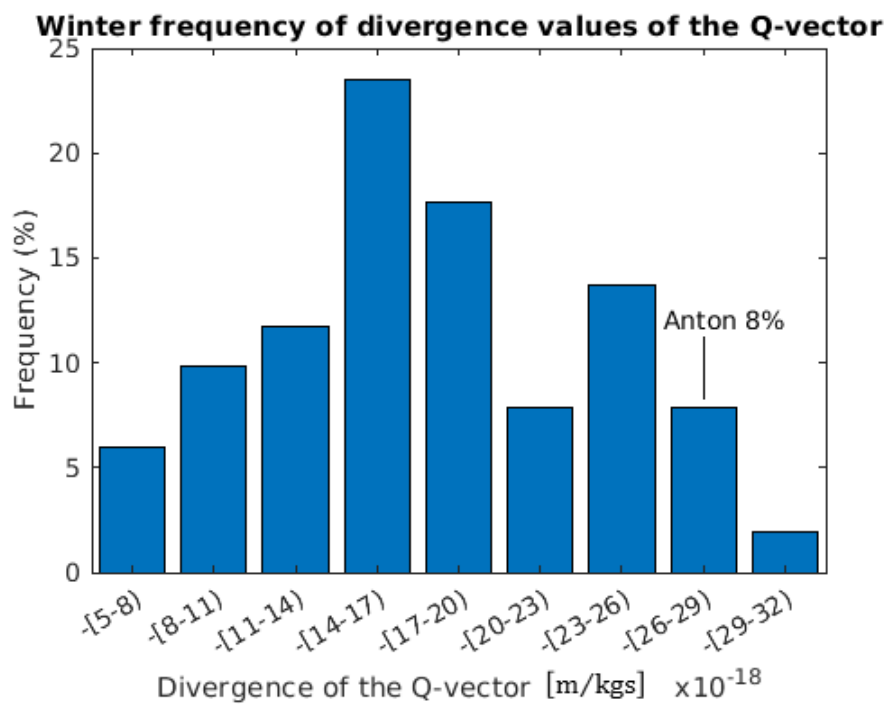
Figure 5.8: Frequency of Q-vector divergence values in the winter season from 1979 to 2020.

Correlation between Q-vector and divergence of the winter season

The correlation between Q-vector and the divergence of Q-vector for the winter season has been reported in Figure 5.9.

Looking at Figure 5.9, the entire sample of winter events turns out to be divided into three groups; one more populated - precisely made up of 41 events - (left), with Q-vector values between $(1-1.3)*10^{-11} \frac{m^2}{kgs}$ and divergence between $-(6-31)*10^{-18} \frac{m}{kgs}$, a central one consisting of 8 events with Q-vector values between $(1.3-1.4)*10^{-11} \frac{m^2}{kgs}$ and divergence between $-(14-26)*10^{-18} \frac{m}{kgs}$ and finally one on the right, with only 2 events with a Q-vector greater than $1.45*10^{-11} \frac{m^2}{kgs}$ and with divergence values in the range $-(18-29)*10^{-18} \frac{m}{kgs}$. For the winter season, as for the autumn season, documentation was sought relating to the meteorological phenomena associated with these events and the consequent effects on the ground, but also in this case information was found only for a subset of events, indicated in the graph by the red dot in Figure 5.9 and by the blue box with which the cyclone Anton is indicated.
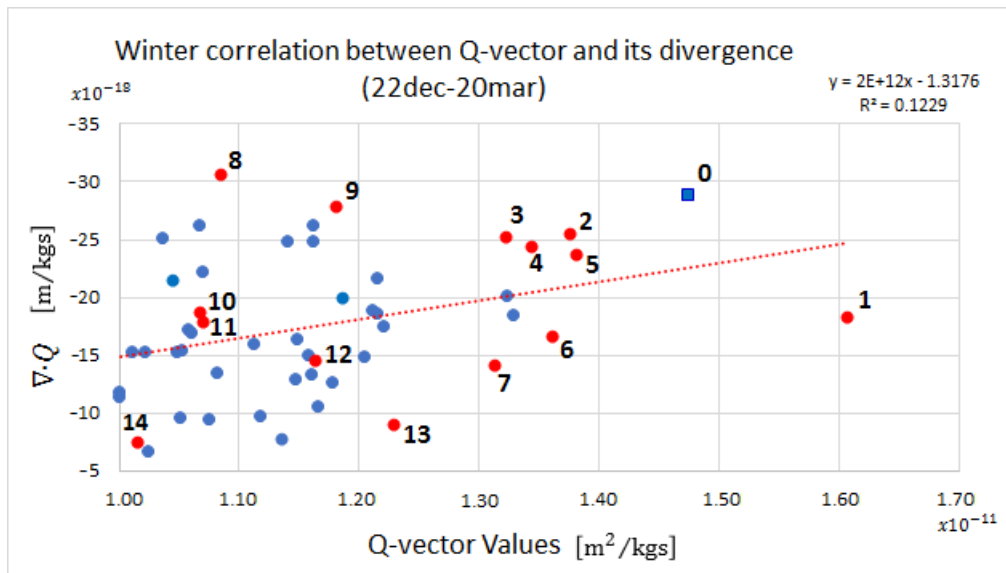

Figure 5.9: Correlation between Q-vector and divergence of Q-vector in the winter months from 22 December 1979 to 20 March 2020.

The red dots and the cyclone Anton, in Figure 5.9 have been numbered and inserted in the following table, which specifies the Q-vector and divergence values, assumed by the events, associated with the relevant meteorological phenomena associated with them:

$N°$	Date	Q-vector ($10^{-11} \frac{m^2}{kgs}$)	$\nabla \cdot$ Q ($10^{-18} \frac{m}{kgs}$)	
0	5MAR2015	1.47	-29	Sea storm Rimini (Anton)
1	17FEB2016	1.61	-18	Sea storm Calabria
2	5FEB2012	1.38	-25	Snowfall Emilia-Romagna (Rimini)
3	16JAN1985	1.32	-25	Snowfall Lombardia (Milano)
4	14FEB2005	1.34	-24	Snowfall San Benedetto del Tronto
5	29JAN2005	1.38	-24	Snowfall Italia centro-meridionale
6	8JAN1981	1.36	-17	Snowfall Sicilia-Calabria
7	31JAN2003	1.14	-31	Snowfall Lazio
8	31DEC1979	1.09	-31	Sea storm Puglia
9	5JAN1985	1.18	-28	Snowfall Africa-Italia
10	9MAR2012	1.07	-19	Sea storm Sicilia
11	21JAN1981	1.07	-18	Sea storm Sicilia
12	28FEB2016	1.16	-15	Sea storm Napoli
13	31JAN1999	1.23	-9	Snowfall Messina
14	12JAN1981	1.02	-7	Snowfall Verona

Table 5.2: Summary table in which the Q-vector and divergence values, assumed by the events, associated with the meteorological effects are specified.

From the information collected it can be concluded that:

- The *cluster* located on the left, populated by most events, is characterized by both storms and snowfalls.

- 6 of the 8 events, in the central *cluster*, documentation of which was found, were snow episodes.

- The *cluster* to the right, the one that moves away from the average statistics, consisting of only 2 events, includes fall events associated with sea storm.

17 February 2016 is largely outside of the winter event statistics, however no information has been found on devastating effects comparable to those caused by cyclone Vaia.

Comparison of the temporal evolution of the Q-vector values and divergence between the autumn and winter seasons

Looking from a general point of view, Figure 5.10, which shows the trend of the maximum values of Q-vector for the autumn season, shows a random temporal trend that would seem not to provide useful information. However, the trend line shows a temporal increase in the number of events with higher Q-vector values. The arithmetic mean of the Q-vector values is $1.16 * 10^{-11} \frac{m^2}{kgs}$ where most events have a Q-vector value in the range $(1 - 1.25) * 10^{-11} \frac{m^2}{Kgs}$ while the presence of only 5 cyclones which show a much higher Q-vector value is observed. Also Vaia belongs to this group; the first four occurred one every about 10 years, while the last (11/11/2019) only one year after the cyclone Vaia. The study therefore leads us to say that, starting from the late 70s to the present day, an event occurred with Q-vector $\geq 1.30 * 10^{-11} \frac{m^2}{kgs}$ with a recurrence of about 10 years until the year 2018. It is also observed that in the last two years two close events have been observed characterized by high Q-vector values.

For the winter season, looking at Figure 5.11, the average of the Q-vectors for the winter season is $1.16 * 10^{-11} \frac{m^2}{kgs}$, but in comparison to the values reached in the autumn season, the number of cyclones having Q-vector values in the range up to $1.4 * 10^{-11} \frac{m^2}{kgs}$ and only two events that occurred in 2015 showed greater values than this. These two events are the cyclone Anton (5/03/2015) and the cyclone of 5/2/2015.

Therefore, from the comparison between the values of Q-vector assumed in the two seasons it can be summarized that:

- In the autumn season most intense cyclones take a Q-vector value up to the value $1.25 * 10^{-11} \frac{m^2}{kgs}$ and about every 10 years there is an overcoming.

- In the winter season, however, most events take on a Q-vector value of up to $1.40 * 10^{-11} \frac{m^2}{kgs}$ while, only in 2015, there was a case exceeding this value reaching $1.6 * 10^{-11} \frac{m^2}{kgs}$.

It can also be said that there is a greater probability of having events with Q-vector values greater than $1.4 * 10^{-11} \frac{m^2}{kgs}$ in the autumn season than in the winter season.

As for the seasonal comparison of the temporal distribution of the divergence of the Q-vector (Figures 5.12 and 5.13) the only information that can be obtained is that: in the autumn season the value of $-25 * 10^{-18} \frac{m}{kgs}$ is never passed, except for two event; on the other hand, in the winter season it is more frequent to exceed this value.

Figure 5.10: Temporal evolution of the Q-vector values of the 39 cases selected for the autumn season.
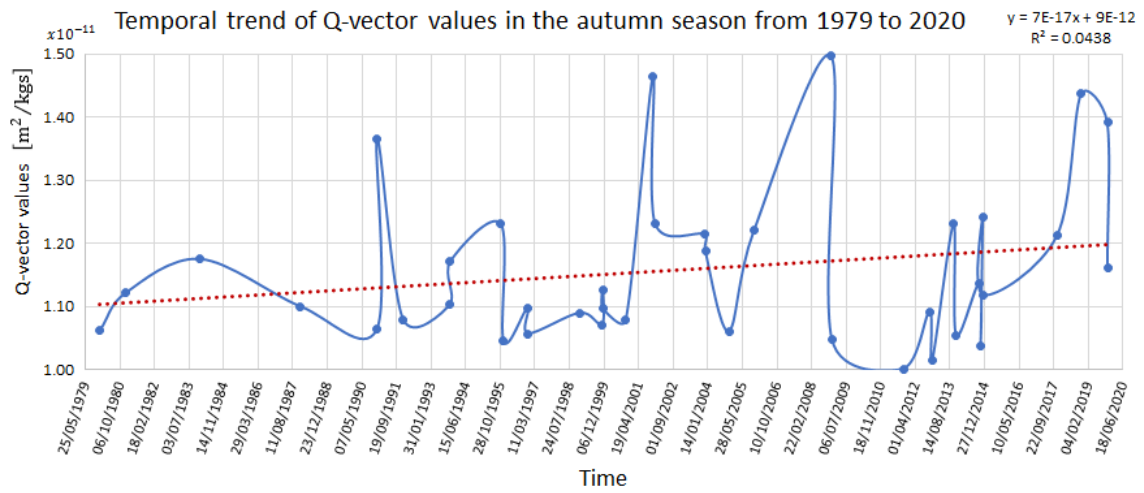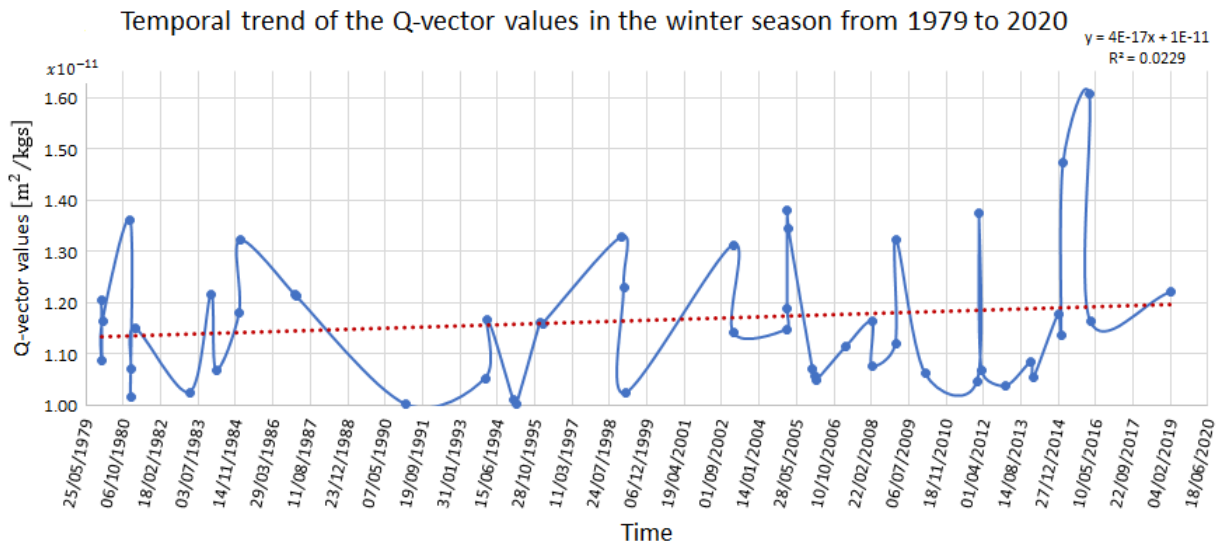

Figure 5.11: Temporal evolution of the Q-vector values of the 51 cases selected for the winter season.
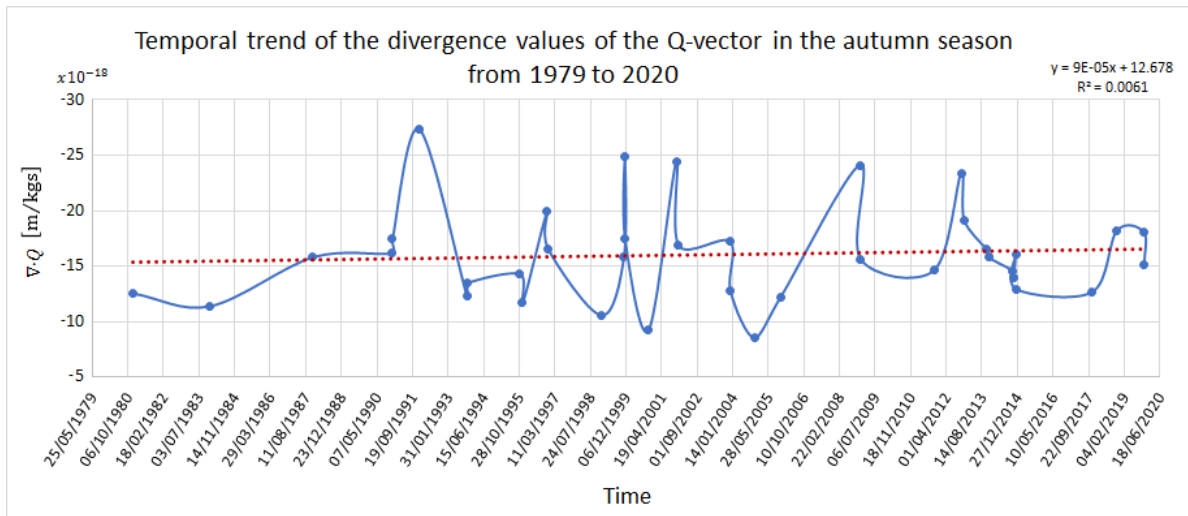
Figure 5.12: Temporal evolution of the divergence values of the Q-vector of the 39 cases selected for the autumn season.
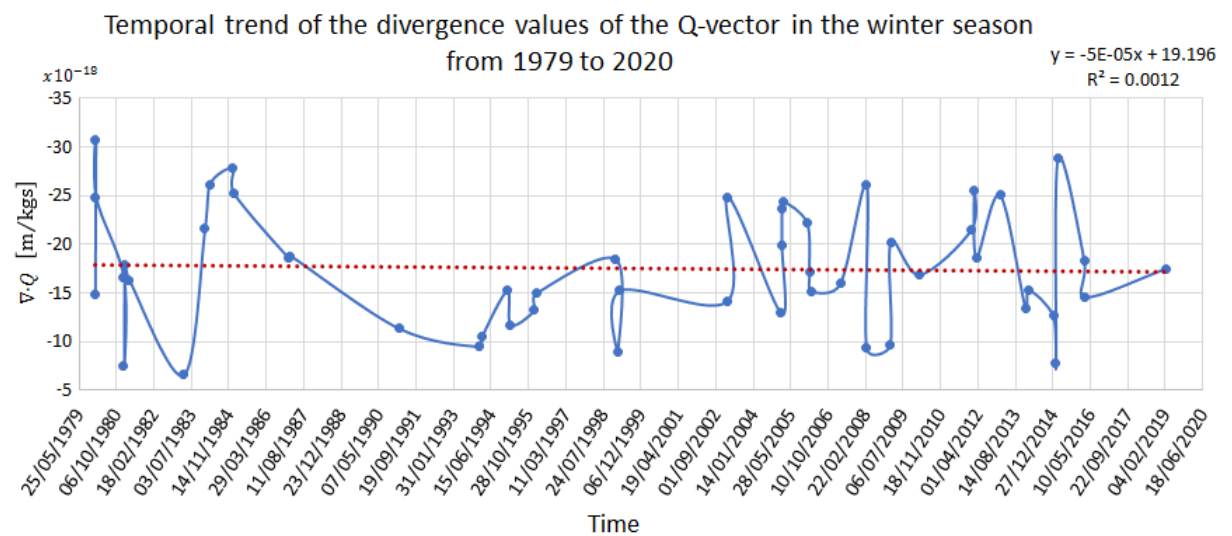

Figure 5.13: Temporal evolution of the divergence values of the Q-vector of the 51 cases selected for the winter season.

Conclusions

The purpose of this chapter was to evaluate the exceptional nature of Vaia and the seasonality of the baroclinic cyclones. The following conclusions can be drawn from the analyses conducted:

Autumn season Low frequency of events with Q-vector values similar to Vaia, between $(1.4 - 1.5)10^{-11} \ \frac{m^2}{kgs}$, while the divergence values of Vaia's Q-vector are above the average. Vaia falls into the $95th$ and the $80th$ percentile for the Q-vector and divergence values respectively. Analyzing the correlation between the Q-vector and divergence, which is not good, Vaia appears distinct from the rest of the statistical cases, as shown in Figure 5.5, where the 39 events are divided into two groups; one more populated, with Q-vector values less than $1.30 * 10^{-11} \ \frac{m^2}{kgs}$ and divergence in the range $-(8 - 28) * 10^{-18} \ \frac{m}{kgs}$ and one on the right, with only 5 events, including Vaia, with a Q-vector greater than $1.30*10^{-11} \ \frac{m^2}{kgs}$ and with divergence values in the range $-(17 - 25) * 10^{-18} \ \frac{m}{kgs}$.

Winter season Low frequency of events that assume values similar to the cyclone Anton, more precisely where the Q-vector is in the range $(1.4 - 1.5)10^{-11} \ \frac{m^2}{kgs}$ and divergence values in the range $-(26 - 29)10^{-18} \ \frac{m}{kgs}$: for both variables, cyclone Anton ranks at the $98th$ percentile. From the Figure 5.9, the correlation between Q-vector and divergence, that even for this season is not good, highlights the subdivision of the entire sample population into three groups in which Anton falls into the one more distant from the average statistics and the least populated.

The attention of the whole thesis is focused on the Vaia storm but unfortunately there is no clear answer to confirm its exceptionality and rarity in terms of Q-vector. However, the cyclone belongs to explosive cyclogenesis, which can make it classified among the most intense cyclones. It is recognized as exceptional for the damage it has caused on a large scale (in Liguria, Trentino Alto Adige, Friuli Venezia Giulia and Veneto) and for the strong winds that have been recorded. It has been difficult to obtain confirmation from the Q-vector statistics which however seems to give perception of the rarity of this event.
In this study, the variable used for selection, as already explained, is the Q-vector. Its maximum value is associated with a divergence value, which does not occur at the same time as the maximum of Q-vector for all cyclones, unlike what happens for the Vaia cyclone.
Is this feature that makes Vaia's power unique?
Given the availability of adequate documentation on the ground effects of the selected events, it would be interesting to compare the cases in which Q-vector and divergence are simultaneously maxima with those in which the two maxima are not synchronous.
Below are some photos of the Vaia storm, of 29 October 2018.

Figure 5.14: Rapallo seafront (Liguria).

Figure 5.15: Rapallo seafront (Liguria).

Figure 5.16: Dolomite forests shot down by Vaia.

Conclusions

The Q-vector is the mathematical tool used to conduct the present study on the Vaia storm, that is recognized to have been exceptional for the damage it has caused on a large scale (in Liguria, Trentino Alto Adige, Friuli Venezia Giulia and Veneto) and for the strong winds that have been recorded. This tool is widely used in operational centers, especially abroad. The first part of the thesis focused on the understanding of the response and the information obtainable from the Q-vector values in different cyclonic events. Subsequently, analysis was carried out to understand the explosive nature of the cyclone Vaia through the use of sensitivity tests applied to numerical simulations performed with the MOLOCH limited area model. Finally, the Q-vector values in the cyclone Vaia was investigated in the framework of the climatology of Mediterranean cyclones.

From the comparison among the cyclone Vaia with other cyclones the results obtained are:

- The order of magnitude assumed by the Q-vector in the Vaia storm is 10^{-11} $\frac{m^2}{kgs}$.

- The Q-vector reaches high values, of the order of magnitude 10^{-11} $\frac{m^2}{kgs}$, only in cases of intense baroclinic cyclones and is much smaller in the presence of barotropic cyclones.

- The convergence values of Q-vector during the cyclone Vaia was only slightly above average.

- In all the studied cases, except from Vaia, the Q-vector reaches the maximum (order of magnitude 10^{-11} $\frac{m^2}{kgs}$) when the surface low has already formed. Only in the case of Vaia the maximum Q-vector value occurs few hours before the cyclone development, suggesting favorable conditions to the intensification of frontal structures independently of the presence of the cyclone.

From the sensitivity experiments, used to understand which physical processes contributed most to the development of the cyclone Vaia, the following pieces of information are obtained: in the first phase of cyclone development, the contribution of heat fluxes from the sea was significant, while in the second phase the contribution of humidity transported by the *atmospheric river* was of fundamental importance, which contributed, in a remarkable way, to the deepening of the cyclone Vaia.

Finally, from the statistical analysis conducted to understand how Vaia fits into the

climatology of Mediterranean cyclones in terms of Q-vector values, it was found that: both in autumn and winter, events with Q-vector values comparable to Vaia, between $(1.4 - 1.5)10^{-11} \frac{m^2}{kgs}$ are unusual. Vaia falls respectively above the $95th$ and the $80th$ percentile for the Q-vector intensity and for the divergence values in comparison with the other autumn cyclones, confirming the hypothesis that it was a rare event.

It can be concluded that, for what concerns the values of the Q-vector, Vaia had high values, comparable only to a few other cyclones, such as Anton. Both are far from the statistical average, and therefore can be considered rare events.

Appendix   A

The equation (2.1) can be approximated to the first order of Rossby $O(Ro)$, therefore the terms of order higher than the first are removed, as shown below:

$$
\left.
\begin{aligned}
\frac{D(u_g + u_a)}{Dt} &= \frac{\partial u_g}{\partial t} + \cancel{\frac{\partial u_a}{\partial t}} + (u_g + u_a)\frac{\partial}{\partial x}(u_g + u_a) + (v_g + v_a)\frac{\partial}{\partial y}(u_g + u_a) + \omega\cancel{\frac{\partial}{\partial p}u_g} + \omega\cancel{\frac{\partial}{\partial p}u_a} \\
&= \frac{\partial u_g}{\partial t} + u_g\frac{\partial u_g}{\partial x} + u_g\cancel{\frac{\partial u_g}{\partial x}} + u_g\cancel{\frac{\partial u_a}{\partial x}} + u_a\cancel{\frac{\partial u_a}{\partial x}} + v_g\frac{\partial u_g}{\partial y} + v_g\cancel{\frac{\partial u_g}{\partial y}} + v_g\cancel{\frac{\partial u_a}{\partial y}} + v_a\cancel{\frac{\partial u_a}{\partial y}} \\
&= \frac{\partial u_g}{\partial t} + u_g\frac{\partial u_g}{\partial x} + u_g\frac{\partial u_g}{\partial y} \\
\frac{D(v_g + v_a)}{Dt} &= \frac{\partial v_g}{\partial t} + \cancel{\frac{\partial v_a}{\partial t}} + (u_g + u_a)\frac{\partial}{\partial x}(v_g + v_a) + (v_g + v_a)\frac{\partial}{\partial y}(v_g + v_a) + \omega\cancel{\frac{\partial}{\partial p}v_g} + \omega\cancel{\frac{\partial}{\partial p}v_a} \\
&= \frac{\partial v_g}{\partial t} + u_g\frac{\partial v_g}{\partial x} + u_g\cancel{\frac{\partial v_g}{\partial x}} + u_g\cancel{\frac{\partial v_a}{\partial x}} + u_a\cancel{\frac{\partial v_a}{\partial x}} + v_g\frac{\partial v_g}{\partial y} + v_a\cancel{\frac{\partial v_g}{\partial y}} + v_g\cancel{\frac{\partial v_a}{\partial y}} + v_a\cancel{\frac{\partial v_a}{\partial y}} \\
&= \frac{\partial v_g}{\partial t} + v_g\frac{\partial v_g}{\partial x} + v_g\frac{\partial v_g}{\partial y}
\end{aligned}
\right\} \simeq \frac{D_g\vec{V}_g}{Dt}
$$

$$
\begin{aligned}
f\hat{k} \times \vec{V} + \nabla\phi &= (f_0 + \beta y)\hat{k} \times (\vec{V}_g + \vec{V}_a) - f_0\hat{k} \times \vec{V}_g \\
&= \cancel{f_0\hat{k} \times \vec{V}_g} + f_0\hat{k} \times \vec{V}_a + \beta y\hat{k} \times \vec{V}_g + \beta y\hat{k} \times \vec{V}_a - \cancel{f_0\hat{k} \times \vec{V}_g} \\
&= f_0\hat{k} \times \vec{V}_a + \beta y\hat{k} \times \vec{V}_g + \beta y\hat{k} \times \vec{V}_a \\
&\simeq f_0\hat{k} \times \vec{V}_a + \beta y\hat{k} \times \vec{V}_g
\end{aligned}
$$

Finally, by replacing:

$$
\frac{D_g\vec{V}_g}{Dt} = -f_0\hat{k} \times \vec{V}_a - \beta y\hat{k} \times \vec{V}_g \tag{5.1}
$$

Appendix   B

Proof of the equation (2.6):

$$\frac{D_g T}{Dt} - S_p \omega - \frac{J}{c_p} = 0$$

We start from the equation of state for perfect gases:

$$p\alpha = RT \qquad (5.2)$$

The total derivative applies

$$p\frac{D\alpha}{Dt} = R\frac{DT}{Dt} - \alpha\frac{Dp}{Dt} \qquad (5.3)$$

Using it in the thermodynamic energy equation:

$$c_v\frac{DT}{Dt} + p\frac{D\alpha}{Dt} = J \qquad (5.4)$$

equation 5.3 becomes

$$c_v\frac{DT}{Dt} + R\frac{DT}{Dt} - \alpha\frac{Dp}{Dt} = J \qquad (5.5)$$

using the relationship $c_p = c_v + R$

$$c_p\frac{DT}{Dt} - \alpha\frac{Dp}{Dt} = J \qquad (5.6)$$

In isobaric coordinates:

$$\frac{Dp}{Dt} = \omega \qquad (5.7)$$

$$\frac{D}{Dt} = \frac{\partial}{\partial t} + u\frac{\partial}{\partial x} + v\frac{\partial}{\partial v} + \omega\frac{\partial}{\partial p} \qquad (5.8)$$

then,

$$\frac{\partial T}{\partial t} + u\frac{\partial T}{\partial x} + v\frac{\partial T}{\partial v} + \omega\frac{\partial T}{\partial p} - \frac{\alpha\omega}{c_p} = \frac{J}{c_p} \qquad (5.9)$$

$$(\frac{\partial T}{\partial t} + u\frac{\partial T}{\partial x} + v\frac{\partial T}{\partial v}) - S_p\omega = \frac{J}{c_p} \qquad (5.10)$$

where $S_p = \frac{\alpha}{c_p} - \frac{\partial T}{\partial p}$ and from $\vec{V} = \vec{v_g} + \vec{v_a} \approx \vec{v_g}$ finally we get:

$$\frac{D_g T}{Dt} - S_p\omega - \frac{J}{c_p} = 0$$

Appendix   C

For the horizontal y-component of the Q-vector, $p\frac{\partial}{\partial p}(2.4) - (\frac{R}{f_0})\frac{\partial}{\partial y}(2.6)$:

$$p\frac{\partial}{\partial p}[\frac{\partial u_g}{\partial t} + u_g\frac{\partial u_g}{\partial x} + v_g\frac{\partial u_g}{\partial x} - f_0 v_a - \beta y v_g] - \frac{R}{f_0}\frac{\partial}{\partial y}[\frac{\partial T}{\partial t} + u_g\frac{\partial T}{\partial x} + v_g\frac{\partial T}{\partial y} - S_p\omega - \frac{J}{c_p}] = 0$$

$$\frac{R}{f_0}S_p\frac{\partial\omega}{\partial y} - pf_0\frac{\partial v_a}{\partial p} - \beta y p\frac{\partial v_g}{\partial p} + \frac{R}{c_p f_0}\frac{\partial J}{\partial y} = -(\frac{\partial}{\partial t} + u_g\frac{\partial}{\partial x} + v_g\frac{\partial}{\partial y})(p\frac{\partial u_g}{\partial p} - \frac{R}{f_0}\frac{\partial T}{\partial y})$$
$$- p[\frac{\partial u_g}{\partial p}\frac{\partial u_g}{\partial x} + \frac{\partial v_g}{\partial p}\frac{\partial u_g}{\partial y}]$$
$$+ \frac{R}{f_0}[\frac{\partial u_g}{\partial y}\frac{\partial T}{\partial x} + \frac{\partial v_g}{\partial y}\frac{\partial T}{\partial y}]$$
$$(5.11)$$

We suppose Sp nearly constant.
Using the equation of the *thermal wind*, whose components are:

$$p\frac{\partial u_g}{\partial p} = \frac{R}{f_0}\frac{\partial T}{\partial y} \tag{5.12}$$

$$p\frac{\partial v_g}{\partial p} = -\frac{R}{f_0}\frac{\partial T}{\partial x} \tag{5.13}$$

the first term on the right hand side of the equation (5.11) is deleted and the second becomes:

$$-p[\frac{\partial u_g}{\partial p}\frac{\partial u_g}{\partial x} + \frac{\partial v_g}{\partial p}\frac{\partial u_g}{\partial y}] = -\frac{R}{f_0}[\frac{\partial T}{\partial y}\frac{\partial u_g}{\partial x} - \frac{\partial T}{\partial x}\frac{\partial u_g}{\partial y}]$$

Substituting it into the equation (5.11) and multiplying by $\frac{f_0}{p}$:

$$\frac{R}{p}S_p\frac{\partial\omega}{\partial y} - f_0^2\frac{\partial v_a}{\partial p} - \beta f_0 y\frac{\partial v_g}{\partial p} = -\frac{R}{p}[\frac{\partial T}{\partial y}\frac{\partial u_g}{\partial x} - \frac{\partial T}{\partial x}\frac{\partial u_g}{\partial y}] + \frac{R}{p}[\frac{\partial u_g}{\partial y}\frac{\partial T}{\partial x} + \frac{\partial v_g}{\partial y}\frac{\partial T}{\partial y}] - \frac{R}{pc_p}\frac{\partial J}{\partial y}$$
$$(5.14)$$

Knowing that $\nabla \cdot \vec{V}_g = 0$, the equation (5.14) becomes:

$$\frac{R}{p}S_p\frac{\partial\omega}{\partial y} - f_0^2\frac{\partial v_a}{\partial p} - \beta f_0 y\frac{\partial v_g}{\partial p} = +2\frac{R}{p}\frac{\partial T}{\partial y}\frac{\partial v_g}{\partial y} + 2\frac{R}{p}\frac{\partial T}{\partial x}\frac{\partial u_g}{\partial y} - \frac{R}{pc_p}\frac{\partial J}{\partial y}$$

By placing $\sigma = \frac{RS_p}{p}$:

$$\sigma\frac{\partial\omega}{\partial y} - f_0^2\frac{\partial v_a}{\partial p} - \beta f_0 y\frac{\partial v_g}{\partial p} = -2Q_y - \frac{R}{pc_p}\frac{\partial J}{\partial y} \tag{5.15}$$

where

$$Q_y = -\frac{R}{p}[\frac{\partial u_g}{\partial y}\frac{\partial T}{\partial x} + \frac{\partial v_g}{\partial y}\frac{\partial T}{\partial y}] \tag{5.16}$$

For the horizontal x-component, $p\frac{\partial}{\partial p}(2.5) + (\frac{R}{f_0})\frac{\partial}{\partial x}(2.6)$:

$$p\frac{\partial}{\partial p}[\frac{\partial v_g}{\partial t} + u_g\frac{\partial v_g}{\partial x} + v_g\frac{\partial v_g}{\partial y} + f_0 u_a + \beta y u_g] + \frac{R}{f_0}\frac{\partial}{\partial x}[\frac{\partial T}{\partial t} + u_g\frac{\partial T}{\partial x} + v_g\frac{\partial T}{\partial y} - S_p\omega - \frac{J}{c_p}] = 0$$

$$pf_0\frac{\partial u_a}{\partial p} - \frac{R}{f_0}S_p\frac{\partial \omega}{\partial x} + \beta yp\frac{\partial u_g}{\partial p} - \frac{R}{c_p f_0}\frac{\partial J}{\partial x} = -(\frac{\partial}{\partial t} + u_g\frac{\partial}{\partial x} + v_g\frac{\partial}{\partial y})(p\frac{\partial v_g}{\partial p} + \frac{R}{f_0}\frac{\partial T}{\partial x})$$
$$- p[\frac{\partial u_g}{\partial p}\frac{\partial v_g}{\partial x} + \frac{\partial v_g}{\partial p}\frac{\partial v_g}{\partial y}]$$
$$- \frac{R}{f_0}[\frac{\partial u_g}{\partial x}\frac{\partial T}{\partial x} + \frac{\partial v_g}{\partial x}\frac{\partial T}{\partial y}]$$

$$\tag{5.17}$$

Using the equations (5.12) and (5.13), the first term to the right of the equation (5.17) is deleted and the second becomes:

$$-p[\frac{\partial u_g}{\partial p}\frac{\partial v_g}{\partial x} + \frac{\partial v_g}{\partial p}\frac{\partial v_g}{\partial y}] = -\frac{R}{f_0}[\frac{\partial T}{\partial y}\frac{\partial v_g}{\partial x} - \frac{\partial T}{\partial x}\frac{\partial v_g}{\partial y}]$$

Substituting in the equation (5.17) and multiplying by $\frac{f_o}{p}$, the latter becomes:

$$-\frac{R}{p}S_p\frac{\partial \omega}{\partial x} + f_0^2\frac{\partial u_a}{\partial p} + \beta yf_0\frac{\partial u_g}{\partial p} = -\frac{R}{p}[\frac{\partial T}{\partial y}\frac{\partial v_g}{\partial x} - \frac{\partial T}{\partial x}\frac{\partial v_g}{\partial y}] - \frac{R}{p}[\frac{\partial u_g}{\partial x}\frac{\partial T}{\partial x} + \frac{\partial v_g}{\partial x}\frac{\partial T}{\partial y}] + \frac{R}{c_p p}f_0\frac{\partial J}{\partial x}$$
$$\tag{5.18}$$

Knowing that $\nabla \cdot \vec{V}_g = 0$ and changing all signs the equation 5.18 we have:

$$\frac{R}{p}S_p\frac{\partial \omega}{\partial x} - f_0^2\frac{\partial v_a}{\partial p} - \beta yf_0\frac{\partial u_g}{\partial p} = +2\frac{R}{p}\frac{\partial T}{\partial y}\frac{\partial v_g}{\partial x} + 2\frac{R}{p}\frac{\partial T}{\partial x}\frac{\partial u_g}{\partial x} - \frac{R}{c_p p}f_0\frac{\partial J}{\partial x}$$

and therefore:

$$\sigma\frac{\partial \omega}{\partial x} - f_0^2\frac{\partial v_a}{\partial p} - \beta yf_0\frac{\partial u_g}{\partial p} = -2Q_x - \frac{R}{c_p p}f_0\frac{\partial J}{\partial x} \tag{5.19}$$

where

$$Q_x = -\frac{R}{p}[\frac{\partial v_g}{\partial x}\frac{\partial T}{\partial y} + \frac{\partial u_g}{\partial x}\frac{\partial T}{\partial x}] \tag{5.20}$$

108

Appendix   D

Omega equation

The definition of the Q-vector allows to rewrite the so called *omega equation* in terms of Q-vector. We proceed by carrying out $\frac{\partial}{\partial x}(5.19) + \frac{\partial}{\partial y}(5.15)$

$$\sigma\frac{\partial}{\partial x}[\frac{\partial \omega}{\partial x}] - f_0^2\frac{\partial}{\partial x}[\frac{\partial u_a}{\partial p}] - f_0\beta y\frac{\partial}{\partial x}[\frac{\partial u_g}{\partial p}] + 2\frac{\partial Q_x}{\partial x} + \frac{k}{p}\frac{\partial^2 J}{\partial x^2} +$$

$$\sigma\frac{\partial}{\partial y}[\frac{\partial \omega}{\partial y}] - f_0^2\frac{\partial}{\partial y}[\frac{\partial v_a}{\partial p}] - f_0\beta y\frac{\partial}{\partial y}[\frac{\partial v_g}{\partial p}] + 2\frac{\partial Q_y}{\partial y} + \frac{k}{p}\frac{\partial^2 J}{\partial y^2} = 0 \quad (5.21)$$

where $k = \frac{R}{c_p}$.
Using the continuity equation in isobaric coordinates,

$$\frac{\partial u_a}{\partial x} + \frac{\partial v_a}{\partial y} + \frac{\partial \omega}{\partial p} = 0 \tag{5.22}$$

to eliminate the components of the ageostrophic wind and considering that $\nabla \cdot \vec{V}_g = 0$ you have:

$$\sigma\nabla^2\omega - f_0^2\frac{\partial^2\omega}{\partial p^2} = -2\nabla \cdot \vec{Q} - f_0\beta\frac{\partial v_g}{\partial p} - \frac{k}{p}\nabla^2 J \tag{5.23}$$

Appendix E

Thus, we let $\phi(x, y, z, t) = \frac{(p - p_0)}{\rho_0}$ dove ϕ designate the pressure deviation normalized by density and $\Theta = \theta - \theta_0$ designate the potential temperature deviation where $p_0(z)$ e $\theta_0(z)$ are the height-dependent standard atmosphere values of pressure and potential temperature, respectively.

With the above definitions, the horizontal momentum equations, thermodynamic energy equation, hydrostatic approximation, and continuity equation become:

$$\frac{Du}{Dt} - fv + \frac{\partial \phi}{\partial x} = 0 \tag{5.24}$$

$$\frac{Dv}{Dt} + fu + \frac{\partial \phi}{\partial y} = 0 \tag{5.25}$$

$$\frac{D\Theta}{Dt} + w\frac{d\theta_0}{dz} = 0 \tag{5.26}$$

$$b \equiv \frac{g\Theta}{\theta_{00}} = \frac{\partial \phi}{\partial z} \tag{5.27}$$

$$\frac{\partial u}{\partial x} + \frac{\partial v}{\partial y} + \frac{\partial w}{\partial z} = 0 \tag{5.28}$$

where b is the buoyancy, θ_{00} is a constant reference value of potential temperature, and

$$\frac{D}{Dt} = \frac{\partial}{\partial t} + u\frac{\partial}{\partial x} + v\frac{\partial}{\partial y} + w\frac{\partial}{\partial z} \tag{5.29}$$

As a first approximation we can model fronts as two-dimensional structures. For convenience we choose a coordinate system in which the front is stationary and take the cross-frontal direction to be parallel to the y axis. Then $L_x \gg L_y$, where L_x and L_y designate the along-front and cross-front lenght scales. Similarly, from continuity equation, $U \gg V$ where U and V, respectively, design the along-front and cross-front velocity scales. The Figure 5.17 shows these scales relative to the front.
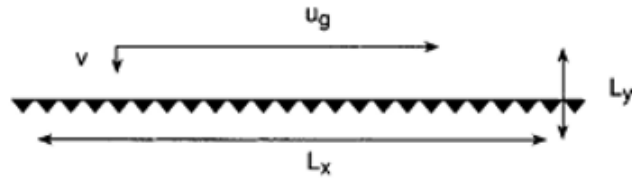

Figure 5.17: Velocity and length scales for a front parallel to the x-axis [13].

Letting $U \sim 10\frac{m}{s}$, $V \sim 1\frac{m}{s}$, $L_x \sim 1000$ Km and $L_y \sim 100$ Km, we find that it is possible to utilize the differing scales of the along-front and cross-front motion to

simplify the dynamics.

Assuming that $\frac{D}{Dt} \sim \frac{V}{L_y}$ (the cross-front advection time scale) and defining a Rossby number, $R_o = \frac{V}{fL_y} \ll 1$, the magnitude of the ratios of the inertial and Coriolis terms in the x and y components of the momentum equation can be expressed as

$$\frac{|Du/Dt|}{|fv|} \sim \frac{UV/L_y}{fV} \sim R_0\Big(\frac{U}{V}\Big) \sim 1 \tag{5.30}$$

$$\frac{|Dv/Dt|}{|fu|} \sim \frac{V^2/L_y}{fU} \sim R_0\Big(\frac{U}{V}\Big) \sim 10^{-2} \tag{5.31}$$

The velocity along the front is in geostrophic equilibrium while the front velocity direction perpendicular to the front, which is the direction of motion of the front (equation (5.31))) is not.

Therefore, if the components of the geostrophic wind are defined by:

$$fu_g = -\frac{\partial \phi}{\partial y} \tag{5.32}$$

$$fv_g = \frac{\partial \phi}{\partial x} \tag{5.33}$$

and separating the horizontal velocity field into geostrophic and ageostrophic parts, with a good approximation $u = u_g$, but $v = v_g + v_a$, where v_g and v_a they are of the same order of magnitude.

The x component of the horizontal motion equation (5.24), the thermodynamic energy equation (5.26) and the continuity equation (5.28) for frontal scaling can therefore be expressed as:

$$\frac{Du_g}{Dt} - fv_a = 0 \tag{5.34}$$

$$\frac{Db}{Dt} + wN^2 = 0 \tag{5.35}$$

$$\frac{\partial v_a}{\partial y} + \frac{\partial w}{\partial z} = 0 \tag{5.36}$$

The equation (5.35) is obtained using the equation (5.27) to replace Θ with b in the equation (5.26), and N is the defined Brunt-Vaisala frequency in terms of potential temperature such as:

$$N^2 \equiv \frac{g}{\theta_{00}} \frac{\partial \theta_0}{\partial z} \tag{5.37}$$

Since the velocity along the front is in geostrophic equilibrium, u_g and b are correlated by the relation of the thermal wind:

$$f\frac{\partial u_g}{\partial z} = -\frac{\partial b}{\partial y} \tag{5.38}$$

Note that the equations (5.34) and (5.35) differ from their quasi-geostrophic analogues; although the zonal motion is still approximately geostrophic and the advection parallel to the front is geostrophic, the advection of the motion and temperature perpendicular to the front are due not only to the geostrophic wind, but to the ageostrophic circulation (v_a, w):

$$\frac{D}{Dt} = \frac{D_g}{Dt} + \left(v_a \frac{\partial}{\partial y} + w \frac{\partial}{\partial z}\right) \tag{5.39}$$

where D_g/Dt was defined in (APPENDIX A).

The substitution of momentum with its geostrophic value in (5.34) is indicated as an approximation of the geostrophic momentum, and the resulting set of prediction equations are called semigeostrophic equations.

The equations from (5.34) to (5.38) form a closed set that can be used to determine the cross-frontal ageostrophic circolation in terms of wind or zonal temperature.

Suppose that the large-scale geostrophic flow acts to intensify the north-south temperature gradient through deformation, as shown in Figure 2.5.

As the temperature gradient increases, the vertical shear of the zonal wind must also increase to maintain the geostrophic balance. This requires an increase of u_g in the upper troposphere, which must be produced by the Coriolis force associated with a cross-frontal ageostrophic circulation (see equation (5.34)).

Deriving the equation (5.35) with respect to y and using the chain rule we have:

$$\frac{D}{Dt}\left(\frac{\partial b}{\partial y}\right) = Q_2 - \frac{\partial v_a}{\partial y}\frac{\partial b}{\partial y} - \frac{\partial w}{\partial y}\left(N^2 + \frac{\partial b}{\partial z}\right) \tag{5.40}$$

where

$$Q_2 = -\frac{\partial u_g}{\partial y}\frac{\partial b}{\partial x} - \frac{\partial v_g}{\partial y}\frac{\partial b}{\partial y} \tag{5.41}$$

is the y component of the Q-vector previously discussed, but expressed in the Boussinesq approximation.

Deriving the equation (5.34) with respect to z, we use the chain rule again to rearrange the terms and the thermal wind equation (5.38)to replace $\partial u_g/\partial z$ con $\partial b/\partial y$ on the right side. The result can therefore be written as:

$$\frac{D}{Dt}\left(f\frac{\partial u_g}{\partial z}\right) = Q_y - \frac{\partial v_a}{\partial z}f\left(f - \frac{\partial u_g}{\partial y}\right) + \frac{\partial w}{\partial z}\frac{\partial b}{\partial y} \tag{5.42}$$

Bibliography

[1] ARPAV (2019). Relazione evento 27/10/2018 − 01/11/2018. *(https://www.regione.veneto.it/c/document_library/get_file?uuid=094022ae-43e7-46b1-86d2-ff3ebf669b89&groupId=90748)*

[2] Betti, G. (2015). Report meteorologico 4-5 marzo 2015. *Consorzio LaMMA (http://www.lamma.rete.toscana.it/clima/report/eventi/evento_29102018.pdf)*

[3] Buzzi, A., Davolio, S., Malguzzi, P., Drofa, O., and Mastrangelo, D. (2014). Heavy rainfall episodes over Liguria of autumn 2011. *Numerical forecasting experiments. Nat. Hazards Earth Syst. Sci., 14, 1325–1340.*

[4] Buzzi, A., D'Isidoro, M., and Davolio, S. (2003). A case study of an orographic cyclone south of the Alps during the MAP SOP. *Quart. J. Roy. Meteor. Soc., 129, 1795–1818.*

[5] Buzzi, A., and Tibaldi, S. (1978). Cyclogenesis in the lee of Alps: a case study. *Quart. J. Roy. Meteor. Soc., 104, 271–287.*

[6] Campins, J., Genovés, A., Picornell, M. A., and Jansà, A. (2011). Climatology of Mediterranean cyclones using the ERA-40 dataset. *Int. J. of Climatol, 31, 1596–1614. doi:10.1002/joc.2183.*

[7] Celano, M., Costa, S., Foraci, R., e Valentini, A. (2018). Rapporto dell'evento meteorologico dal 27 al 30 ottobre 2018. *ARPAE (https://www.arpae.it/cms3/documenti/_cerca_doc/meteo/radar/rapporti/Rapporto_meteo_20181027-30.pdf)*

[8] Della Fera, S. (2019). Il ruolo di un atmospheric river nell'evento di precipitazione estrema dell'ottobre 2018 in Italia. *Tesi Università di Bologna.*

[9] Egger, J., Alpert, P., Tafferner, A., and Ziv, B. (1995). Numerical experiments on the genesis of Sharav cyclones: Idealised simulations. *Tellus, 47A, 162–174.*

[10] Fornasiero, A., and Bortolotti R., (2019). Rapporto dell'evento meteorologico dal 22 al 24 gennaio 2019. *ARPAE (https://www.arpae.it/cms3/documenti/_cerca_doc/meteo/radar/rapporti/rapporto_meteo_20190122-24.pdf)*

[11] Funk, T. (2011). A practical, basic guide to Quasi-Geostrophic theory, response to geostrophic deformation-ageostrophic motion,jet streaks. *Operations Officer National Weather Service Louisville, Kentucky.*

[12] Gil, V., Genovés, A., Picornell, M. A., and Jansà, A. (2002). Base de datos de ciclones a partir de análisis objetivos del CEPPM: Similitudes y diferencias entre el Mediterráneo occidental y oriental. *Revista de Climatología, 2, 21-28.*

[13] Holton, J. R. (2004). An introduction to dynamic Meteorology. *Fourth Edition, Volume 88 in the International Geophysics Series, Elsevier Academic Press, California.*

[14] Jansa, A., Alpert, P., Arbogast, P., Buzzi, A., Ivancan-Picek, B., Kotroni, V., Llasat, M. C., Ramis, C., Richard, E., Romero, R., and Speranza, A. (2014). MEDEX: a general overview. *Nat. Hazards Earth Syst. Sci., 14, 1965–1984. https://doi.org/10.5194/nhess-14-1965-2014.*

[15] Malguzzi, P., Grossi, G., Buzzi, A., Ranzi, R., and Buizza, R. (2006). The 1966 'century' flood in Italy: A meteorological and hydrological revisitation. *J. Geophys. Res., 111. D24106.*

[16] Martin, J. E. (2006). Mid.Latitude Atmospheric Dynamics. *A first course, John Wiley and Sons, Ltd, England, 189-204.*

[17] Miglietta, M.M., and Rotunno, R. (2019). Development Mechanisms for Mediterranean Tropical-Like Cyclones (Medicanes). *Q. J. R. Meteorol. Soc., 145, 1444-1460.*

[18] Pedemonte, L., Corazza, M., Forestieri, A., e Turato, B. (2019). Rapporto di evento meteoidrologico del 27-30/10/2018. *ARPAL (https://www.arpal.liguria.it/contenuti_statici//pubblicazioni/rapporti_eventi/2018/REM_20181027-30_rossaBCDE_vers20190107.pdf)*

[19] Picornell, M. A., Jansà, A., Genovès, A., and Campins, J. (2001). Automated database of mesocyclones from the HIRLAM(INM)-0.5 Analyses in the Western Mediterranean. *Int. J. Climatol, Vol 21, N.3, 335-354. 10.1002/joc.621*

[20] Reale, O., Atlas, R. (2001). Tropical Cyclon-Like Vortices in the Extratropics: observational Evidence and Synoptic Analysis. *Wea. Forecasting, 16, 7–34. https://doi.org/10.1175/1520-0434(2001)016<0007:TCLVIT>2.0.CO;2.*

[21] Sawyer, J. S., (1956). The vertical circulation at meteorological fronts and its relation to frontogenesis. *Proc. Roy. Soc. A, 234, 346–362.*

[22] Thorncroft, C. D., and Flocas, H. A. (1997). A case study of Saharan cyclogenesis. *Mon. Wea. Rev., 125, 1147–1165.*

[23] Trigo, I. F., Davies, T. D., and Bigg G. R. (1999). Objective Climatology of Cyclones in the Mediterranean Region. *Journal of Climate 12, 1685-1696. 10.1175/1520-0442(1999)012<1685:OCOCIT>2.0.CO;2*

[24] Trini Castelli, S., Bisignano, A., Donateo, A., et al. (2019). Evaluation of the turbulence parametrization in the MOLOCH meteorological model. *Q J R Meteorol Soc. 2020, 146, 124– 140.*

[25] Uccellini, L. W. (1990). Processes Contributing to the Rapid Development of Extratropical Cyclones. *In: Newton C.W., Holopainen E.O. (eds) Extratropical Cyclones. American Meteorological Society, Boston, MA.*

Ringraziamenti

Per realizzare il mio elaborato sono stata supportata da moltissime persone, non posso citarle tutte, ma le porto nel cuore e sono grata ad ognuno.

I miei più sentiti ringraziamenti sono rivolti alla Professoressa Di Sabatino che ha sempre supportato la mia grande passione, dandomi anche la possibilità di svolgere la tesi al di fuori dell'Università di Bologna.

In secondo luogo, ringrazio l'Ing. Francesca Giannoni e la Dott.ssa Barbara Turato che, grazie all'esperienza del tirocinio, mi hanno dato la possibilità di svolgere l'intera tesi presso l'ARPAL; Barbara mi ha sempre seguita con tanta dedizione, trasmettendomi passione e professionalità. Le attività integranti, non obbligatorie per la tesi, sono stati consigli preziosi e stimoli che mi hanno fatto crescere e appassionare ancora di più alla materia.

Ringrazio il Dott. Marcello M. Miglietta e il Dott. Silvio Davolio per la loro immensa dedizione, perché senza la loro collaborazione la tesi non sarebbe stata così ricca di argomenti.

Un caloroso ringraziamento va anche a tutte le persone conosciute presso il Centro Funzionale Meteo-Idrologico di Protezione Civile della Regione Liguria-ARPAL, grazie ai quali la tesi tocca vari campi: studio – teorico – modellistico - statistico. In particolare, il Dott. Davide Sacchetti e il Dott. Federico Cassola che mi hanno spronata e supportata nell'affrontare le criticità riscontrate.

Ed infine, ma non per importanza, la mia Famiglia che mi ha sostenuta sempre e che resta il mio porto sicuro. Saperli vicini e orgogliosi del percorso che ho scelto è stato ed è per me motivo di sprono continuo.